

THE FLORIDA STATE UNIVERSITY  
COLLEGE OF ARTS AND SCIENCES

HEAVY-QUARK ASSOCIATED PRODUCTION WITH ONE HARD PHOTON  
AT HADRON COLLIDERS

By  
HERIBERTUS BAYU HARTANTO

A Dissertation submitted to the  
Department of Physics  
in partial fulfillment of the  
requirements for the degree of  
Doctor of Philosophy

Degree Awarded:  
Summer Semester, 2013

Heribertus Bayu Hartanto defended this dissertation on June 27, 2013.

The members of the supervisory committee were:

Laura Reina  
Professor Directing Thesis

Paolo Aluffi  
University Representative

Joseph F. Owens III  
Committee Member

Andrew Askew  
Committee Member

Simon Capstick  
Committee Member

The Graduate School has verified and approved the above-named committee members, and certifies that the dissertation has been approved in accordance with the university requirements.

# TABLE OF CONTENTS

List of Tables . . . . .	v
List of Figures . . . . .	vii
Abstract . . . . .	xiv
<b>1 INTRODUCTION</b>	<b>1</b>
1.1 The Standard Model of Particle Physics . . . . .	1
1.2 Going Beyond the Leading Order Approximation . . . . .	2
1.3 $t\bar{t}\gamma$ and $b\bar{b}\gamma$ production at hadron collider: motivations . . . . .	4
1.4 Outline . . . . .	7
<b>2 Next-to-Leading Order QCD Corrections to <math>Q\bar{Q}\gamma</math> Production at Hadron Colliders</b>	<b>8</b>
2.1 Cross section in high-energy hadronic collisions . . . . .	8
2.2 $Q\bar{Q}\gamma$ production at leading order . . . . .	11
2.3 $\mathcal{O}(\alpha_s)$ virtual corrections to $pp(p\bar{p}) \rightarrow Q\bar{Q}\gamma$ production . . . . .	14
2.3.1 $\mathcal{O}(\alpha_s)$ virtual corrections to $q\bar{q} \rightarrow Q\bar{Q}\gamma$ . . . . .	18
2.3.2 $\mathcal{O}(\alpha_s)$ virtual corrections to $gg \rightarrow Q\bar{Q}\gamma$ . . . . .	24
2.4 $\mathcal{O}(\alpha_s)$ real corrections to $pp(p\bar{p}) \rightarrow Q\bar{Q}\gamma$ production . . . . .	30
2.5 Photon isolation and quark-photon final state singularities . . . . .	36
2.6 NLO cross section for $pp(p\bar{p}) \rightarrow Q\bar{Q}\gamma$ production . . . . .	39
2.7 Treatment of bottom quarks in the final state . . . . .	41
2.8 Checks on the calculation . . . . .	42
2.8.1 Direct checks on the calculation . . . . .	42
2.8.2 $pp(p\bar{p}) \rightarrow Q\bar{Q} + h/A^0$ production: indirect checks on the calculation	43
<b>3 Results for <math>t\bar{t}\gamma</math> production at Hadron Colliders</b>	<b>45</b>
3.1 The Setup . . . . .	45
3.2 Numerical Results . . . . .	46
<b>4 Results for <math>b\bar{b}\gamma</math> Production at Hadron Colliders</b>	<b>56</b>
4.1 The Setup . . . . .	56
4.2 $pp(p\bar{p}) \rightarrow b\bar{b}\gamma + X$ : at least two $b$ jets identified in the final state . . . . .	57
4.3 $pp(p\bar{p}) \rightarrow b(\bar{b})\gamma + X$ : at least one $b$ jet identified in the final state . . . . .	64
4.4 Comparison between 5FNS and 4FNS calculations . . . . .	66
4.5 Impact of NLO QCD corrections on $p\bar{p} \rightarrow b\bar{b}\gamma$ process to the $\gamma + b + X$ theoretical prediction in comparison to the Tevatron data . . . . .	70

<b>5</b>	<b>Conclusions and Outlook</b>	<b>75</b>
<b>A</b>	<b>The Standard Model</b>	<b>77</b>
<b>B</b>	<b>Leading Order Amplitudes</b>	<b>83</b>
B.1	LO amplitudes using Dirac spinor technique . . . . .	83
B.2	LO amplitudes using spinor-helicity formalism . . . . .	84
<b>C</b>	<b>Reduction of Tensor Integrals</b>	<b>88</b>
<b>D</b>	<b><math>\mathcal{O}(\alpha_s)</math> Real Corrections to <math>pp(p\bar{p}) \rightarrow Q\bar{Q}\gamma</math> process: Soft and Collinear Matrix Elements</b>	<b>93</b>
D.1	Matrix element in the soft limit . . . . .	93
D.2	Matrix element in the collinear limit . . . . .	95
	References . . . . .	98

# LIST OF TABLES

2.1	List of UV divergent diagrams in the $\mathcal{O}(\alpha_s)$ virtual corrections to the $q\bar{q} \rightarrow Q\bar{Q}\gamma$ subprocess. . . . .	22
2.2	List of IR divergent diagrams in the $\mathcal{O}(\alpha_s)$ virtual corrections to the $q\bar{q} \rightarrow Q\bar{Q}\gamma$ subprocess. . . . .	22
2.3	List of UV divergent diagrams in the $\mathcal{O}(\alpha_s)$ virtual corrections to the $gg \rightarrow Q\bar{Q}\gamma$ subprocess. . . . .	28
2.4	List of IR divergent diagrams in the $\mathcal{O}(\alpha_s)$ virtual corrections to the $gg \rightarrow Q\bar{Q}\gamma$ subprocess. . . . .	28
2.5	All possible splittings of initial partons to be included in the calculation of the collinear cross section. For the $i \rightarrow jk$ splitting process, the splitting function is given by $P_{ij}(z)$ . . . . .	34
3.1	LO and NLO QCD total cross sections for $pp(p\bar{p}) \rightarrow t\bar{t}\gamma + X$ at the LHC ( $\sqrt{s} = 8$ TeV) and the Tevatron ( $\sqrt{s} = 1.96$ TeV), together with their $K$ -factor defined as $K = \sigma_{\text{NLO}}/\sigma_{\text{LO}}$ . The uncertainties are due to renormalization/factorization scale dependence, obtained by evaluating the cross section at $\mu = m_t/2$ for the upper value and at $\mu = 2m_t$ for the lower value. The integration errors are at the % level. . . . .	46
4.1	LO and NLO QCD Total cross sections for $pp(p\bar{p}) \rightarrow b\bar{b}\gamma + X$ production with at least two $b$ jets tagged in the final state at the LHC ( $\sqrt{s} = 8$ TeV) and the Tevatron ( $\sqrt{s} = 1.96$ TeV), together with their $K$ -factor. The uncertainties are due to the dependence on the renormalization/factorization scale, obtained by evaluating the cross section at $\mu = p_T(\gamma)/4$ for the upper value and at $\mu = 4p_T(\gamma)$ for the lower value. The integration errors are well below 1% . .	57
4.2	LO and NLO QCD total cross sections for $pp(p\bar{p}) \rightarrow b(\bar{b})\gamma + X$ with at least one $b$ jet tagged in the final state at the LHC ( $\sqrt{s} = 8$ TeV) and at the Tevatron ( $\sqrt{s} = 1.96$ TeV), together with their $K$ -factor. The uncertainties are due to the dependence on the renormalization/factorization scale, obtained by evaluating the cross section at $\mu = p_T(\gamma)/4$ for the upper value and at $\mu = 4p_T(\gamma)$ for the lower value. The integration errors are well below 1% . .	64

4.3	List of subprocesses that contribute to LO and NLO 5FNS calculation of $pp(p\bar{p}) \rightarrow \gamma b + X$ process, with $i = q, \bar{q}$ and $Q = b, \bar{b}$ . . . . .	70
-----	--	----

# LIST OF FIGURES

1.1	Left: Theoretical prediction for the rapidity distributions of the dilepton final state in the $(Z, \gamma^*)$ production at the Tevatron at LO, NLO and NNLO in comparison with experimental data [3]. Right: Total cross sections for $t\bar{t}$ production at the Tevatron as a function of the top mass, including the LO, NLO, NNLO and NNLO+NNLL predictions [4]. The full NNLO corrections are included only for the $q\bar{q}$ initiated subprocess. . . . .	2
1.2	The differential cross sections for $t\bar{t}\gamma$ production as a function of $p_T(\gamma)$ at the Tevatron and the LHC. Shown are the SM predictions for $t\bar{t}\gamma$ production and its background (upper plots) and the predictions for several non-SM $tt\gamma$ couplings (lower plots) [39]. . . . .	5
1.3	The photon transverse momentum distribution measured by the D0 [55] (left) and CDF [56] (right) collaborations for $p\bar{p} \rightarrow \gamma + b + X$ process at the Tevatron in comparison with theoretical predictions. . . . .	6
2.1	Pictorial representation of a $pp(p\bar{p})$ collision in perturbative QCD. . . . .	10
2.2	Leading-order diagrams for the $q\bar{q} \rightarrow Q\bar{Q}\gamma$ subprocess. . . . .	13
2.3	Leading-order diagrams for the $gg \rightarrow Q\bar{Q}\gamma$ subprocess . . . . .	13
2.4	Schematic representation of a one-loop diagram/integral. . . . .	15
2.5	The $P_1$ virtual amplitude interfered with the LO amplitude as a function of $\phi_{t\bar{t}}$ . Numerical instabilities arise in the small $\phi_{t\bar{t}}$ region (where the GD vanishes) when the PV reduction is used (red). Implementing the reduction at the matrix element squared level (blue) and also the GD-free reduction (green) avoid the instability problem. The inset shows a blow up of the small $\phi_{t\bar{t}}$ region. . . . .	18
2.6	$\mathcal{O}(\alpha_s)$ bubble-diagram corrections to the $q\bar{q} \rightarrow Q\bar{Q}\gamma$ subprocess. The red-circled crosses correspond to all possible photon insertions. The shaded blob represents the gluonic, quark, and ghost loop corrections to the gluon propagator. . . . .	19
2.7	$\mathcal{O}(\alpha_s)$ triangle-diagram corrections to the $q\bar{q} \rightarrow Q\bar{Q}\gamma$ subprocess. The red-circled crosses correspond to all possible photon insertions while the blue blobs represent QCD correction to the quark-photon vertex . . . . .	20

2.8	Vanishing $\mathcal{O}(\alpha_s)$ triangle-diagram corrections to the $q\bar{q} \rightarrow Q\bar{Q}\gamma$ subprocess. The red-circled crosses correspond to all possible photon insertions. . . . .	20
2.9	$\mathcal{O}(\alpha_s)$ box-diagram corrections to the $q\bar{q} \rightarrow Q\bar{Q}\gamma$ subprocess. The red-circled crosses correspond to all possible photon insertions. . . . .	21
2.10	$\mathcal{O}(\alpha_s)$ pentagon-diagram corrections to the $q\bar{q} \rightarrow Q\bar{Q}\gamma$ subprocess. The red-circled crosses correspond to all possible photon insertions. . . . .	21
2.11	$\mathcal{O}(\alpha_s)$ bubble-diagram corrections to the $gg \rightarrow Q\bar{Q}\gamma$ subprocess. The red-circled crosses correspond to all possible photon insertions. The shaded blob represents the gluonic, quark, and ghost loop corrections to the gluon propagator. The $u$ -channel diagrams are obtained from the $t$ -channel diagrams by exchanging the initial state gluons. . . . .	25
2.12	Vanishing $\mathcal{O}(\alpha_s)$ triangle-diagrams in the $gg \rightarrow Q\bar{Q}\gamma$ subprocess. The red-circled crosses correspond to all possible photon insertions. . . . .	25
2.13	$\mathcal{O}(\alpha_s)$ triangle-diagram corrections to the $gg \rightarrow Q\bar{Q}\gamma$ subprocess. The red-circled crosses correspond to all possible photon insertions while the blue blobs represent QCD correction to the quark-photon vertex as shown in Fig. 2.7. The $u$ -channel diagrams are obtained from the $t$ -channel diagrams by exchanging the initial state gluons. . . . .	26
2.14	$\mathcal{O}(\alpha_s)$ box-diagram corrections to the $gg \rightarrow Q\bar{Q}\gamma$ subprocess. The red-circled crosses correspond to all possible photon insertions. The $u$ -channel diagrams are obtained from the $t$ -channel diagrams by exchanging the initial state gluons. . . . .	27
2.15	$\mathcal{O}(\alpha_s)$ pentagon-diagram corrections to the $gg \rightarrow Q\bar{Q}\gamma$ subprocess. The red-circled crosses correspond to all possible photon insertions. The $u$ -channel diagrams are obtained from the $t$ -channel diagrams by exchanging the initial state gluons. . . . .	27
2.16	Examples of $\mathcal{O}(\alpha_s)$ real-emission corrections to $Q\bar{Q}\gamma$ production in all three channels: $q\bar{q} \rightarrow Q\bar{Q}\gamma + g$ (diagrams $a, b, c$ ), $gg \rightarrow Q\bar{Q}\gamma + g$ (diagrams $d, e, f$ ), and $qg(\bar{q}g) \rightarrow Q\bar{Q}\gamma + q(\bar{q})$ (diagrams $g, h, i$ ). . . . .	31
2.17	Prompt-photon production includes (a) the direct process and (b) the fragmentation process. . . . .	37
2.18	Photon isolation in the virtual corrections (left) and the real-emission corrections (right). . . . .	37
2.19	Feynman diagrams of $gb \rightarrow b\gamma$ subprocess in the 5FNS calculation of $pp(p\bar{p}) \rightarrow b(\bar{b})\gamma + X$ process. . . . .	42
2.20	The $q\bar{q}h$ , $q\bar{q}A^0$ , $q\bar{q}\gamma$ couplings that enter in the calculation of $pp(p\bar{p}) \rightarrow Q\bar{Q} + h/A^0/\gamma$ process. . . . .	44



3.1	The upper plot shows the total cross section for $pp \rightarrow t\bar{t}\gamma + X$ at the LHC with $\sqrt{s} = 8$ TeV as a function of the (PSS2) cutoff $\delta_s$ , while keeping $\delta_c$ fixed at $2 \times 10^{-6}$ . The total cross section (black solid line) receives contribution from $2 \rightarrow 4$ and $2 \rightarrow 3$ processes as shown in the plot. The $2 \rightarrow 4$ part (red dashed line) consists of the hard/non-collinear cross section, while the $2 \rightarrow 3$ part (blue dot-dashed line) consists of the tree level, virtual, soft and hard/collinear cross sections. The lower plot shows the blow up of the total NLO cross section (black solid line) together with the corresponding integration errors. . . . .	47
3.2	NLO total cross section for $pp \rightarrow t\bar{t}\gamma + X$ at the LHC with $\sqrt{s} = 8$ TeV as a function of the (PSS2) cutoff $\delta_c$ , while keeping $\delta_s$ fixed at $10^{-4}$ . See caption of Fig. 3.1 for details. . . . .	47
3.3	NLO total cross section for $p\bar{p} \rightarrow t\bar{t}\gamma + X$ at the Tevatron with $\sqrt{s} = 1.96$ TeV as a function of the (PSS2) cutoff $\delta_s$ , while keeping $\delta_c$ fixed at $2 \times 10^{-6}$ . See caption of Fig. 3.1 for details. . . . .	48
3.4	NLO total cross section for $p\bar{p} \rightarrow t\bar{t}\gamma + X$ at the Tevatron with $\sqrt{s} = 1.96$ TeV as a function of the (PSS2) cutoff $\delta_c$ , while keeping $\delta_s$ fixed at $10^{-4}$ . See caption of Fig. 3.1 for details. . . . .	48
3.5	Dependence of the $pp \rightarrow t\bar{t}\gamma + X$ LO (red) and NLO (blue) cross section on the renormalization/factorization scale at the LHC with $\sqrt{s} = 8$ TeV and $\mu_R = \mu_F$ . The central scale is chosen to be $\mu_0 = m_t$ . . . . .	50
3.6	Dependence of the $pp \rightarrow t\bar{t}\gamma + X$ LO (red) and NLO (blue) cross section to the renormalization/factorization scale at the Tevatron with $\sqrt{s} = 1.96$ TeV and $\mu_R = \mu_F$ . The central scale is chosen to be $\mu_0 = m_t$ . . . . .	50
3.7	Scale dependence of the separate contributions to the NLO total $pp \rightarrow t\bar{t}\gamma + X$ cross section at the LHC with $\sqrt{s} = 8$ TeV. . . . .	51
3.8	Scale dependence of the separate contributions to the NLO total $pp \rightarrow t\bar{t}\gamma + X$ cross section at the Tevatron with $\sqrt{s} = 1.96$ TeV. . . . .	51
3.9	Transverse-momentum distributions of the photon (left) and top quark (right) for the $pp \rightarrow t\bar{t}\gamma + X$ process at the LHC with $\sqrt{s} = 8$ TeV. The bands correspond to the variation of the renormalization and factorization scales in the interval $m_t/2 < \mu < 2m_t$ . The lower plot shows the bin-by-bin $K$ -factor for the distribution, defined in Eq. 3.3. . . . .	52
3.10	Rapidity distributions of the photon (left) and top quark (right) for the $pp \rightarrow t\bar{t}\gamma + X$ process at the LHC with $\sqrt{s} = 8$ TeV. The bands correspond to the variation of the renormalization and factorization scales in the interval $m_t/2 < \mu < 2m_t$ . The lower plot shows the bin-by-bin $K$ -factor for the distribution, defined in Eq. 3.3. . . . .	52

3.11	Distributions of the top-quark to photon separation (left) and of the invariant mass of the $t\bar{t}\gamma$ system for the $pp \rightarrow t\bar{t}\gamma + X$ process at the LHC with $\sqrt{s} = 8$ TeV. The bands correspond to the variation of the renormalization and factorization scales in the interval $m_t/2 < \mu < 2m_t$ . The lower plot shows the bin-by-bin $K$ -factor for the distribution, defined in Eq. 3.3. . . . .	53
3.12	Transverse-momentum distributions of final state photon (left) and top quark (right) for $p\bar{p} \rightarrow t\bar{t}\gamma + X$ process at the Tevatron with $\sqrt{s} = 1.96$ TeV. The bands correspond to the variation of the renormalization and factorization scales in the interval $m_t/2 < \mu < 2m_t$ . The lower plot shows the bin-by-bin $K$ -factor for the distribution, defined in Eq. 3.3. . . . .	54
3.13	Rapidity distributions of final state photon (left) and top quark (right) for $p\bar{p} \rightarrow t\bar{t}\gamma + X$ process at the Tevatron with $\sqrt{s} = 1.96$ TeV. The bands correspond to the variation of the renormalization and factorization scales in the interval $m_t/2 < \mu < 2m_t$ . The lower plot shows the bin-by-bin $K$ -factor for the distribution, defined in Eq. 3.3. . . . .	54
3.14	The distributions of top quark-photon separation (left) and invariant mass of the $t\bar{t}\gamma$ system for $p\bar{p} \rightarrow t\bar{t}\gamma + X$ process at the Tevatron with $\sqrt{s} = 1.96$ TeV. The bands correspond to the variation of the renormalization and factorization scales in the interval $m_t/2 < \mu < 2m_t$ . The lower plot shows the bin-by-bin $K$ -factor for the distribution, defined in Eq. 3.3. . . . .	55
4.1	Dependence of the $pp \rightarrow b\bar{b}\gamma + X$ (at least two $b$ jets identified in the final state) LO (red) and NLO (blue) cross section on the renormalization/factorization scale at the LHC with $\sqrt{s} = 8$ TeV (left) and at the Tevatron with $\sqrt{s} = 1.96$ TeV (right). . . . .	59
4.2	Dependence of the $pp \rightarrow b\bar{b}\gamma + X$ (at least two $b$ jets identified in the final state) LO (red) and NLO (blue) cross section, with the $q\bar{q}$ (dashed), $gg$ (dotted) and $qg$ (dash-dotted) channels individually shown, on the renormalization/factorization scale at the LHC with $\sqrt{s} = 8$ TeV (left) and at the Tevatron with $\sqrt{s} = 1.96$ TeV (right). . . . .	59
4.3	Scale dependence of the $q\bar{q}$ - (dashed), $gg$ - (dotted), $qg$ - (dash-dotted) subprocess and the NLO total cross section (solid) for the $pp \rightarrow b\bar{b}\gamma + X$ (at least two $b$ jets identified in the final state) for four different choices of the central scale: $\mu_0 = (m_T(b)m_T(\bar{b})m_T(\gamma))^{1/3}$ (top-left), $\mu_0 = m_T(\text{leading} - b)$ (top-right), $\mu_0 = H_T/2 = \sum_{i=b,\bar{b},\gamma} E_T^i/2$ (bottom-left), $\mu_0 = p_T(\gamma)$ (bottom-right). . . . .	60
4.4	The upper plot shows the transverse-momentum distributions of the photon (left) and the leading $b$ jet (right) for $pp \rightarrow b\bar{b}\gamma + X$ (at least 2 $b$ jets identified in the final state) at the LHC with $\sqrt{s} = 8$ TeV. The bands correspond to the variation of the renormalization and factorization scales in the interval $\mu_0/4 < \mu < 4\mu_0$ . The lower plot shows the bin-by-bin $K$ -factor for the corresponding distribution. . . . .	61

4.5	The upper plot shows the pseudorapidity distribution of the photon (left) and the separation between the leading $b$ jet and the photon (right) for $pp \rightarrow b\bar{b}\gamma + X$ (at least two $b$ jets identified in the final state) at the LHC with $\sqrt{s} = 8$ TeV. The bands correspond to the variation of the renormalization and factorization scales in the interval $\mu_0/4 < \mu < 4\mu_0$ . The lower plot shows the bin-by-bin $K$ -factor for the corresponding distribution. . . . .	61
4.6	The upper plot shows the transverse-momentum distributions of the photon (left) and the leading $b$ jet (right) for $p\bar{p} \rightarrow b\bar{b}\gamma + X$ (at least two $b$ jets identified in the final state) at the Tevatron with $\sqrt{s} = 1.96$ TeV. The bands correspond to the variation of the renormalization and factorization scales in the interval $\mu_0/4 < \mu < 4\mu_0$ . The lower plot shows the bin-by-bin $K$ -factor for the corresponding distribution. . . . .	62
4.7	The upper plot shows the pseudorapidity distribution of final state photon (left) and the separation between the leading $b$ jet and the photon (right) for $p\bar{p} \rightarrow b\bar{b}\gamma + X$ (at least two $b$ jets identified in the final state) at the Tevatron with $\sqrt{s} = 1.96$ TeV. The bands correspond to the variation of the renormalization and factorization scales in the interval $\mu_0/4 < \mu < 4\mu_0$ . The lower plot shows the bin-by-bin $K$ -factor for the corresponding distribution. . . . .	62
4.8	Individual contribution of the $q\bar{q}$ (red), $gg$ (blue) and $qg$ (black) channels to the transverse-momentum distributions of the photon (left) and the leading $b$ jet (right) for $pp \rightarrow b\bar{b}\gamma + X$ (at least two $b$ jets identified in the final state) at the LHC with $\sqrt{s} = 8$ TeV, with $\mu = p_T(\gamma)$ . . . . .	63
4.9	Individual contribution of the $q\bar{q}$ (red), $gg$ (blue) and $qg$ (black) channels to the transverse momentum distributions of the photon (left) and the leading $b$ jet (right) for $p\bar{p} \rightarrow b\bar{b}\gamma + X$ (at least two $b$ jets identified in the final state) at the Tevatron with $\sqrt{s} = 1.96$ TeV, with $\mu = p_T(\gamma)$ . . . . .	63
4.10	Dependence of the $pp \rightarrow b(\bar{b})\gamma + X$ (at least one $b$ jet identified in the final state) LO (red) and NLO (blue) cross section on the renormalization/factorization scale at the LHC with $\sqrt{s} = 8$ TeV (left) and at the Tevatron with $\sqrt{s} = 1.96$ TeV (right). . . . .	65
4.11	Dependence of the $pp \rightarrow b(\bar{b})\gamma + X$ (at least one $b$ jet identified in the final state) LO (red) and NLO (blue) cross section, with the $q\bar{q}$ (dashed), $gg$ (dotted), and $qg$ (dash-dotted) channels individually shown, on the renormalization/factorization scale at the LHC with $\sqrt{s} = 8$ TeV (left) and at the Tevatron with $\sqrt{s} = 1.96$ TeV (right). . . . .	65
4.12	The upper plot shows the transverse-momentum distributions of the photon (left) and the $b$ jet (right) for $pp \rightarrow b(\bar{b})\gamma + X$ (at least one $b$ jet identified in the final state) at the LHC with $\sqrt{s} = 8$ TeV. The bands correspond to the variation of the renormalization and factorization scales in the interval $\mu_0/4 <$	

	$\mu < 4\mu_0$ . The lower plot shows the bin-by-bin $K$ -factor for the corresponding distribution. . . . .	67
4.13	The upper plot shows the pseudorapidity distribution of the photon (left) and the separation between the $b$ jet and the photon (right) for $pp \rightarrow b(\bar{b})\gamma + X$ (at least one $b$ jet identified in the final state) at the LHC with $\sqrt{s} = 8$ TeV. The bands correspond to the variation of the renormalization and factorization scales in the interval $\mu_0/4 < \mu < 4\mu_0$ . The lower plot shows the bin-by-bin $K$ -factor for the corresponding distribution. . . . .	67
4.14	The upper plot shows the transverse-momentum distributions of the photon (left) and the $b$ jet (right) for $p\bar{p} \rightarrow b(\bar{b})\gamma + X$ (at least one $b$ jet identified in the final state) at the Tevatron with $\sqrt{s} = 1.96$ TeV. The bands correspond to the variation of the renormalization and factorization scales in the interval $\mu_0/4 < \mu < 4\mu_0$ . The lower plot shows the bin-by-bin $K$ -factor for the corresponding distribution. . . . .	68
4.15	The upper plot shows the pseudorapidity distribution of the photon (left) and the separation between the $b$ jet and the photon (right) for $p\bar{p} \rightarrow b(\bar{b})\gamma + X$ (at least one $b$ jet identified in the final state) at the Tevatron with $\sqrt{s} = 1.96$ TeV. The bands correspond to the variation of the renormalization and factorization scales in the interval $\mu_0/4 < \mu < 4\mu_0$ . The lower plot shows the bin-by-bin $K$ -factor for the corresponding distribution. . . . .	68
4.16	Individual contribution of the $q\bar{q}$ (red), $gg$ (blue) and $qg$ (black) channels to the transverse-momentum distributions of the photon (left) and the $b$ jet (right) for $pp \rightarrow b(\bar{b})\gamma + X$ (at least one $b$ jet identified in the final state) at the LHC with $\sqrt{s} = 8$ TeV, with $\mu = p_T(\gamma)$ . . . . .	69
4.17	Individual contribution of the $q\bar{q}$ (red), $gg$ (blue) and $qg$ (black) channels to the transverse-momentum distributions of the photon (left) and the $b$ jet (right) for $pp \rightarrow b(\bar{b})\gamma + X$ (at least one $b$ jet identified in the final state) at the Tevatron with $\sqrt{s} = 1.96$ TeV, with $\mu = p_T(\gamma)$ . . . . .	69
4.18	Transverse-momentum distributions of the photon (left) and the $b$ jet (right) for $pp \rightarrow \gamma + b + X$ (at least one $b$ jet identified in the final state) at the LHC with $\sqrt{s} = 8$ TeV, obtained from the 4FNS (blue) and the 5FNS (red) calculations. The bands correspond to the variation of the renormalization and factorization scales in the interval $\mu_0/4 < \mu < 4\mu_0$ . . . . .	71
4.19	Transverse-momentum distributions of the photon (left) and the $b$ jet (right) for $p\bar{p} \rightarrow \gamma + b + X$ (at least one $b$ jet identified in the final state) at the Tevatron with $\sqrt{s} = 1.96$ TeV, obtained from the 4FNS (blue) and the 5FNS (red) calculations. The bands correspond to the variation of the renormalization and factorization scales in the interval $\mu_0/4 < \mu < 4\mu_0$ . . . . .	71

4.20	Different subprocesses that contribute to the NLO photon transverse-momentum distribution for $p\bar{p} \rightarrow \gamma + b + X$ process, calculated using 5FNS approach, at the Tevatron [57] . . . . .	72
4.21	The photon- $p_T$ distribution for $\gamma + b + X$ at the Tevatron with $\sqrt{s} = 1.96$ TeV. The numbers for the CDF data and the NLO 5FNS calculation (red) [57] are taken from [56]. The bands correspond to the variation of the renormalization and factorization scales in the interval $\mu_0/2 < \mu < 2\mu_0$ . The left plot shows the CDF data and the prediction from NLO 5FNS calculation compared with improved NLO 5FNS prediction (blue) that includes the NLO QCD corrections only to the $q\bar{q} \rightarrow b(\bar{b})\gamma$ subprocess. The right plot shows the CDF data and the prediction from NLO 5FNS calculation compared with the prediction from the pure 4FNS calculation (blue). . . . .	72
A.1	SM Feynman rules for interaction vertices that are used in the calculation of $Q\bar{Q}\gamma$ production. . . . .	82
A.2	SM Feynman rules for the propagators that are used in the calculation of $Q\bar{Q}\gamma$ production. . . . .	82
D.1	Divergent Feynman diagrams in the soft limit, for the $q\bar{q} \rightarrow Q\bar{Q}\gamma$ subprocess. The green-circled crosses correspond to all possible external gluon leg insertions.	94
D.2	Schematic diagram involving a final state gluon radiated from initial quark line in the $q\bar{q} \rightarrow Q\bar{Q}\gamma + g$ subprocess. . . . .	95

# ABSTRACT

We present the calculation of heavy-quark associated production with a hard photon at hadron colliders, namely  $pp(p\bar{p}) \rightarrow Q\bar{Q}\gamma + X$  (for  $Q = t, b$ ), at Next-to-Leading Order (NLO) in Quantum Chromodynamics (QCD). We study the impact of NLO QCD corrections on the total cross section and several differential distributions at both the Tevatron and the Large Hadron Collider (LHC). For  $t\bar{t}\gamma$  production we observe a sizeable reduction of the renormalization and factorization scale dependence when the NLO QCD corrections are included, while for  $b\bar{b}\gamma$  production a considerable scale dependence still persists at NLO in QCD. This is consistent with what emerges in similar processes involving  $b$  quarks and vector bosons and we explain its origin in detail. For  $b\bar{b}\gamma$  production we study both the case in which at least one  $b$  jet and the case in which at least two  $b$  jets are observed. We perform the  $b\bar{b}\gamma$  calculation using the Four Flavor Number Scheme (4FNS) and compare the case where at least one  $b$  jet is observed with the corresponding results from the Five Flavor Number Scheme (5FNS) calculation. Finally we compare our results for  $p\bar{p} \rightarrow \gamma + b + X$  with the Tevatron data.

# CHAPTER 1

## INTRODUCTION

### 1.1 The Standard Model of Particle Physics

The Standard Model (SM) of particle physics is nowadays the best framework to understand the dynamics of all elementary particles that have been observed in high energy collisions. It is a quantum field theory (QFT) based on the gauge symmetry group  $SU(3)$  for color,  $SU(2)$  for weak isospin, and  $U(1)$  for hypercharge. The color quantum number is associated to the dynamics of strong interactions, which by itself is the subject of Quantum Chromodynamics (QCD), while the weak isospin and hypercharge quantum numbers are fundamental to the dynamics of electroweak (EW) interactions.

In the SM, the fundamental constituents of matter are fermions that interact via their coupling to the gauge vector bosons of the gauge symmetry group(s), namely the *gluons* for the strong interaction, the  $W^\pm$  and  $Z$  bosons for the weak interaction, and the photon for the electromagnetic interaction. Fermions come in three generations or families and they are labeled as *leptons* if they only interact electromagnetically and weakly, or as *quarks* if they also interact strongly. Mass terms for gauge bosons and fermions are not allowed by gauge invariance. The simplest way to remedy this problem and to explain the large masses of  $W^\pm$  and  $Z$  bosons (80.4 and 91.18 GeV respectively) is by coupling the gauge sector to some scalar degrees of freedom (commonly referred to as the Higgs field) whose potential undergoes spontaneous symmetry breaking. The same scalar degrees of freedom can then be independently coupled to fermions and give origin to fermion mass terms in the lagrangian. A more detailed description of the SM will be given in Appendix A. The most important highlight of Large Hadron Collider (LHC) physics has been indeed the discovery in July 2012 of the scalar boson that is believed to be the SM Higgs boson [1, 2]. More precise measurements of its couplings will determine possible deviations from the SM pattern and shed some light on the kind of new physics that can embed the SM dynamics in a more fundamental framework and resolve some of the least satisfactory and more arbitrary aspects of this theory.

Indeed, all models of new physics that complement and complete the SM at energies beyond the electroweak scale owe their origin to the attempt of explaining the breaking of the EW symmetry (i.e. the origin of the weak gauge boson masses) and the hierarchy of

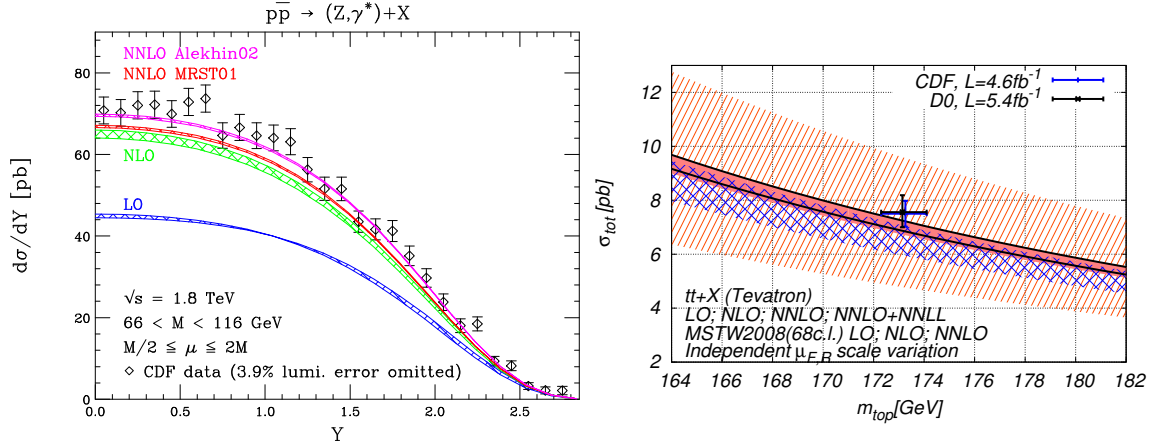


Figure 1.1: Left: Theoretical prediction for the rapidity distributions of the dilepton final state in the  $(Z, \gamma^*)$  production at the Tevatron at LO, NLO and NNLO in comparison with experimental data [3]. Right: Total cross sections for  $t\bar{t}$  production at the Tevatron as a function of the top mass, including the LO, NLO, NNLO and NNLO+NNLL predictions [4]. The full NNLO corrections are included only for the  $q\bar{q}$  initiated subprocess.

fermion masses. Evidence of new physics beyond the SM will finally shed some light on the explanation of several other experimental facts, coming from non-accelerator experiments, that demand physics beyond the SM. We remind, among others, the evidence of neutrino masses through flavor oscillations of neutrinos, the large baryon asymmetry present in the universe, and the presence of dark matter and dark energy in the universe for which the SM has no candidates.

## 1.2 Going Beyond the Leading Order Approximation

Many beyond the Standard Model (BSM) scenarios have been proposed to provide solutions to the still open problems of the SM. With the data collected at the Tevatron, and the turning on of the LHC in 2010, we now have the unique opportunity to obtain even more stringent test of the SM and to confirm or exclude several BSM scenarios. In order to accurately discriminate signals from background, it is very important to have very precise theoretical predictions to be compared with experiments. In the framework of perturbative QFT, more accurate theoretical predictions can be obtained by properly taking into account both QCD and EW higher-order corrections, as well as resumming well-defined sets of (large) corrections at all orders, or by interfacing fixed-order calculations with parton-shower Monte Carlo programs.



The theoretical predictions obtained using the Leading Order (LO) approximation in perturbative QFT are usually good only for roughly estimating the rate of a process, due to the large theoretical uncertainties that accompany the LO predictions. This theoretical uncertainties are originated from the truncation of the perturbative series at a certain (fixed) order. The left-hand side of Fig. 1.1 shows the rapidity distributions of the dilepton final state in Drell-Yan production at the Tevatron ( $p\bar{p} \rightarrow (Z, \gamma^*) + X$ ) [3]. It is clear that both the normalization and shape of the distributions from experimental data are best described by the inclusion of higher order corrections, in this case the Next-to-Next-to-Leading Order (NNLO) QCD corrections. The Next-to-Leading Order (NLO) QCD corrections improve the agreement with the data but are still not sufficient for this particular process. The right-hand side of Fig. 1.1 shows the total cross section for top-quark pair production at the Tevatron as a function of the mass of the top quark,  $m_t$  [4]. The uncertainties of the theoretical predictions are dramatically reduced when higher-order corrections are included. Theoretical predictions with smaller uncertainty are obtained, in this case, by including the NNLO QCD corrections as well as by resumming classes of logarithmic corrections at all order, up to Next-to-Next-to-Leading Logarithms (NNLL).

Over the last few decades the structure of higher-order QCD/EW perturbative calculations has been thoroughly studied and many tools have been developed to obtain theoretical predictions for processes at hadron colliders. LO tools are largely automated nowadays and inclusion of new BSM models in these packages is also straightforward. **MadGraph/MadEvent** [5], and **CompHEP/CalcHEP** [6, 7] are among the LO tools that are publicly available. NLO programs that contain hardcoded NLO calculations of a number of processes have been around for many years. Examples of programs that can be used for several processes and are publicly available are **MCFM** [8], **VBFNLO** [9], and the **PHOX** family [10], while many more individual/non-public codes exist. On the other hand, due to the complexity of higher order calculations, the progress in the automatization of NLO calculations has been slower and has received a substantial boost only recently, due to the development of new techniques for loop calculations and to the availability of more powerful computational facilities. As will be discussed in Chapter 2, NLO calculations consist of virtual and real corrections. The virtual corrections can be computed using either traditional Feynman-diagram or unitarity-based techniques (see [11] for a comprehensive review on both techniques), while for the real corrections, the phase-space-slicing and subtraction techniques are widely used. **BlackHat** [12], **FormCalc** [13], **GoSam** [14], **MadLoop** [15], **NLOX** [16], and **OpenLoops** [17] are examples of automated packages to calculate the virtual corrections. On the other hand, for the real corrections, examples of automated packages based on subtraction techniques are **MadDipole** [18] and **Sherpa** [19, 20], that implement the Catani-Seymour dipole subtraction formalism [21, 22], as well as **MadFKS** [15], that implements the Frixione-Kunszt-Signer (FKS) subtraction [23]. Monte Carlo event-generator programs, such as **Pythia** [24, 25], **Herwig** [26, 27], and **Sherpa**, are utilized to get the full description of hadronic collisions (i.e. including hadronization effects). In order to include hadronization effects, the partons that are present in the fixed-order calculation have to be showered first. Two different methods are available to systematically interface NLO fixed-order calculations with parton showers, namely the **MC@NLO** [28] and the **POWHEG** [29, 30] methods. At the NNLO level new methods and ideas have been pioneered on  $2 \rightarrow 1$  and  $2 \rightarrow 2$  hadronic processes of

particular relevance, notably the Drell-Yan process[3],  $t\bar{t}$  production [4, 31], and inclusive Higgs+jet production [32] (see Fig. 1.1). Beyond NNLO, the resummation of sets of large kinematic logarithmic corrections has been addressed and often shown to play a crucial role in a process by process basis.

In this context, the calculation of processes like the one presented in this thesis (photon + heavy-quark pair at NLO) is of technical value because it allows to test NLO automated packages when they can be used for processes involving several massive fermions, and provide an analytical and usually computationally more efficient alternative. Moreover, it allows the study of QCD effects for hard-photon production with  $b$  jets ( $Q = b$ ), with potential implications for processes that play a crucial role in Higgs-boson and new physics searches (e.g.  $W/Z + b$ ,  $H/A^0 + b$ ) as well as in the determination of the bottom-quark parton distribution function.

### 1.3 $t\bar{t}\gamma$ and $b\bar{b}\gamma$ production at hadron collider: motivations

The discovery of the top quark in 1995 by the CDF and D0 experiments at the Fermilab Tevatron collider established the validity of the SM with three generations of quarks [33, 34]. In the following years, the two Tevatron experiments measured the cross section for  $t\bar{t}$  production with precision comparable to the most accurate theoretical predictions [35], while the two LHC experiments, ATLAS and CMS, have measured the  $t\bar{t}$  production at both 7 and 8 TeV center-of-mass energies [36]. The measurement of the top-quark mass has also been established at the few percent level by the Tevatron ( $m_{top} = 173.2 \pm 0.6 \pm 0.8$  GeV, March 2013 combination) [37] and the LHC ( $m_{top} = 173.3 \pm 0.5 \pm 1.3$  GeV, June 2012 combination) [38]. It is an important task to measure the top-quark properties precisely due to the fact that the top quark is the most massive particle in the SM and has the largest coupling to the Higgs boson,  $y_t \sim 1$ . For example, deviations of the SM top-quark couplings to EW gauge bosons may provide hints of new physics responsible for EW symmetry breaking.

Important properties of the top quark, such as the  $t\bar{t}Z$  and  $t\bar{t}\gamma$  couplings, have not been measured yet and the only indirect constraint on the  $t\bar{t}Z$  coupling came from LEP data. Existing studies [39, 40, 41] have shown that one of the main limitations will then be the theoretical systematic error. We note incidentally that a high-energy measurement of  $e^+e^- \rightarrow \gamma^*/Z^* \rightarrow t\bar{t}$  (if and when available) would not necessarily provide a better access to the  $t\bar{t}\gamma$  and  $t\bar{t}Z$  couplings because it would measure a superposition of both  $t\bar{t}\gamma$  and  $t\bar{t}Z$  couplings. A direct measurement will provide a crucial handle in determining the *standard* and *non-standard* components of the top-quark electroweak couplings. The total cross section for  $t\bar{t}Z$  and  $t\bar{t}\gamma$  productions at the LHC have been measured recently [42, 43, 44].

The most general Lorentz-invariant  $t\bar{t}\gamma$  coupling or vertex function is expressed in terms of four independent form factors (for on-shell top quark, anti-top quark, and photon), which

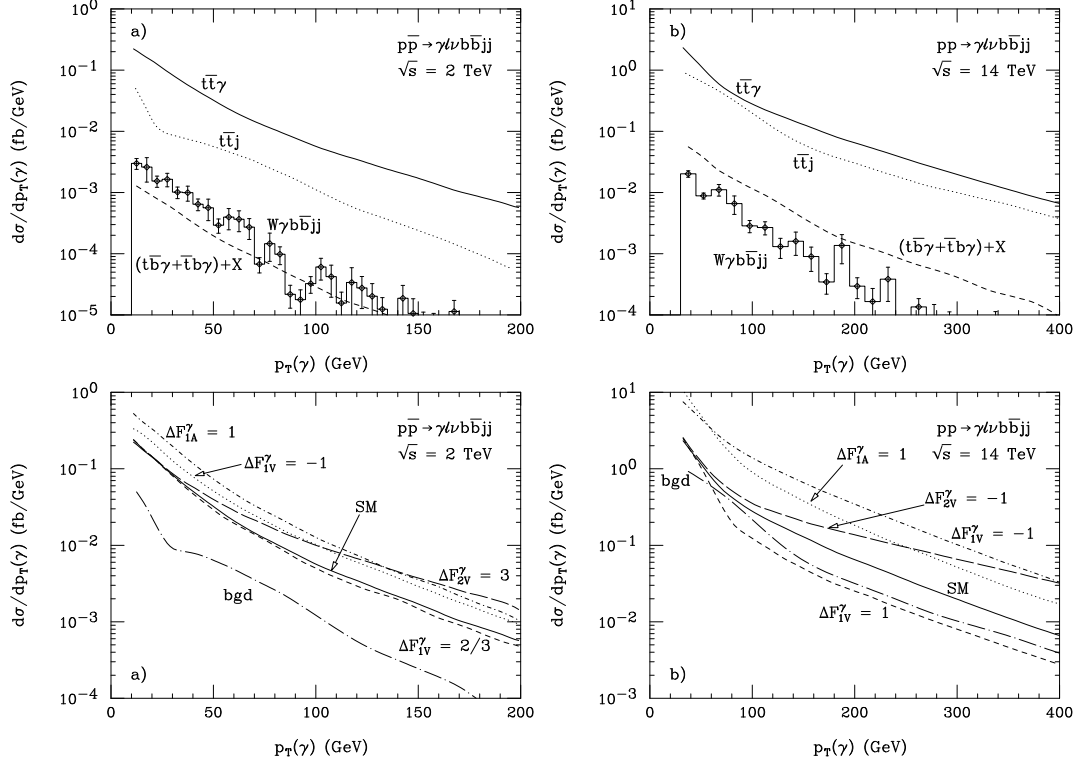


Figure 1.2: The differential cross sections for  $t\bar{t}\gamma$  production as a function of  $p_T(\gamma)$  at the Tevatron and the LHC. Shown are the SM predictions for  $t\bar{t}\gamma$  production and its background (upper plots) and the predictions for several non-SM  $tt\gamma$  couplings (lower plots) [39].

are functions of kinematics invariants, as follows,

$$\Gamma_{\mu}^{t\bar{t}\gamma}(k^2, p, \bar{p}) = -ie \left[ \gamma_{\mu} (F_{1V}^{\gamma}(k^2) + \gamma_5 F_{1A}^{\gamma}(k^2)) + \frac{\sigma_{\mu\nu}}{2m_t} (p + \bar{p})^{\nu} (iF_{2V}^{\gamma}(k^2) + \gamma_5 F_{2A}^{\gamma}(k^2)) \right], \quad (1.1)$$

where  $p$  and  $\bar{p}$  are the outgoing momenta of the top and anti-top quark, and  $k = p + \bar{p}$  is the momentum of the photon. The form factors  $F_{1V}^{\gamma, SM}$ ,  $F_{2V}^{\gamma, SM}$ , and  $F_{2A}^{\gamma, SM}$  correspond, in the low energy limit ( $k^2 \rightarrow 0$ ) to the charge (modulus a minus sign, depending on the convention that is used for the Feynman rules), anomalous magnetic moment, and electric dipole moment of the top quark respectively. At tree level, the form factors  $F_{iV,A}^{\gamma, SM}$  give us the Feynman rules for the interaction vertices. For example, at tree level in the SM,  $F_{1V}^{\gamma, SM} = -2/3$  and  $F_{2V}^{\gamma, SM} = F_{1A}^{\gamma, SM} = F_{2A}^{\gamma, SM} = 0$ .

The most promising channel to study the  $t\bar{t}\gamma$  coupling at hadron colliders has been shown to be the  $\gamma\ell\nu_{\ell}b\bar{b}jj$  channel (where  $\ell = e, \mu$  and  $\nu_{\ell} = \nu_e, \nu_{\mu}$ ) which receives contributions from QCD  $t\bar{t}\gamma$  production as well as  $t\bar{t}$  production with radiative top-quark decay [39].

Predictions for the photon transverse momentum ( $p_T(\gamma)$ ) distribution in  $t\bar{t}\gamma$  production, for SM and non-SM  $t\bar{t}\gamma$  couplings, as well as for the most important backgrounds are shown in Fig. 1.2, at both the Tevatron and the LHC. The top panels of Fig. 1.2 show the background composition for  $t\bar{t}\gamma$  production.  $t\bar{t}j$  production, where a jet is misidentified as a photon, is the dominant background, followed by single-top production ( $t\bar{b}\gamma + \bar{t}b\gamma$ ), and  $W\gamma b\bar{b}jj$ . The lower panels of Fig. 1.2 show the  $p_T(\gamma)$  distribution when various non-standard form factors in the  $t\bar{t}\gamma$  coupling defined in Eq. 1.1 are included and only one form factor at a time is allowed to deviate from its SM value. The non-SM  $t\bar{t}\gamma$  couplings that are investigated in Fig. 1.2 are defined by

$$\Delta F_{iV,A}^\gamma(k^2) = F_{iV,A}^\gamma(k^2) - F_{iV,A}^{\gamma,SM}. \quad (1.2)$$

Deviations from the SM pattern can be isolated and identified in this relatively clean channel if we can provide accurate theoretical predictions. We note that the calculation of  $t\bar{t}\gamma$  production at NLO QCD accuracy has been reported by Duan et al. [45] and Melnikov et al. [46], while for the  $t\bar{t}Z$  production, the NLO prediction is calculated by Lazopoulos et al. [47, 48], Kardos et al. [49] and Garzelli et al. [50]. The NLO calculation for  $t\bar{t}j$  production, which is the main background for the  $t\bar{t}\gamma$  production, has been reported by Dittmaier et al. [51, 52] and Melnikov et al. [53, 54]. In this thesis we reproduce the results of [45, 46] with full agreement and work toward the implementation of our calculation into a full-fledged NLO parton-shower Monte Carlo.

On the other hand, the associated production of a photon with a  $b\bar{b}$  pair is a crucial component of the theoretical prediction for direct photon production with  $b$  quarks (when either one  $b$  or both  $b$ -initiated jets are tagged). The direct photon production in association with  $b$  quarks, in particular with one  $b$  quark, can be used to directly constrain the  $b$ -quark PDF, which so far has only been derived from the gluon parton distribution function (PDF). This much awaited measurement will play a very important role in improving the accuracy with which other crucial processes like  $W/Z + b$  and  $H/A^0 + b$  can be predicted. The NLO prediction for direct photon production in association with one  $b$  jet has been calculated by Stavreva and Owens [57] in the so-called "variable flavor scheme" or 5FNS (see Chapter 2 and 4 for details). On the experimental side, the measurement of the  $\gamma + b + X$  process at the Tevatron has been performed by the D0 collaboration with 1 fb<sup>-1</sup> [58] and 8.7 fb<sup>-1</sup> data sets [55] as well as by the CDF collaboration with 86 pb<sup>-1</sup> [59] and more recently 9.1 fb<sup>-1</sup> data sets [56]. The  $p_T(\gamma)$  distributions for the  $p\bar{p} \rightarrow \gamma + b + X$  process at the Tevatron from the most recent D0 [55] and CDF [56] results are shown in Fig. 1.3. The experimental data are compared with the predictions from the NLO calculation in [57], as well as other predictions from **Pythia**, **Sherpa** and a calculation which uses the  $k_T$ -factorization approach [60] that contains only partial NLO corrections but selected higher order effects. In the intermediate to high photon transverse momentum region, one notices some discrepancies between the data and the NLO calculation. In this thesis we present the NLO QCD results for direct photon production with either one or two  $b$  jets, using a fixed flavor scheme or 4FNS (see Chapter 2 and 4 for details), and discuss our results in the context of existing theoretical [57] and experimental [55, 56] results.

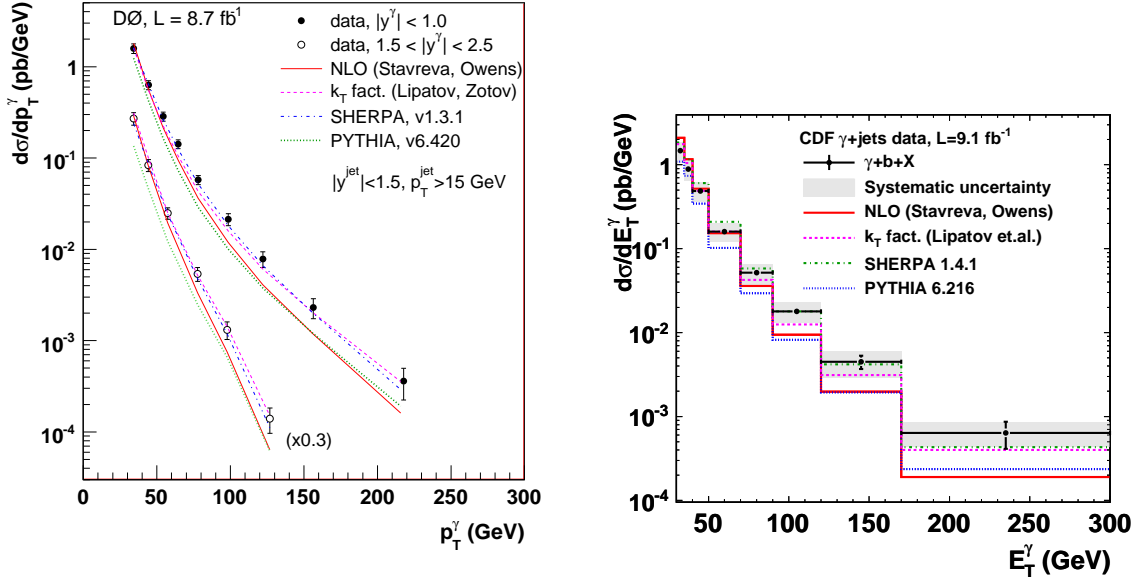


Figure 1.3: The photon transverse momentum distribution measured by the DØ [55] (left) and CDF [56] (right) collaborations for  $p\bar{p} \rightarrow \gamma + b + X$  process at the Tevatron in comparison with theoretical predictions.

## 1.4 Outline

In this thesis we will calculate the NLO QCD corrections to heavy-quark associated production with one hard photon at hadron colliders ( $pp(p\bar{p}) \rightarrow Q\bar{Q}\gamma$ , with  $Q = t, b$ ). We use a Feynman-diagram approach to calculate the virtual corrections, and a phase-space-slicing method with two cutoffs to compute the real corrections. The hard-photon requirement in the calculation is realized by imposing a cut on the photon transverse momentum,  $p_T(\gamma)$ . The thesis is organized as follows. In Chapter 2 we discuss in detail the NLO calculation of  $Q\bar{Q}\gamma$  production. The treatment of final state photon and bottom quarks are also reviewed. In Chapter 3 and Chapter 4 we present numerical results, including the LO and NLO total cross sections as well as some interesting differential distributions, for  $t\bar{t}\gamma$  and  $b\bar{b}\gamma$  production at the Tevatron and the LHC, respectively. For  $b\bar{b}\gamma$  production, we consider both the case in which at least one  $b$  jet is identified (1***b***-tag) and the case in which at least two  $b$  jets are identified (2***b***-tag) in the final state. In particular we discuss how the NLO QCD corrections presented in this thesis make the theoretical predictions for  $\gamma + b + X$  (1***b***-tag) more consistent with the Tevatron data [55, 56]. In Chapter 5, we conclude with a summary and some outlook for possible refinements of the calculation presented in this thesis. All the results presented in this thesis will appear in [61].

# CHAPTER 2

## NEXT-TO-LEADING ORDER QCD CORRECTIONS TO $Q\bar{Q}\gamma$ PRODUCTION AT HADRON COLLIDERS

In this Chapter we present in detail the NLO QCD calculation of  $Q\bar{Q}\gamma$  production at hadron colliders where  $Q = t, b$  is a heavy quark. This Chapter is organized as follows. The theoretical framework in calculating the total or differential cross sections in high-energy hadronic collisions is discussed in Sec. 2.1. The description of the calculation for the tree level cross section as well as for the  $\mathcal{O}(\alpha_s)$  virtual and real corrections are presented in Secs. 2.2, 2.3, 2.4 respectively. The presence of a real photon in the final state requires an isolation procedure in order to significantly reduce the background. The photon-isolation prescription as well as the treatment of singularities induced by the radiation of a final state photon from massless quark are discussed in Sec. 2.5. Once all the ingredients of the NLO calculation are introduced, the formulae to calculate the NLO cross section are presented in Sec. 2.6. The theoretical and experimental issues due to the presence of bottom quarks in the final state are illustrated in Sec. 2.7. Finally, in Sec. 2.8 we review some checks that we have performed on our calculation. All Feynman diagrams in this thesis are drawn using the `Jaxodraw` package [62], while all plots are produced using the `GNUplot` software. Further software packages that have been used or developed as part of this project will be mentioned later in this Chapter.

### 2.1 Cross section in high-energy hadronic collisions

The effects of strong interactions in high energy processes can be described systematically within the framework of perturbative QCD, due to the property of asymptotic freedom, where the running coupling constant of strong interactions becomes small at high energies. This has two important consequences. First of all, it allows us to calculate total and differential hadronic cross sections (like those for  $pp$  or  $p\bar{p}$  collisions) in terms of the corresponding cross sections for the constituents quarks and gluons, here denoted by  $d\hat{\sigma}$ . According to a *factorization* principle (pictorially illustrated in Fig. 2.1), we can indeed

write the differential cross section as [63]

$$d\sigma(pp(p\bar{p}) \rightarrow \mathbf{X}) = \sum_{ij} \int dx_1 dx_2 f_i^p(x_1, \mu_F) f_j^{p/\bar{p}}(x_2, \mu_F) d\hat{\sigma}(ij \rightarrow \mathbf{X}; x_1, x_2, \mu_F, \mu_R), \quad (2.1)$$

where  $\mathbf{X}$  is a generic partonic final state,  $i$  and  $j$  are initial-state quarks and gluons (collectively named *partons*), while  $f_i^{p/\bar{p}}$  are the so-called Parton Distribution Functions (PDFs), to be interpreted as the probability of finding a parton  $i$  in a proton (antiproton) with a fraction  $x_i$  of the parent hadron momentum. Furthermore, the smallness of the strong coupling ( $\alpha_s$ ) gives us the possibility of providing the theoretical prediction for  $\hat{\sigma}$  by perturbatively calculating its series expansion in  $\alpha_s$ ,

$$d\hat{\sigma}(ij \rightarrow \mathbf{X}; x_1, x_2, \mu_F, \mu_R) = \alpha_s^k(\mu_R) \sum_{m=0}^{\infty} \alpha_s^m(\mu_R) d\hat{\sigma}_{ij}^{(m)}(x_1, x_2, \mu_F, \mu_R), \quad (2.2)$$

where  $k$  is the order of the corresponding tree-level process in powers of  $\alpha_s$ . The first term in the perturbative expansion of the partonic cross section in  $\alpha_s$  ( $m = 0$ ), is traditionally dubbed as leading order (LO) or Born process. The next order ( $m = 1, 2, \dots$ ) are dubbed as (Next-to-) <sup>$m$</sup> Leading Order (N <sup>$m$</sup> LO) corrections.  $\mu_R$  and  $\mu_F$  in Eqs. 2.1 and 2.2 are the *renormalization* and *factorization* scales respectively. The factorization scale can be thought of as the scale that separates the long- and short-distance physics, where a perturbative calculation of QCD effects is appropriate. The renormalization scale is an unphysical scale introduced in the regularization procedure of the partonic cross section that suffers from ultraviolet singularities. The cross section, of course, should not depend on these two unphysical scales, i.e.

$$\mu_i \frac{d\sigma(\mu_i)}{d\mu_i} = 0, \quad (2.3)$$

but any truncation of the expansion in Eq. 2.2 will result in a residual scale dependence of the cross section, induced by terms of higher order with respect to the truncation. Therefore, higher perturbative orders capture more and more of the complex dynamics of strong interactions and therefore allow for a more careful modelling of real high-energy hadronic collisions.

The PDFs, which describe the long distance nature of the strong interactions, are non-perturbative quantities and have to be determined from experimental data. However, due to the smallness of the strong coupling, their dependence on the factorization scale, i.e. their rescaling with  $\mu_F$ , can be calculated using the DGLAP (Dokshitzer-Gribov-Lipatov-Altarelli-Parisi) [64, 65, 66] equations,

$$\frac{\partial f_i(x, \mu_F^2)}{\partial \ln \mu_F^2} = \frac{\alpha_s}{2\pi} \sum_j \int_x^1 \frac{dz}{z} P_{ij}(z, \alpha_s) f_j\left(\frac{x}{z}, \mu_F^2\right), \quad (2.4)$$

where  $P_{ij}$  are the unregulated Altarelli-Parisi splitting functions given in Eqs. D.21 - D.24. Several groups nowadays provide independent sets of PDF based on fitting both high-energy



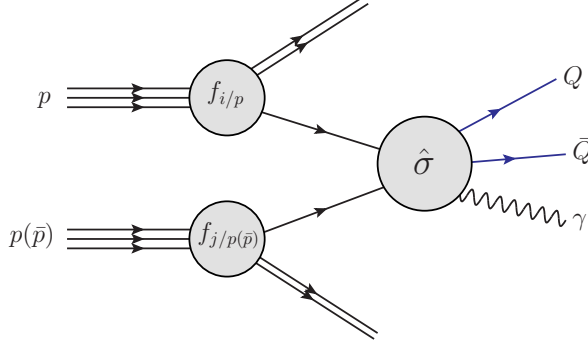


Figure 2.1: Pictorial representation of a  $pp(p\bar{p})$  collision in perturbative QCD.

and low-energy data, e.g. ABM [67], CTEQ [68], HERAPDF [69], MSTW [70], NNPDF [71], etc. The LHAPDF package [72] provides a collection of all major PDF sets with a Fortran/C++ interface.

At Next-to-Leading Order (NLO), the partonic cross section is given by,

$$d\hat{\sigma}_{ij}^{\text{NLO}} = d\hat{\sigma}_{ij}^{\text{LO}} + \frac{\alpha_s}{4\pi} \delta d\hat{\sigma}_{ij}^{\text{NLO}}, \quad (2.5)$$

where, in the notation of Eq. 2.2,  $d\hat{\sigma}_{ij}^{\text{LO}} = \alpha_s^k d\hat{\sigma}_{ij}^{(0)}$  and  $\delta d\hat{\sigma}_{ij}^{\text{NLO}} = 4\pi\alpha_s^k d\hat{\sigma}_{ij}^{(1)}$ . The NLO corrections are made of one-loop virtual corrections ( $d\hat{\sigma}_{ij}^{\text{virt}}$ ) and one-parton real-emission corrections ( $d\hat{\sigma}_{ij}^{\text{real}}$ ), i.e.

$$\delta d\hat{\sigma}_{ij}^{\text{NLO}} = d\hat{\sigma}_{ij}^{\text{virt}} + d\hat{\sigma}_{ij}^{\text{real}}. \quad (2.6)$$

The calculation of the LO, virtual, and real emission partonic cross sections for  $Q\bar{Q}\gamma$  hadroproduction will be discussed in Secs. 2.2, 2.3 and 2.4, respectively. Based on the evolution equation of the strong coupling,

$$\mu_R^2 \frac{d\alpha_s(\mu_R)}{d\mu_R^2} = -b_0\alpha_s^2 + \dots, \quad (2.7)$$

where  $b_0$  is,

$$b_0 = \frac{1}{4\pi} \left( \frac{11}{3}N - \frac{2}{3}n_{\text{lf}} \right), \quad (2.8)$$

where  $N = 3$  is the number of colors, and  $n_{\text{lf}}$  is the number of light-quark flavors, and on the DGLAP evolution equations for the PDFs in Eq. 2.4, the explicit scale dependence of



the NLO partonic cross section is given by

$$\begin{aligned}
d\hat{\sigma}_{ij}^{\text{NLO}}(x_1, x_2, \mu_R, \mu_F) &= \alpha_s^k(\mu_R) d\hat{\sigma}_{ij}^{(0)}(x_1, x_2) + \alpha_s^{k+1}(\mu_R) d\hat{\sigma}_{ij}^{(1)}(x_1, x_2, \mu_R, \mu_F) \\
&= \alpha_s^k(\mu_R) d\hat{\sigma}_{ij}^{(0)}(x_1, x_2) + \alpha_s^{k+1}(\mu_R) d\hat{\sigma}_{ij}'^{(1)}(x_1, x_2) \\
&+ \frac{\alpha_s^{k+1}(\mu_R)}{4\pi} \left\{ 8\pi b_0 \ln\left(\frac{\mu_R^2}{\hat{s}}\right) d\hat{\sigma}_{ij}^{(0)}(x_1, x_2) \right. \\
&\quad \left. - 2\ln\left(\frac{\mu_F^2}{\hat{s}}\right) \sum_n \left[ \int_\rho^1 dz_1 P_{in} d\hat{\sigma}_{nj}^{(0)}(x_1 z_1, x_2) \right. \right. \\
&\quad \left. \left. + \int_\rho^1 dz_2 P_{nj} d\hat{\sigma}_{in}^{(0)}(x_1, x_2 z_2) \right] \right\}. \quad (2.9)
\end{aligned}$$

In Eq. 2.9,  $d\hat{\sigma}_{ij}^{(0,1)}$  are defined in Eq. 2.2 and we have rewritten  $d\hat{\sigma}_{ij}^{(1)}$  as

$$d\hat{\sigma}_{ij}^{(1)} = d\hat{\sigma}_{ij}'^{(1)} + \text{terms containing } \ln\left(\frac{\mu_{R,F}}{\hat{s}}\right),$$

where  $d\hat{\sigma}_{ij}'^{(1)}$  is the piece of NLO correction that neither depends on  $\mu_R$  nor  $\mu_F$ .  $\hat{s}$  is the partonic center-of-mass energy squared, and  $\rho = \hat{s}_{\min}/\hat{s}$ . It is sensible to choose the value of  $\mu_R$  and  $\mu_F$  of the order of the hard scattering scale of the process in order to avoid large logarithms to appear in the perturbation series. However, for the process with multiple scales, the presence of such large logarithms are unavoidable. It is a common practice also to assume that  $\mu_R = \mu_F = \mu$  and study the systematic uncertainty on a given theoretical prediction by varying  $\mu$  in a predefined range about a chosen central value.

## 2.2 $Q\bar{Q}\gamma$ production at leading order

At lowest order in perturbation theory (LO), the  $pp(p\bar{p}) \rightarrow Q\bar{Q}\gamma$  process consists of two partonic subprocesses,

$$q(i_1, p_1) + \bar{q}(i_2, p_2) \rightarrow Q(i_3, p_3) + \bar{Q}(i_4, p_4) + \gamma(p_5), \quad (2.10)$$

and

$$g(a_1, p_1) + g(a_2, p_2) \rightarrow Q(i_3, p_3) + \bar{Q}(i_4, p_4) + \gamma(p_5), \quad (2.11)$$

where  $p_i$  denote the momenta of external particles, the  $i$ 's and  $a$ 's are color indices for quarks and gluons respectively. The above momentum and color index assignments will be used for both LO and NLO virtual amplitudes calculation. The Feynman diagrams for the  $q\bar{q}$  and  $gg$  subprocesses at leading order are shown in Figs. 2.2 and 2.3. The LO amplitudes in the  $q\bar{q}$  subprocess have only one common color factor,

$$\mathcal{M}_0^{q\bar{q}} = t_{i_2 i_1}^a t_{i_3 i_4}^a \mathcal{A}_0^{q\bar{q}}, \quad (2.12)$$

where

$$\mathcal{A}_0^{q\bar{q}} = \sum_{k=1}^4 \mathcal{A}_k^{q\bar{q}}, \quad (2.13)$$

and the individual  $\mathcal{A}_k^{q\bar{q}}$  amplitudes correspond to the Feynman diagrams shown in Fig. 2.2. The LO amplitudes in the  $gg$  subprocess can be decomposed into an 'abelian' ( $ab$ ) and a 'non-abelian' ( $nab$ ) piece,

$$\mathcal{M}_0^{gg} = [t^{a_1}, t^{a_2}]_{i_3 i_4} \mathcal{A}_0^{nab} + \{t^{a_1}, t^{a_2}\}_{i_3 i_4} \mathcal{A}_0^{ab}, \quad (2.14)$$

where

$$\begin{aligned} \mathcal{A}_0^{nab} &= \mathcal{A}_{0,s} + \frac{1}{2}(\mathcal{A}_{0,t} - \mathcal{A}_{0,u}), \\ \mathcal{A}_0^{ab} &= \frac{1}{2}(\mathcal{A}_{0,t} + \mathcal{A}_{0,u}). \end{aligned} \quad (2.15)$$

$\mathcal{A}_{0,s}$ ,  $\mathcal{A}_{0,t}$  and  $\mathcal{A}_{0,u}$  are the amplitudes for the  $s$ ,  $t$  and  $u$  channel processes respectively, and can be written as

$$\begin{aligned} \mathcal{A}_{0,s} &= \mathcal{A}_1^{gg} + \mathcal{A}_2^{gg}, \\ \mathcal{A}_{0,t} &= \mathcal{A}_3^{gg} + \mathcal{A}_4^{gg} + \mathcal{A}_5^{gg}, \\ \mathcal{A}_{0,u} &= \mathcal{A}_6^{gg} + \mathcal{A}_7^{gg} + \mathcal{A}_8^{gg}. \end{aligned} \quad (2.16)$$

The Feynman diagrams corresponding to each  $\mathcal{A}_k^{gg}$  are shown in Fig. 2.3. The amplitudes squared, averaged over initial spins and colors, are then given by

$$\overline{\sum} |\mathcal{M}_0^{q\bar{q}}|^2 = \frac{1}{4} \frac{1}{9} \frac{N^2 - 1}{4} \sum |\mathcal{A}_0^{q\bar{q}}|^2, \quad (2.17)$$

$$\overline{\sum} |\mathcal{M}_0^{gg}|^2 = \frac{1}{4} \frac{1}{64} \left\{ \frac{N(N^2 - 1)}{2} \sum |\mathcal{A}_0^{nab}|^2 - \frac{N^2 - 1}{N} \sum |\mathcal{A}_0^{ab}|^2 \right\}. \quad (2.18)$$

In squaring the amplitude, we use the following polarization vector sums, for photon and gluons respectively:

$$\sum_{\lambda} \varepsilon_{\mu}(p_5, \lambda) \varepsilon_{\nu}^*(p_5, \lambda) = -g_{\mu\nu}, \quad (2.19)$$

$$\sum_{\lambda} \varepsilon_{\mu}(p_i, \lambda) \varepsilon_{\nu}^*(p_i, \lambda) = -g_{\mu\nu} + \frac{p_{1\mu} p_{2\nu} + p_{2\mu} p_{1\nu}}{p_1 \cdot p_2}, \quad \text{for } i = 1, 2. \quad (2.20)$$

The LO partonic total/differential cross section is obtained by integrating the averaged matrix element squared  $\overline{\sum} |\mathcal{M}_0|^2$  over the final-state  $Q\bar{Q}\gamma$  three-body phase space

$$d\hat{\sigma}_{ij}^{\text{LO}} = dPS(Q\bar{Q}\gamma) \overline{\sum} |\mathcal{M}_0^{ij}|^2, \quad (2.21)$$

where  $ij = q\bar{q}, gg$ . The total cross section is obtained by integrating over all kinematic variables of the  $Q\bar{Q}\gamma$  phase-space measure, that is denoted by  $dPS(Q\bar{Q}\gamma)$ , while for the differential cross section, the corresponding kinematic variable(s) is (are) not integrated and the distribution of events over the corresponding range(s) is obtained.

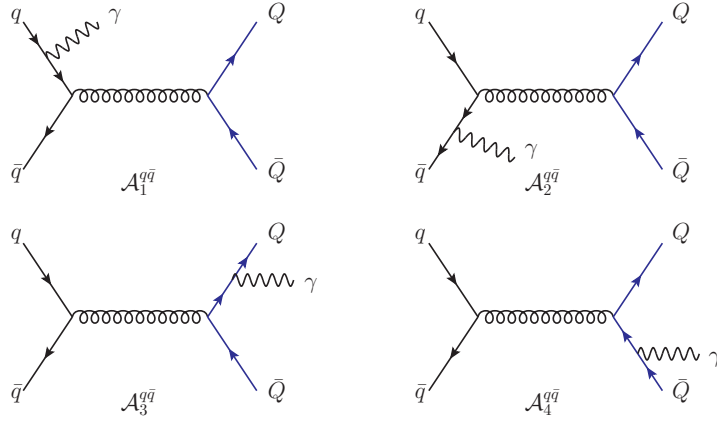


Figure 2.2: Leading-order diagrams for the  $q\bar{q} \rightarrow Q\bar{Q}\gamma$  subprocess.

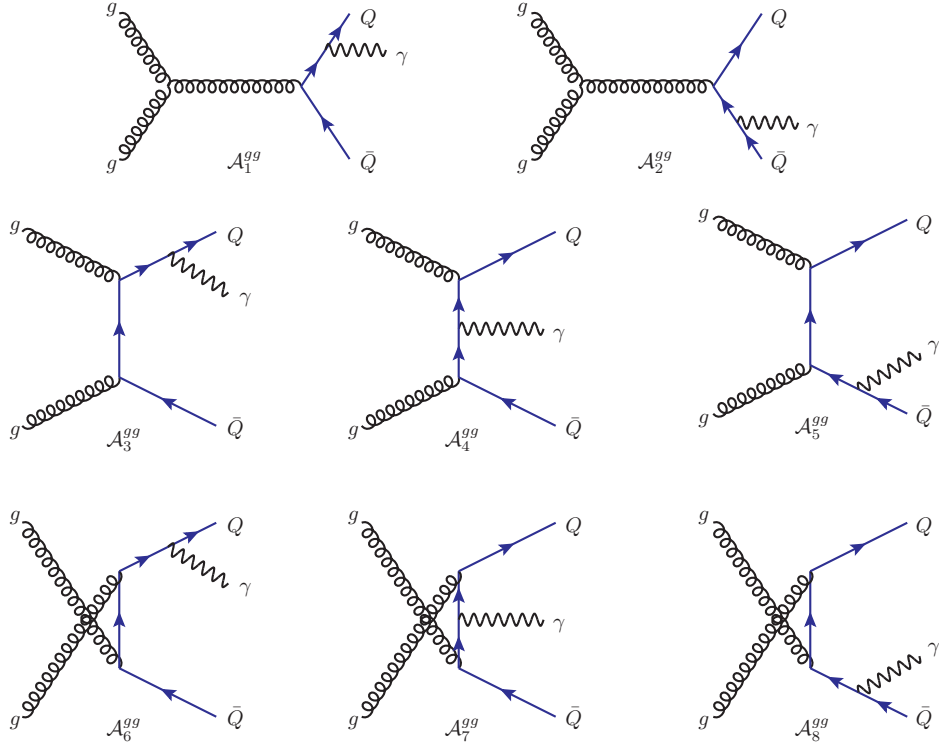


Figure 2.3: Leading-order diagrams for the  $gg \rightarrow Q\bar{Q}\gamma$  subprocess

### 2.3 $\mathcal{O}(\alpha_s)$ virtual corrections to $pp(p\bar{p}) \rightarrow Q\bar{Q}\gamma$ production

The  $\mathcal{O}(\alpha_s)$  virtual corrections to the  $q\bar{q}$  and  $gg$  subprocesses consist of one-loop corrections to the tree level diagrams illustrated in Figs. 2.2 and 2.3. The partonic cross section for the virtual corrections is obtained by integrating the virtual amplitudes of the two subprocesses interfered with the corresponding LO amplitudes over the  $Q\bar{Q}\gamma$  three-body phase space, namely,

$$d\hat{\sigma}_{ij}^{\text{virt}} = dPS(Q\bar{Q}\gamma) 2\mathcal{Re} \overline{\sum} (\mathcal{M}_0^{ij})^* \mathcal{M}_{\text{virt}}^{ij} . \quad (2.22)$$

The virtual amplitudes,  $\mathcal{M}_{\text{virt}}^{ij}$ , are expressed as linear combinations of Dirac structures multiplied by one-loop integrals. One-loop integrals originate from one-loop diagrams, the topology of which is schematically shown in Fig. 2.4. They can be either scalar or tensor integrals of the form

$$I_N^{0,\mu_1\cdots\mu_P}(p_1, \dots, p_{N-1}; m_0, m_1, \dots, m_{N-1}) = \frac{16\pi^2}{i} \mu^{4-d} \int \frac{d^d k}{(2\pi)^d} \frac{1, k^{\mu_1} \cdots k^{\mu_P}}{D_0 D_1 \cdots D_{N-1}} , \quad (2.23)$$

where  $k$  is the loop momentum,  $N$  is the number of denominators, and  $P$  is the number of loop-momentum factors in the numerator. The denominator of a one-loop integral is factorized into the product of propagator-like terms  $D_i$  of the form

$$D_i = (k + q_i)^2 - m_i^2, \quad (2.24)$$

where  $q_i = p_1 + \dots + p_i$  is the propagator momentum ( $q_0 = 0$ ),  $m_0, \dots, m_{N-1}$  are the corresponding internal masses, and  $p_1, \dots, p_N$  are the momenta of the external legs attached to the loop. Traditionally, one-loop integrals, up to  $N = 5$ , are labelled as follows,

$$\begin{aligned} I_1(m_0) &= A(m_0), \\ I_2(p_1; m_0, m_1) &= B(p_1; m_0, m_1), \\ I_3(p_1, p_2; m_0, m_1, m_2) &= C(p_1, p_2; m_0, m_1, m_2), \\ I_4(p_1, p_2, p_3; m_0, m_1, m_2, m_3) &= D(p_1, p_2, p_3; m_0, m_1, m_2, m_3), \\ I_5(p_1, p_2, p_3, p_4; m_0, m_1, m_2, m_3, m_4) &= E(p_1, p_2, p_3, p_4; m_0, m_1, m_2, m_3, m_4), \end{aligned} \quad (2.25)$$

with none or more tensor indices attached to them.

One-loop integrals suffer from ultraviolet (UV) and infrared (IR) divergences. To regulate those divergences, we use dimensional regularization with  $d = 4 - 2\epsilon$ , for both UV and IR divergences. UV divergences, arising from self-energy and vertex diagrams, are cancelled by introducing counterterms for the external fields, the strong coupling, and the heavy-quark mass. The QED coupling (or electric charge) is not renormalized at the first order in  $\alpha_s$ . IR divergences arising in vertex, box, and pentagon diagrams are cancelled by analogous IR divergences in the real-emission part of the NLO cross section. The cancellation of IR singularities for inclusive observables is guaranteed by the Kinoshita-Lee-Nauenberg (KLN) theorem [73, 74].  $\mu$  is the renormalization scale introduced in Sec. 2.1 and a factor of  $\mu^{4-d}$  is included in the definition of the integrals to keep the strong coupling adimensional. A detailed discussion of the UV and IR divergences of the  $(q\bar{q}, gg) \rightarrow Q\bar{Q}\gamma$  virtual amplitudes

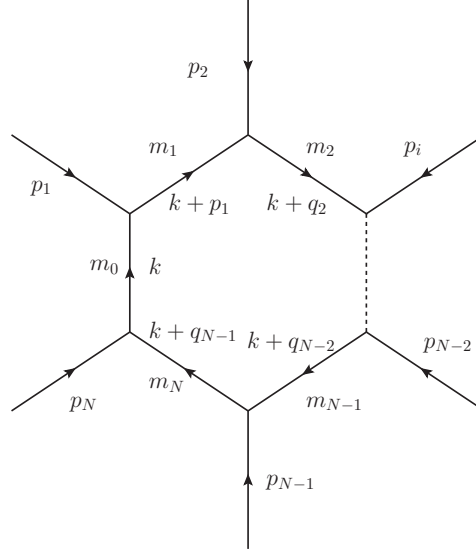


Figure 2.4: Schematic representation of a one-loop diagram/integral.

will be presented in Secs. 2.3.1 and 2.3.2.

The tensor integrals that appear in the virtual amplitudes are first Lorentz decomposed into a linear combination of tensor-integral coefficients multiplied by suitable tensor structures made of external momenta and the metric tensor. For example, the Lorentz decomposition of a rank-2 3-point tensor integral can be written as

$$\begin{aligned}
C^{\mu\nu}(p_1, p_2; m_0, m_1, m_2) &= I_3^{\mu\nu}(p_1, p_2; m_0, m_1, m_2) \\
&= \frac{16\pi^2}{i} \mu^{4-d} \int \frac{d^d k}{(2\pi)^d} \frac{k^\mu k^\nu}{[k^2 - m_0^2][(k + q_1)^2 - m_1^2][(k + q_2)^2 - m_2^2]} \\
&= g^{\mu\nu} C_{00}(p_1, p_2, m_0, m_1, m_2) \\
&\quad + p_1^\mu p_1^\nu C_{11}(p_1, p_2, m_0, m_1, m_2) + p_2^\mu p_2^\nu C_{22}(p_1, p_2, m_0, m_1, m_2) \\
&\quad + (p_1^\mu p_2^\nu + p_2^\mu p_1^\nu) C_{12}(p_1, p_2, m_0, m_1, m_2), \tag{2.26}
\end{aligned}$$

where the  $C_{ij}$ 's are the tensor-integral coefficients for the rank-2 3-point tensor integral. The tensor integral coefficients are then reduced to a linear combination of scalar integrals using various techniques such as Passarino-Veltman (PV) [75], Denner-Dittmaier [76], and Diakonidis et al. [77] methods. More details and an example of tensor-integral reduction using PV method will be presented in Appendix C. This leaves the one-loop scalar integrals as the fundamental building blocks of a one-loop calculation. They have all been evaluated in the literature, and are nowadays collected into libraries. We use the QCDLoop package [78] for this purpose.

Once the one-loop tensor integrals have been reduced, the numerator of a one-loop diagram consists of Dirac structures containing  $\gamma$  matrices and/or slashed external momenta,

$\not{p}_i$ , sandwiched between Dirac spinors, and multiplied by the polarization vectors of the external photon and gluons (in the  $gg$ -initiated subprocess). It is convenient to reduce to the smallest set of Dirac structures, the so called Standard Matrix Elements (SMEs). In obtaining the virtual-correction contributions to the NLO matrix element squared in Eq. 2.22, each SME is interfered with the LO amplitude, and once we substitute the external-polarization vector sums in Eqs. 2.19 and 2.20 and evaluate the traces, the result is expressed in terms of scalar products of external momenta. We use the **FORM** symbolic manipulation program [79] to decompose tensor integrals in terms of tensor-integral coefficients, to handle the simplification of Dirac structures to SMEs, and to interfere the SMEs with the LO amplitude. The bookkeeping of all UV and IR divergencies is performed analytically by exporting the **FORM** output to **Maple**, which we use for simplification and further manipulation of the pole parts only. This allows us to check analytically the cancellation of the UV poles by properly defined counterterms and the cancellation of the IR poles against the corresponding terms in the  $\mathcal{O}(\alpha_s)$  real correction to the cross section (see Sec. 2.4). On the other hand, both the pole and finite parts of the virtual corrections are exported to a **FORTTRAN** code for numerical evaluation. To compute the total cross section and differential distributions we perform the phase space integration numerically by using **VEGAS**, an adaptive multidimensional Monte Carlo integration algorithm [80].

We have also used the spinor-helicity formalism, as a cross check, in calculating the LO and virtual amplitudes, as will be discussed in Appendix B.2. In this case, we project out the spin states of external particles at the amplitude level and express the results in terms of the spinor products,  $\langle ij \rangle$  or  $[ij]$ , instead of the vector products  $p_i \cdot p_j$  (see Appendix B.2 for notation). The amplitudes can be evaluated directly, by evaluating the spinor products numerically. The value of the matrix elements squared are obtained by multiplying two complex numbers. The usage of spinor-helicity formalism also generalize the definition of the SMEs. Now, for each SME, we obtain a set of spin/polarization dependent SMEs, e.g.

$$\text{SME}(i) \rightarrow \text{SME}(i; s_1, s_2, s_3, s_4, s_5),$$

where the  $s_i$ 's are the spin/helicity/polarization assignments of the external particles. The SMEs can now be directly evaluated without interfering with the LO amplitude first. Using the spinor-helicity formalism to handle the Dirac structures in the virtual amplitude is not only useful as a cross check, but is also important to keep the information on the polarization of the final-state particles.

Finally, the evaluation of the cross section is prone to numerical instabilities which arise in the reduction of tensor integrals using standard technique, such as the PV reduction (as illustrated in in Appendix C). This is due to inverse powers of the Gram determinant (GD) introduced at every stage of the reduction, where the GD for an  $N$ -point one-loop integral is defined by

$$\Delta_N = \begin{vmatrix} p_1 \cdot p_1 & p_1 \cdot p_2 & \cdots & p_1 \cdot p_{N-1} \\ p_2 \cdot p_1 & p_2 \cdot p_2 & \cdots & p_2 \cdot p_{N-1} \\ \vdots & \vdots & \ddots & \vdots \\ p_{N-1} \cdot p_1 & p_{N-1} \cdot p_2 & \cdots & p_{N-1} \cdot p_{N-1} \end{vmatrix}. \quad (2.27)$$

Numerical instabilities arise when the GD becomes very small, due to degenerate kinematic configurations. The worst case of these instabilities in our calculation occurs in pentagon diagrams because the integral depends directly on the momenta of external particles (not combinations of them as one finds in box, vertex, and bubble diagrams), which makes easier to find mutual collinear configurations. Moreover, the pentagon diagrams in  $Q\bar{Q}\gamma$  production may contain up to rank-3 5-point tensor integrals in the  $q\bar{q} \rightarrow Q\bar{Q}\gamma$  subprocess and up to rank-4 5-point tensor integrals in the  $gg \rightarrow Q\bar{Q}\gamma$  subprocess which introduce three or four powers of the inverse GD, respectively.

In order to avoid the numerical instabilities arising in the pentagon integrals, we implemented the following two approaches:

- We reduced the 5-point tensor integrals at the amplitude-squared level. In this case, before defining the one-loop integrals, we interfere the amplitudes of the pentagon diagrams with the LO amplitude, such that

$$2\mathcal{R}e \sum \mathcal{A}_0^* \cdot \mathcal{A}_P \propto \int \frac{d^d k}{(2\pi)^d} \frac{\{k^2, k \cdot p_i, p_i \cdot p_j\}}{D_0 D_1 D_2 D_3 D_4}. \quad (2.28)$$

Expressing the  $k^2$  and  $k \cdot p_i$  in terms of  $D_i$  according to Eq. 2.24, and simplifying as many  $D_i$ 's in the denominator as possible, the tensor 5-point functions are expressed as a linear combination of scalar 5-point functions and tensor 4-point functions, which are numerically stable.

- We implemented the GD-free reduction technique by Diakonidis et al. [77], that is based on recursion relations between Feynman integrals in different dimensions [81, 82, 83]. This GD-free reduction is more complicated than the PV reduction and less time efficient. In the numerical calculation, we switch from the PV reduction to this GD-free reduction only when the GD becomes small. We detect the instability by comparing the numerical value of the pole parts of the renormalized virtual amplitude to the value obtained from the corresponding analytic expressions that are obtained from both the virtual amplitude calculation as well as the real correction.

To illustrate the numerical instability problem, consider one of the pentagon diagrams in the  $q\bar{q} \rightarrow t\bar{t}\gamma$  subprocess,  $P_1$ , shown in Fig. 2.10. Parameterizing the phase space point for the  $q\bar{q} \rightarrow t\bar{t}\gamma$  subprocess in terms of the partonic center-of-mass energy and angle of the incoming partons in the partonic center-of-mass frame ( $\hat{s}$ ,  $\theta$ ), the invariant mass and momentum of  $t\bar{t}$  pair ( $\hat{s}_{t\bar{t}}$ ,  $p_{t\bar{t}}$ ), and the polar and azimuthal angles in the  $t\bar{t}$  center-of-mass frame ( $\theta_{t\bar{t}}$ ,  $\phi_{t\bar{t}}$ ), the 5-point GD can be written as,

$$\Delta_5 = \frac{1}{16} |p_{t\bar{t}}|^2 \hat{s}^2 (4m_t^2 - \hat{s}_{t\bar{t}}) \sin^2 \theta \sin^2 \theta_{t\bar{t}} \sin^2 \phi_{t\bar{t}}. \quad (2.29)$$

Fig. 2.5 shows how numerical instabilities arise in  $2\mathcal{R}e \sum \mathcal{A}_0^* \cdot \mathcal{A}_{P_1}$  for small  $\phi_{t\bar{t}}$  when the PV reduction is used while they are not present when the GD-free reduction and the reduction at the amplitude-squared level are used.

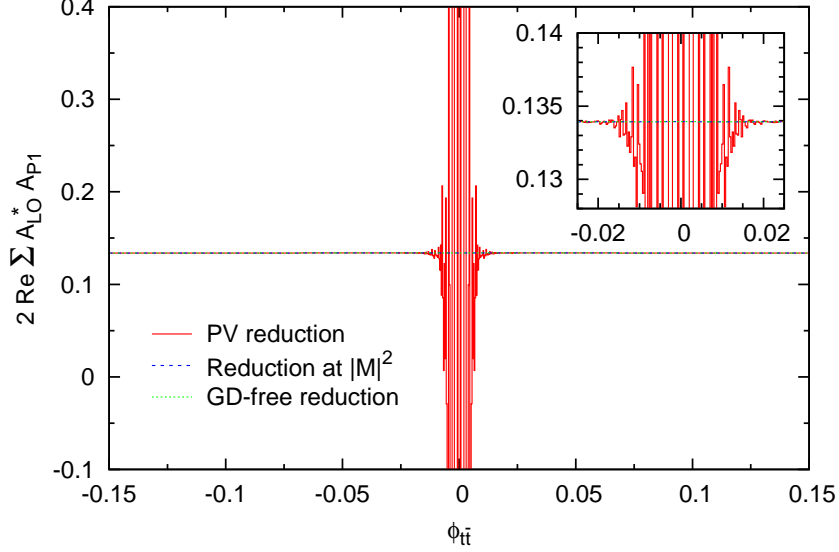


Figure 2.5: The  $P_1$  virtual amplitude interfered with the LO amplitude as a function of  $\phi_{t\bar{t}}$ . Numerical instabilities arise in the small  $\phi_{t\bar{t}}$  region (where the GD vanishes) when the PV reduction is used (red). Implementing the reduction at the matrix element squared level (blue) and also the GD-free reduction (green) avoid the instability problem. The inset shows a blow up of the small  $\phi_{t\bar{t}}$  region.

### 2.3.1 $\mathcal{O}(\alpha_s)$ virtual corrections to $q\bar{q} \rightarrow Q\bar{Q}\gamma$

The  $\mathcal{O}(\alpha_s)$  virtual corrections to  $q\bar{q} \rightarrow Q\bar{Q}\gamma$  consist of bubble, triangle, box, and pentagon diagrams that are shown in Figs. 2.6 - 2.10. We notice that the triangle diagrams shown in Fig. 2.8 vanish due to Furry's theorem [84]. As previously discussed, the virtual corrections suffer from UV and IR singularities. The diagrams that contribute to the UV singularities in this channel are listed in Table 2.1. The UV-divergent contributions have been extracted analytically, and they are given by

$$2\text{Re} \overline{\sum} (\mathcal{M}_0^{q\bar{q}})^* \mathcal{M}_{\text{virt}}^{q\bar{q}} \Big|_{UV} = \overline{\sum} |\mathcal{M}_0^{q\bar{q}}|^2 \left\{ \sum_{i,j} \Delta_{UV}^{q\bar{q}}(S_i^{(j)} + V_i^{(j)}) + 2 \left[ \left( \delta Z_2^{(Q)} \right)_{UV} + \left( \delta Z_2^{(q)} \right)_{UV} + \delta Z_{\alpha_s} \right] \right\}, \quad (2.30)$$

where

$$\begin{aligned} \sum_{i,j} \Delta_{UV}^{q\bar{q}}(S_i^{(j)} + V_i^{(j)}) &= \frac{\alpha_s}{2\pi} \left( \frac{3N}{2} - \frac{1}{2N} \right) \left[ \frac{\mathcal{N}_s}{\epsilon_{UV}} + \frac{\mathcal{N}_Q}{\epsilon_{UV}} \right] \\ &+ \frac{\alpha_s}{2\pi} \left[ \mathcal{N}_s \left( \frac{5N}{3} - \frac{2n_{\text{lf}}}{3} \right) - \delta_{b,Q} \mathcal{N}_Q \frac{2}{3} - \mathcal{N}_t \frac{2}{3} \right] \left( \frac{1}{\epsilon_{UV}} \right), \end{aligned} \quad (2.31)$$

$\delta Z_2^{(q)}$ ,  $\delta Z_2^{(Q)}$ , and  $\delta Z_{\alpha_s}$  are the  $\mathcal{O}(\alpha_s)$  terms of the massless-quark wavefunction, heavy-quark wavefunction, and strong coupling renormalization constants respectively (with  $Z_i =$



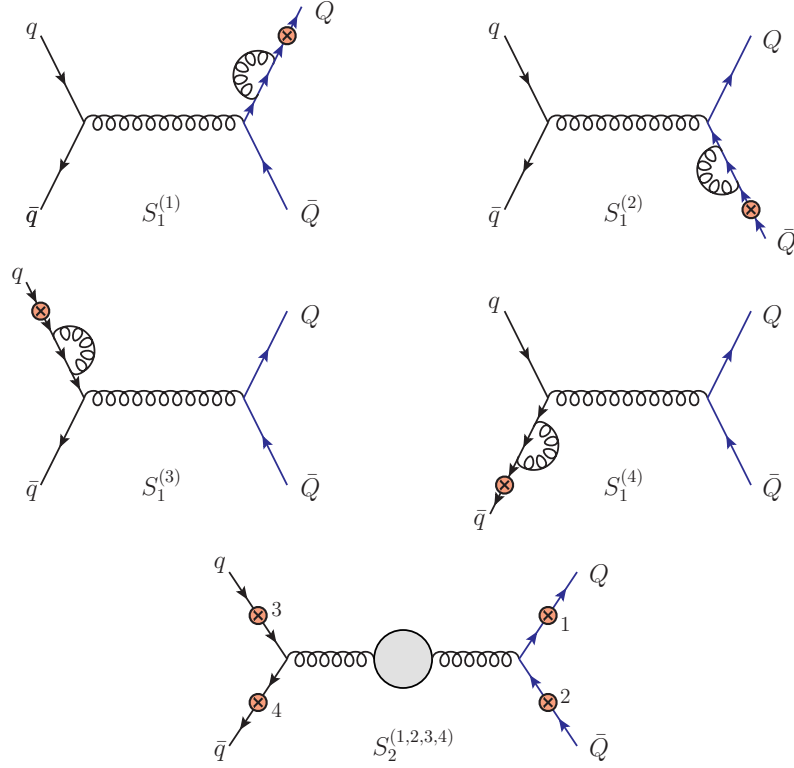


Figure 2.6:  $\mathcal{O}(\alpha_s)$  bubble-diagram corrections to the  $q\bar{q} \rightarrow Q\bar{Q}\gamma$  subprocess. The red-circled crosses correspond to all possible photon insertions. The shaded blob represents the gluonic, quark, and ghost loop corrections to the gluon propagator.

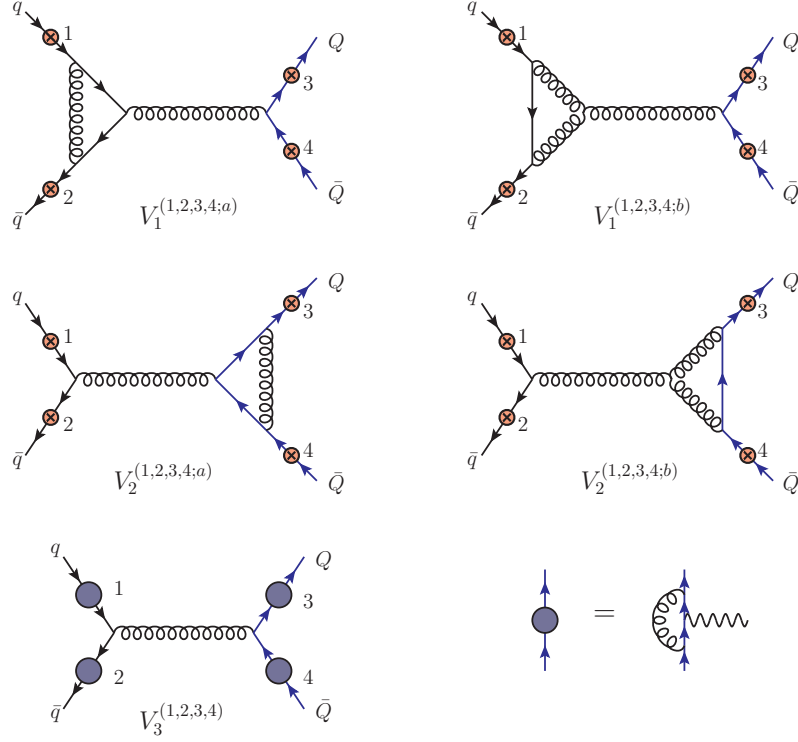


Figure 2.7:  $\mathcal{O}(\alpha_s)$  triangle-diagram corrections to the  $q\bar{q} \rightarrow Q\bar{Q}\gamma$  subprocess. The red-circled crosses correspond to all possible photon insertions while the blue blobs represent QCD correction to the quark-photon vertex

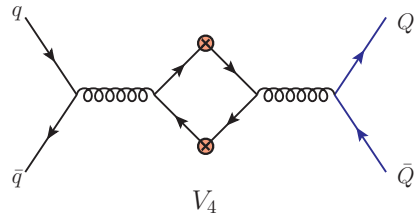


Figure 2.8: Vanishing  $\mathcal{O}(\alpha_s)$  triangle-diagram corrections to the  $q\bar{q} \rightarrow Q\bar{Q}\gamma$  subprocess. The red-circled crosses correspond to all possible photon insertions.

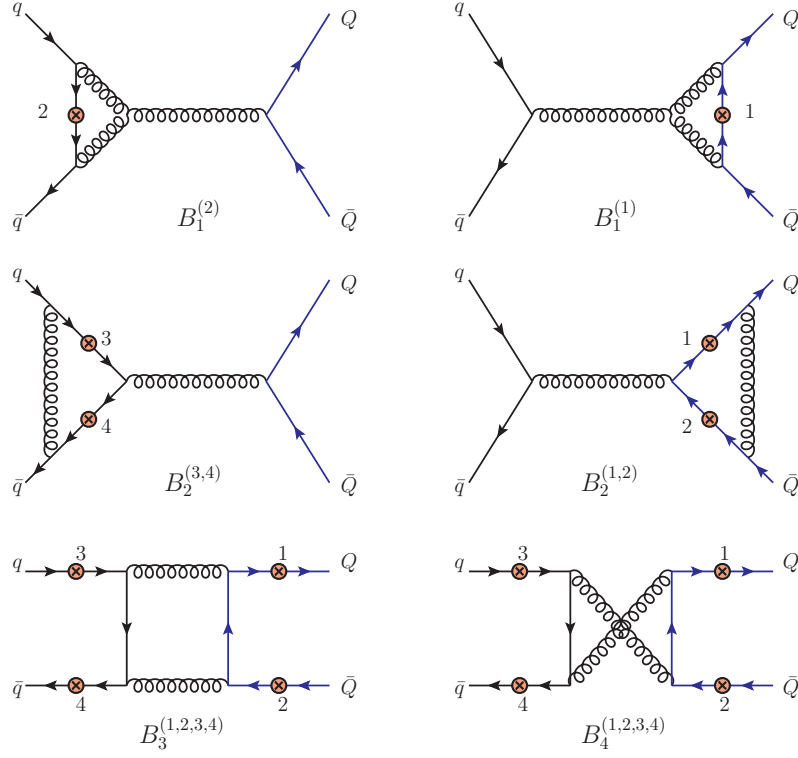


Figure 2.9:  $\mathcal{O}(\alpha_s)$  box-diagram corrections to the  $q\bar{q} \rightarrow Q\bar{Q}\gamma$  subprocess. The red-circled crosses correspond to all possible photon insertions.

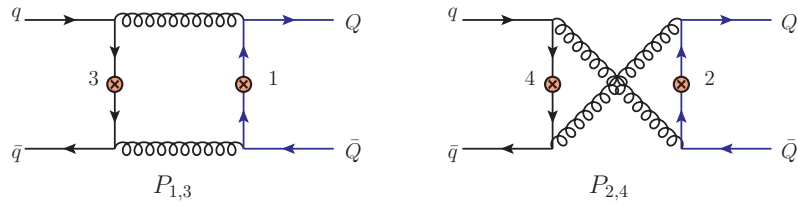


Figure 2.10:  $\mathcal{O}(\alpha_s)$  pentagon-diagram corrections to the  $q\bar{q} \rightarrow Q\bar{Q}\gamma$  subprocess. The red-circled crosses correspond to all possible photon insertions.

Table 2.1: List of UV divergent diagrams in the  $\mathcal{O}(\alpha_s)$  virtual corrections to the  $q\bar{q} \rightarrow Q\bar{Q}\gamma$  subprocess.

Classes	Diagrams
Bubbles	$S_1^{(1,2,3,4)}, S_2^{(1,2,3,4)}$
Triangles	$V_1^{(1,2,3,4;a,b)}, V_2^{(1,2,3,4;a,b)}, V_3^{(1,2,3,4)}$
Boxes	-
Pentagons	-
CTs	$\delta Z_{\alpha_s}, \delta Z_2^{(Q)}, \delta Z_2^{(q)}, \delta m_Q$

Table 2.2: List of IR divergent diagrams in the  $\mathcal{O}(\alpha_s)$  virtual corrections to the  $q\bar{q} \rightarrow Q\bar{Q}\gamma$  subprocess.

Classes	Diagrams
Bubbles	-
Triangles	$V_1^{(1,2,3,4;a,b)}, V_2^{(1,2;a)}, V_3^{(1,2)}$
Boxes	$B_1^{(2)}, B_2^{(1,2,3,4)}, B_3^{(1,2,3,4)}, B_4^{(1,2,3,4)}$
Pentagons	$P_{1,2,3,4}$
CTs	$\delta Z_2^{(q)}, \delta Z_2^{(Q)}$

$1 + \delta Z_i$ ) introduced to cancel the UV-singularities at  $\mathcal{O}(\alpha_s)$  according to renormalization schemes explained in the following.  $\sum |\mathcal{M}_0^{q\bar{q}}|^2$  is the LO matrix element squared of the  $q\bar{q}$  channel, given by Eq. 2.17, while  $\mathcal{N}_s$  and  $\mathcal{N}_Q$  are prefactors defined by

$$\mathcal{N}_s = \left( \frac{4\pi\mu^2}{s_{12}} \right)^\epsilon \Gamma(1+\epsilon) \quad \text{and} \quad \mathcal{N}_Q = \left( \frac{4\pi\mu^2}{m_Q^2} \right)^\epsilon \Gamma(1+\epsilon), \quad (2.32)$$

where  $s_{ij}$  denotes the generic kinematic invariant defined by

$$s_{ij} = 2p_i \cdot p_j. \quad (2.33)$$

The strong coupling constant  $\alpha_s$  is renormalized in the  $\overline{\text{MS}}$  scheme modified to decouple the heavy quark, i.e. the first  $n_{\text{lf}}$  light flavors are subtracted using the  $\overline{\text{MS}}$  scheme, while the divergences associated with the top-quark loop are subtracted at zero momentum:

$$\delta Z_{\alpha_s} = \frac{\alpha_s}{4\pi} (4\pi)^\epsilon \Gamma(1+\epsilon) \left\{ \left( \frac{2}{3} n_{\text{lf}} - \frac{11}{3} N \right) \frac{1}{\epsilon_{UV}} \right. \quad (2.34)$$

$$\left. + \delta_{b,Q} \frac{2}{3} \left[ \frac{1}{\epsilon_{UV}} + \ln \left( \frac{\mu^2}{m_Q^2} \right) \right] + \frac{2}{3} \left[ \frac{1}{\epsilon_{UV}} + \ln \left( \frac{\mu^2}{m_t^2} \right) \right] \right\}. \quad (2.35)$$

The wave-function renormalization constants for the external quark fields and the heavy-quark mass counterterm are calculated in the on-shell subtraction scheme, obtained by

imposing the following conditions:

$$\delta Z_2^{(q)} = \left. \frac{d\Sigma(\not{p})}{d\not{p}} \right|_{\not{p}=0}, \quad (2.36)$$

$$\delta Z_2^{(Q)} = \left. \frac{d\Sigma(\not{p})}{d\not{p}} \right|_{\not{p}=m_Q}, \quad (2.37)$$

$$\delta m_Q = \Sigma(\not{p} = m_Q), \quad (2.38)$$

where  $\Sigma(\not{p})$  is the self-energy correction for external quarks, and the corresponding renormalization constants are explicitly given by

$$\left( \delta Z_2^{(Q)} \right)_{UV} = \frac{\alpha_s}{4\pi} \mathcal{N}_Q \left( \frac{N}{2} - \frac{1}{2N} \right) \left( -\frac{1}{\epsilon_{UV}} - 4 \right), \quad (2.39)$$

$$\left( \delta Z_2^{(q)} \right)_{UV} = \frac{\alpha_s}{4\pi} \mathcal{N}_s \left( \frac{N}{2} - \frac{1}{2N} \right) \left( -\frac{1}{\epsilon_{UV}} \right), \quad (2.40)$$

$$\frac{\delta m_Q}{m_Q} = \frac{\alpha_s}{4\pi} \mathcal{N}_Q \left( \frac{N}{2} - \frac{1}{2N} \right) \left( -\frac{3}{\epsilon_{UV}} - 4 \right). \quad (2.41)$$

We notice that the sum of the UV-divergent contribution of the  $S_1$  diagrams do not completely factor out the LO amplitude, i.e.

$$\sum_j \Delta_{UV}^{q\bar{q}}(S_1^{(j)}) = \frac{\alpha_s}{4\pi} \mathcal{N}_Q \left[ \frac{N}{2} - \frac{1}{2N} \right] \left( -\frac{1}{\epsilon_{UV}} \right) \mathcal{A}_0^{q\bar{q}} + \hat{\mathcal{A}}_{S_1^{(1)}}^{UV} + \hat{\mathcal{A}}_{S_1^{(2)}}^{UV}, \quad (2.42)$$

where

$$\begin{aligned} \hat{\mathcal{A}}_{S_1^{(1)}}^{UV} &= -3m_Q \frac{eg_s^2 Q_Q}{s_{12}} t_{i_2 i_1}^a t_{i_3 i_4}^a [\bar{v}_2 \gamma^\mu u_1] \left[ \bar{u}_3 \not{\epsilon}_5^* \frac{\not{p}_3 + \not{p}_5 + m_Q}{(p_3 + p_5)^2 - m_Q^2} \frac{\not{p}_3 + \not{p}_5 + m_Q}{(p_3 + p_5)^2 - m_Q^2} \gamma_\mu v_4 \right] \\ &\quad \times \frac{\alpha_s}{4\pi} \mathcal{N}_Q \left[ \frac{N}{2} - \frac{1}{2N} \right] \left( -\frac{1}{\epsilon_{UV}} \right), \end{aligned} \quad (2.43)$$

$$\begin{aligned} \hat{\mathcal{A}}_{S_1^{(2)}}^{UV} &= -3m_t \frac{eg_s^2 Q_Q}{s_{12}} t_{i_2 i_1}^a t_{i_3 i_4}^a [\bar{v}_2 \gamma^\mu u_1] \left[ \bar{u}_3 \gamma_\mu \frac{-\not{p}_4 - \not{p}_5 + m_Q}{(p_4 + p_5)^2 - m_Q^2} \frac{-\not{p}_4 - \not{p}_5 + m_Q}{(p_4 + p_5)^2 - m_Q^2} \not{\epsilon}_5^* v_4 \right] \\ &\quad \times \frac{\alpha_s}{4\pi} \mathcal{N}_Q \left[ \frac{N}{2} - \frac{1}{2N} \right] \left( -\frac{1}{\epsilon_{UV}} \right), \end{aligned} \quad (2.44)$$

and  $e$ ,  $g_s$ , and  $Q_Q$  are the electric unit charge, the strong coupling, and the heavy-quark charge (in the unit of  $e$ ) respectively. The  $\hat{\mathcal{A}}_{S_1^{(1)}}^{UV}$ ,  $\hat{\mathcal{A}}_{S_1^{(2)}}^{UV}$  singularities are indeed cancelled

by including the heavy-quark mass counterterm in the self-energy diagrams  $S_1^{(1)}$  and  $S_1^{(2)}$ , and this has already been taken into account in Eq. 2.30. We also notice that the UV singularities in the virtual gluon correction to the quark-photon vertex (diagram  $V_3^{(1,2,3,4)}$  in Fig. 2.7) are exactly cancelled by the first term of Eq. 2.42, due to the corresponding Ward identity. The sum of UV-divergent contributions in the virtual diagrams and counterterms leaves Eq. 2.30 UV finite. We have also confirmed that the scale dependence of Eq. 2.30

follows Eq. 2.9.

Once the UV singularities have been extracted and cancelled using the outlined renormalization procedure, the  $\mathcal{O}(\alpha_s)$  virtual amplitude for the  $q\bar{q} \rightarrow Q\bar{Q}\gamma$  channel contains only IR singularities. The diagrams contributing to the IR singularities in this channel are listed in Table 2.2. Summing up all the IR-divergent contributions, the IR singular part is given by

$$2\mathcal{R}e \sum \overline{(\mathcal{M}_0^{q\bar{q}})^*} \mathcal{M}_{\text{virt}}^{q\bar{q}} \Big|_{IR} = \sum |\mathcal{M}_0^{q\bar{q}}|^2 \left\{ \sum_{i,j} \Delta_{IR}^{q\bar{q}}(V_i^{(j)} + B_i^{(j)} + P_i) + 2 \left[ \left( \delta Z_2^{(Q)} \right)_{IR} + \left( \delta Z_2^{(q)} \right)_{IR} \right] \right\}, \quad (2.45)$$

where

$$\begin{aligned} \sum_{i,j} \Delta_{IR}^{q\bar{q}}(V_i^{(j)} + B_i^{(j)} + P_i) &= \left( -\frac{1}{N} \right) \frac{\alpha_s}{2\pi} \mathcal{N}_Q \left\{ -\frac{1}{\epsilon_{IR}^2} + \frac{1}{\epsilon_{IR}} \left[ \frac{s_{34}}{\beta(s_{34} + 2m_Q^2)} \ln \left( \frac{1+\beta}{1-\beta} \right) \right. \right. \\ &\quad \left. \left. + 2 \ln \left( \frac{s_{13}s_{24}}{s_{14}s_{23}} \right) + \ln \left( \frac{s_{12}}{m_Q^2} \right) - 2 \right] \right\} \\ &\quad + N \frac{\alpha_s}{2\pi} \mathcal{N}_Q \left\{ -\frac{1}{\epsilon_{IR}^2} + \frac{1}{\epsilon_{IR}} \left[ \ln \left( \frac{s_{13}}{m_Q^2} \right) + \ln \left( \frac{s_{24}}{m_Q^2} \right) - 2 \right] \right\}, \\ \left( \delta Z_2^{(Q)} \right)_{IR} &= \frac{\alpha_s}{4\pi} \mathcal{N}_Q \left( \frac{N}{2} - \frac{1}{2N} \right) \left( -\frac{2}{\epsilon_{IR}} \right), \end{aligned} \quad (2.46)$$

$$\left( \delta Z_2^{(q)} \right)_{IR} = \frac{\alpha_s}{4\pi} \mathcal{N}_s \left( \frac{N}{2} - \frac{1}{2N} \right) \left( \frac{1}{\epsilon_{IR}} \right), \quad (2.47)$$

and we have introduced  $\beta$  as,

$$\beta = \sqrt{1 - \frac{4m_Q^2}{s_{34} + 2m_Q^2}}. \quad (2.48)$$

### 2.3.2 $\mathcal{O}(\alpha_s)$ virtual corrections to $gg \rightarrow Q\bar{Q}\gamma$

As for the  $q\bar{q}$ -initiated subprocess, the  $\mathcal{O}(\alpha_s)$  virtual corrections to  $gg \rightarrow Q\bar{Q}\gamma$  consist of the bubble, triangle, box, and pentagon diagrams shown in Figs. 2.11-2.15. The appearance of gluons as external particles generates more diagrams compared to the  $q\bar{q}$ -initiated subprocess due to possibility of having the three- and four-gluon self interactions. The vanishing triangle diagrams are shown in Fig. 2.12. The  $gg$ -initiated virtual diagrams that contribute to the UV singularities are listed in Table 2.3. The UV-divergent contributions are given by

$$\begin{aligned} 2\mathcal{R}e \sum \overline{(\mathcal{M}_0^{gg})^*} \mathcal{M}_{\text{virt}}^{gg} \Big|_{UV} &= 2\mathcal{R}e \sum \sum_{i,j} \overline{(\mathcal{M}_0^{gg})^*} \left( \mathcal{M}_{S_i^{(j)}} + \mathcal{A}_{V_i^{(j)}} \right)_{UV} \\ &\quad + 2 \left[ \left( \delta Z_2^{(Q)} \right)_{UV} + \delta Z_{\alpha_s} + \delta Z_3 + \delta_{UV} \right] \sum |\mathcal{M}_0^{gg}|^2, \end{aligned} \quad (2.49)$$

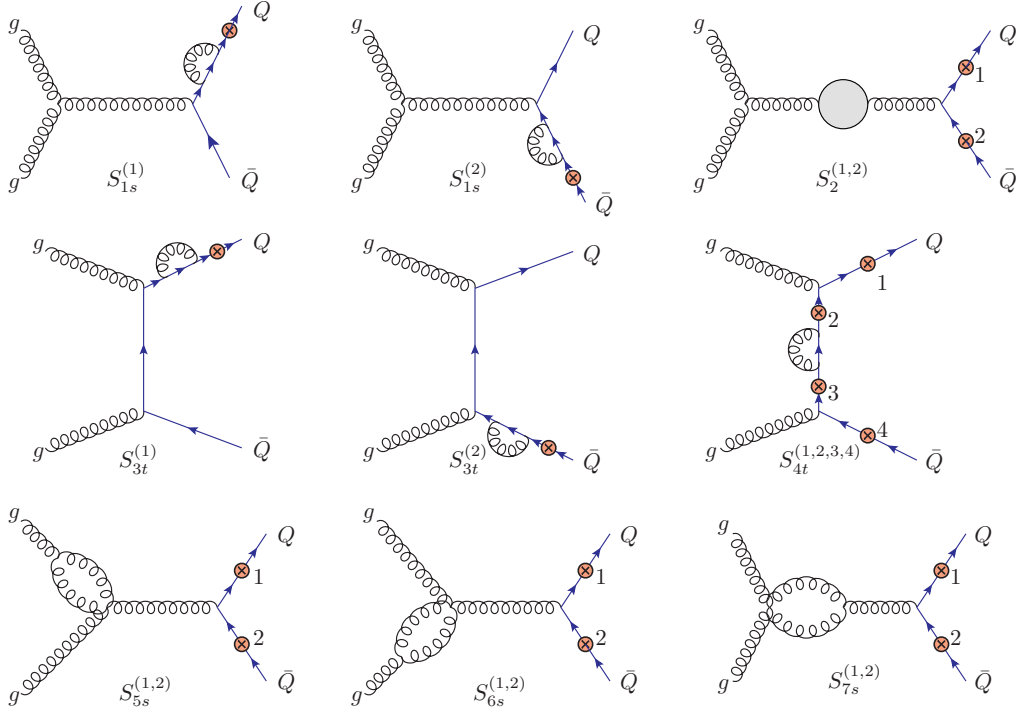


Figure 2.11:  $\mathcal{O}(\alpha_s)$  bubble-diagram corrections to the  $gg \rightarrow Q\bar{Q}\gamma$  subprocess. The red-circled crosses correspond to all possible photon insertions. The shaded blob represents the gluonic, quark, and ghost loop corrections to the gluon propagator. The  $u$ -channel diagrams are obtained from the  $t$ -channel diagrams by exchanging the initial state gluons.

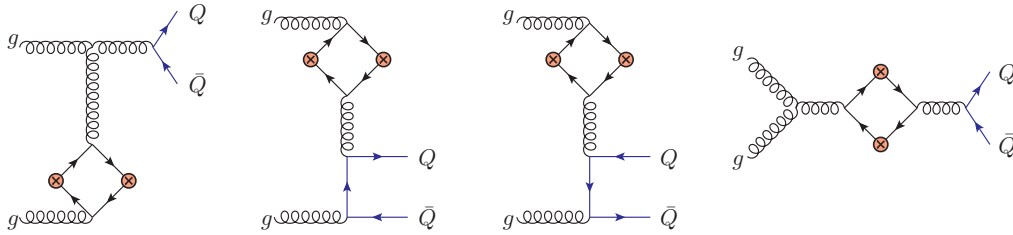


Figure 2.12: Vanishing  $\mathcal{O}(\alpha_s)$  triangle-diagrams in the  $gg \rightarrow Q\bar{Q}\gamma$  subprocess. The red-circled crosses correspond to all possible photon insertions.

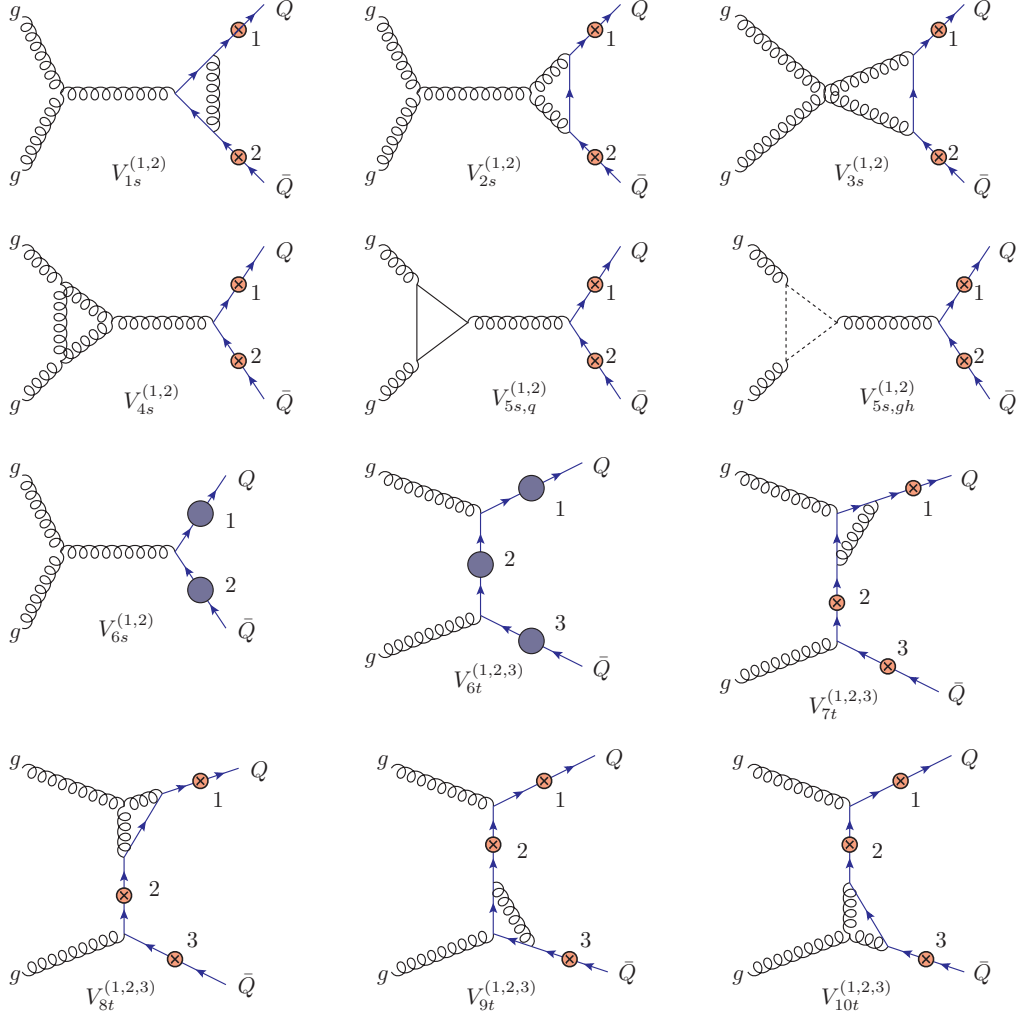


Figure 2.13:  $\mathcal{O}(\alpha_s)$  triangle-diagram corrections to the  $gg \rightarrow Q\bar{Q}\gamma$  subprocess. The red-circled crosses correspond to all possible photon insertions while the blue blobs represent QCD correction to the quark-photon vertex as shown in Fig. 2.7. The  $u$ -channel diagrams are obtained from the  $t$ -channel diagrams by exchanging the initial state gluons.



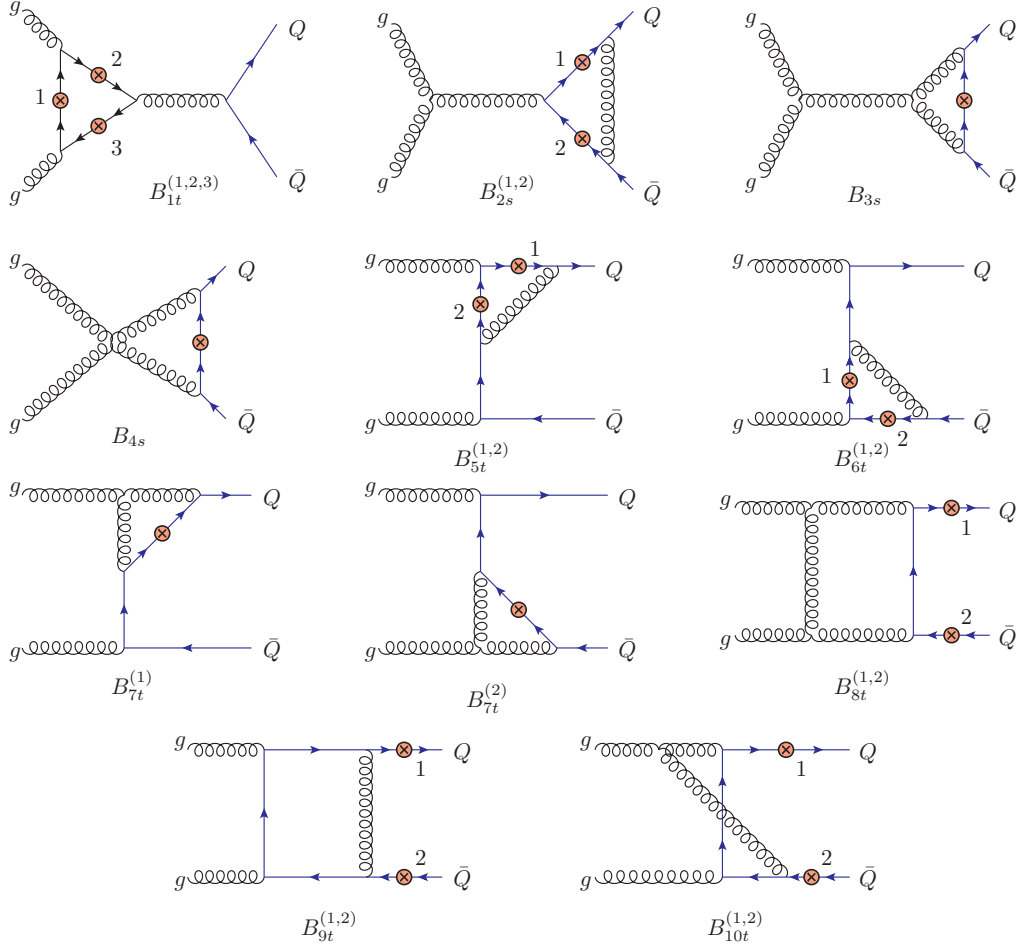


Figure 2.14:  $\mathcal{O}(\alpha_s)$  box-diagram corrections to the  $gg \rightarrow Q\bar{Q}\gamma$  subprocess. The red-circled crosses correspond to all possible photon insertions. The  $u$ -channel diagrams are obtained from the  $t$ -channel diagrams by exchanging the initial state gluons.

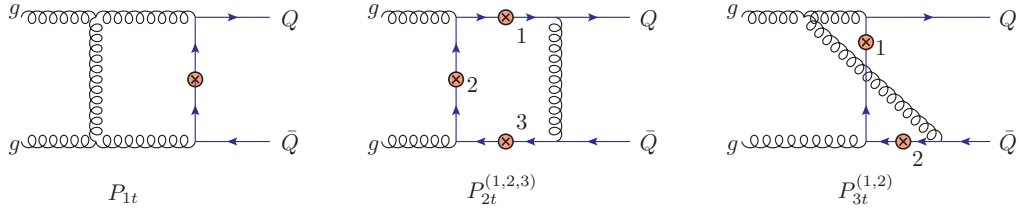


Figure 2.15:  $\mathcal{O}(\alpha_s)$  pentagon-diagram corrections to the  $gg \rightarrow Q\bar{Q}\gamma$  subprocess. The red-circled crosses correspond to all possible photon insertions. The  $u$ -channel diagrams are obtained from the  $t$ -channel diagrams by exchanging the initial state gluons.

Table 2.3: List of UV divergent diagrams in the  $\mathcal{O}(\alpha_s)$  virtual corrections to the  $gg \rightarrow Q\bar{Q}\gamma$  subprocess.

Classes	Diagrams
Bubbles	$S_{1,2,5,6,7;s}^{(1,2)}, S_{3;t,u}^{(1,2)}, S_{4;t,u}^{(1,2,3,4)}$
Triangles	$V_{1,2,4,5q,5gh;s}^{(1,2)}, V_{7,8,9,10;t,u}^{(1,2,3)}$
Boxes	-
Pentagons	-
CTs	$\delta Z_3, \delta Z_2^{(Q)}, \delta Z_{\alpha_s}, \delta m_Q$

Table 2.4: List of IR divergent diagrams in the  $\mathcal{O}(\alpha_s)$  virtual corrections to the  $gg \rightarrow Q\bar{Q}\gamma$  subprocess.

Classes	Diagrams
Bubbles	-
Triangles	$V_{4;s}^{(1,2)}, V_{8,10;t,u}^{(1,2,3)}$
Boxes	$P_{2;s}^{(1,2)}, P_{7,8,10;t,u}^{(1,2)}$
Pentagons	$P_{1;t,u}, P_{2;t,u}^{(1,2,3)}, P_{3;t,u}^{(1,2)}$
CTs	$\delta Z_3, \delta Z_2^{(Q)}$

where

$$\left(\mathcal{M}_{S_{2;s}^{(1,2)}}\right)_{UV} = \frac{\alpha_s}{4\pi} \frac{1}{\epsilon_{UV}} \left\{ \mathcal{N}_s \left( \frac{5N}{3} - \frac{2n_{\text{lf}}}{3} \right) - \mathcal{N}_Q \frac{2}{3} \right\} [t^a, t^b] \mathcal{A}_{0,s}, \quad (2.50)$$

$$\begin{aligned} & \left( \mathcal{M}_{S_{1,2;s}^{(1,2)}} + \mathcal{M}_{S_{3;t,u}^{(1,2)}} + \mathcal{M}_{S_{4;t,u}^{(1,2,3,4)}} \right)_{UV} = -\frac{\alpha_s}{4\pi} \frac{\mathcal{N}_Q}{\epsilon_{UV}} \left( \frac{N}{2} - \frac{1}{2N} \right) \left\{ \mathcal{M}_0^{gg} + [t^a, t^b] \frac{1}{2} (\mathcal{A}_{0,t} - \mathcal{A}_{0,u}) \right. \\ & \quad \left. + \left\{ t^a, t^b \right\} \frac{1}{2} (\mathcal{A}_{0,t} + \mathcal{A}_{0,u}) \right\} \\ & \quad + \hat{\mathcal{A}}_{S_{1;s}^{(1,2)}}^{UV} + \hat{\mathcal{A}}_{S_{3;t,u}^{(1,2)}}^{UV} + \hat{\mathcal{A}}_{S_{4;t,u}^{(1,2,3,4)}}^{UV}, \end{aligned} \quad (2.51)$$

$$\begin{aligned} & \left( \mathcal{M}_{V_{1,2;s}^{(1,2)}} + \mathcal{M}_{V_{7,8,9,10;t,u}^{(1,2,3)}} \right)_{UV} = \frac{\alpha_s}{4\pi} \frac{\mathcal{N}_Q}{\epsilon_{UV}} \left( \frac{3N}{2} - \frac{1}{2N} \right) \left\{ \mathcal{M}_0^{gg} + [t^a, t^b] \frac{1}{2} (\mathcal{A}_{0,t} - \mathcal{A}_{0,u}) \right. \\ & \quad \left. + \left\{ t^a, t^b \right\} \frac{1}{2} (\mathcal{A}_{0,t} + \mathcal{A}_{0,u}) \right\}, \end{aligned} \quad (2.52)$$

$$\left( \mathcal{M}_{S_{5,6,7;s}^{(1,2)}} + \mathcal{M}_{V_{4,5q,5gh;s}^{(1,2)}} \right)_{UV} = \frac{\alpha_s}{4\pi} \frac{1}{\epsilon_{UV}} \left\{ \mathcal{N}_s \left( -\frac{2N}{3} + \frac{2n_{\text{lf}}}{3} \right) + \mathcal{N}_Q \frac{2}{3} \right\} [t^a, t^b] \mathcal{A}_{0,s}, \quad (2.53)$$

$$\left( \mathcal{M}_{V_{6;s}^{(1,2)}} + \mathcal{M}_{V_{6;t,u}^{(1,2,3)}} \right)_{UV} = \frac{\alpha_s}{4\pi} \frac{\mathcal{N}_Q}{\epsilon_{UV}} \left( \frac{N}{2} - \frac{1}{2N} \right) \mathcal{M}_0^{gg}. \quad (2.54)$$

Here the UV-singular contributions depend on the color correlation of the LO amplitudes. The LO amplitudes,  $\mathcal{M}_0^{gg}$  and  $\mathcal{A}_{0;s,t,u}$  are given by Eqs. 2.14 and 2.16. Similar to the  $q\bar{q}$ -initiated virtual subprocess, the UV-singularities due to the virtual gluon corrections to the quark-photon vertex (diagrams  $V_{6s}^{(1,2)}$ ,  $V_{6;t,u}^{(1,2,3)}$  in Fig. 2.13) are exactly cancelled by the first term of Eq. 2.51. We also include the heavy-quark mass counterterm, given by Eq. 2.41, into the self-energy corrections in diagram  $S_{1s}^{(1,2)}$ ,  $S_{3;t,u}^{(1,2)}$ ,  $S_{4;t,u}^{(1,2,3,4)}$ , in order to cancel UV-singularities that do not factor out completely from the LO amplitudes as explained in Sec. 2.3.1.  $\delta Z_{\alpha_s}$  and  $\delta Z_2^{(Q)}$  are given by Eqs. 2.35 and 2.39, respectively. The external-gluon wavefunction renormalization constant is computed in the  $\overline{\text{MS}}$  scheme, and is given by

$$(\delta Z_3)_{UV} = \frac{\alpha_s}{4\pi}(4\pi)^\epsilon \Gamma(1+\epsilon) \left\{ \left( \frac{5}{3}N - \frac{2}{3}n_{\text{lf}} \right) \frac{1}{\epsilon_{UV}}, \right. \\ \left. -\delta_{b,Q} \frac{2}{3} \left[ \frac{1}{\epsilon_{UV}} + \ln \left( \frac{\mu^2}{m_Q^2} \right) \right] - \frac{2}{3} \left[ \frac{1}{\epsilon_{UV}} + \ln \left( \frac{\mu^2}{m_t^2} \right) \right] \right\}, \quad (2.55)$$

with the extra caveat that a finite self-energy correction  $\delta_{UV}$  needs to be inserted for the gluon external legs,

$$\delta_{UV} = \frac{\alpha_s}{4\pi}(4\pi)^\epsilon \Gamma(1+\epsilon) \left( \frac{5}{3}N - \frac{2}{3}n_{\text{lf}} \right) \ln \left( \frac{\mu^2}{m_Q^2} \right). \quad (2.56)$$

The sum of UV-divergent contributions and counterterms leaves Eq. 2.49 UV finite, and one can verify that the scale dependence of Eq. 2.49 agrees with Eq. 2.9.

Switching the discussion to the IR-singularities, the diagrams contributing to the IR singularities in this channel are listed in Table 2.4. The IR singular part is given by

$$2\mathcal{R}e \overline{\sum} (\mathcal{M}_0^{gg})^* \mathcal{M}_{\text{virt}}^{gg} |_{IR} = \sum_{i,j} \Delta_{IR}^{gg} (V_i^{(j)} + B_i^{(j)} + P_i^{(j)}) \\ + 2 \left[ \left( \delta Z_2^{(Q)} \right)_{IR} + (\delta Z_3)_{IR} \right] \overline{\sum} |\mathcal{M}_0^{gg}|^2 \\ = \frac{\alpha_s}{2\pi} \mathcal{N}_Q \overline{\sum} (C_1 \mathcal{A}_\epsilon^{C_1} + C_2 \mathcal{A}_\epsilon^{C_2} + C_3 \mathcal{A}_\epsilon^{C_3}) \\ + \frac{\alpha_s}{2\pi} \mathcal{N}_Q \left( \frac{2}{3}n_{\text{lf}} - \frac{8}{3}N + \frac{1}{N} \right) \frac{1}{\epsilon_{IR}} \overline{\sum} |\mathcal{M}_0^{gg}|^2, \quad (2.57)$$

where we have organized the result according to three color factors,

$$C_1 = \frac{N^2}{4} (N^2 - 1), \\ C_2 = -\frac{1}{4} (N^2 - 1), \\ C_3 = \left( 1 + \frac{1}{N^2} \right) (N^2 - 1), \quad (2.58)$$

and the corresponding amplitudes, given by:

$$\begin{aligned}\mathcal{A}_\epsilon^{C_1} = & \left[ -\frac{4}{\epsilon_{IR}} + \frac{2}{\epsilon_{IR}} \left( -2 + \ln \left( \frac{s_{12}}{m_Q^2} \right) \right) \right] \cdot \left\{ |\mathcal{A}_0^{nab}|^2 + |\mathcal{A}_0^{ab}|^2 \right\} \\ & + \frac{1}{\epsilon_{IR}} \left[ \ln \left( \frac{s_{13}}{m_Q^2} \right) + \ln \left( \frac{s_{24}}{m_Q^2} \right) \right] \cdot |\mathcal{A}_{0,s} + \mathcal{A}_{0,t}|^2 \\ & + \frac{1}{\epsilon_{IR}} \left[ \ln \left( \frac{s_{14}}{m_Q^2} \right) + \ln \left( \frac{s_{23}}{m_Q^2} \right) \right] \cdot |\mathcal{A}_{0,s} - \mathcal{A}_{0,t}|^2, \end{aligned} \quad (2.59)$$

$$\begin{aligned}\mathcal{A}_\epsilon^{C_2} = & \left\{ -\frac{8}{\epsilon_{IR}^2} + \frac{4}{\epsilon_{IR}} \left[ -2 + \ln \left( \frac{s_{13}}{m_Q^2} \right) + \ln \left( \frac{s_{14}}{m_Q^2} \right) + \ln \left( \frac{s_{23}}{m_Q^2} \right) + \ln \left( \frac{s_{24}}{m_Q^2} \right) \right] \right\} \cdot |\mathcal{A}_0^{ab}|^2 \\ & + \frac{2}{\epsilon_{IR}} \frac{s_{34}\Lambda}{(s_{34} + 2m_Q^2)\beta} \cdot \left\{ |\mathcal{A}_0^{nab}|^2 + |\mathcal{A}_0^{ab}|^2 \right\}, \end{aligned} \quad (2.60)$$

$$\mathcal{A}_\epsilon^{C_3} = \frac{1}{\epsilon_{IR}} \frac{s_{34}\Lambda}{(s_{34} + 2m_Q^2)\beta} \cdot |\mathcal{A}_0^{ab}|^2, \quad (2.61)$$

where

$$\Lambda = \ln \left( \frac{1 + \beta}{1 - \beta} \right), \quad (2.62)$$

and  $\beta$  is defined in Eq. 2.48.  $\mathcal{A}_0^{ab}$  and  $\mathcal{A}_0^{nab}$  are given by Eq. 2.15.

## 2.4 $\mathcal{O}(\alpha_s)$ real corrections to $pp(p\bar{p}) \rightarrow Q\bar{Q}\gamma$ production

The  $\mathcal{O}(\alpha_s)$  real corrections to  $pp(p\bar{p}) \rightarrow Q\bar{Q}\gamma$  production consist of three subprocesses,

$$\begin{aligned}q\bar{q} & \rightarrow Q\bar{Q}\gamma + g, \\ gg & \rightarrow Q\bar{Q}\gamma + g, \\ qg(\bar{q}g) & \rightarrow Q\bar{Q}\gamma + q(\bar{q}).\end{aligned}$$

In addition to the  $q\bar{q}$ - and  $gg$ -initiated subprocesses that also appear in the LO process and the  $\mathcal{O}(\alpha_s)$  virtual corrections, the  $qg$ - and  $\bar{q}g$ -initiated subprocesses open up at tree level in the  $\mathcal{O}(\alpha_s)$  real corrections and at this order (NLO) they do not have virtual counter-parts. From here on in this thesis, the  $qg$  notation will include both the  $qg$  and the  $\bar{q}g$  channels. Some representative Feynman diagrams for the three subprocesses are shown in Fig. 2.16. In this section, we will use the same momenta and color index assignments as in Eqs. 2.10 and 2.11, with the addition of an extra parton momentum,

$$i(p_1) + j(p_2) \rightarrow Q(p_3) + \bar{Q}(p_4) + \gamma(p_5) + f_k(k). \quad (2.63)$$

where  $i$  and  $j$  are the initial state partons that include  $q\bar{q}$ ,  $gg$ , and  $qg(\bar{q}g)$ , while  $f_k$  corresponds to the extra parton that is emitted in the process ( $g/q/\bar{q}$ ) depending on the initial state partons. These real-correction diagrams suffer from IR singularities when,

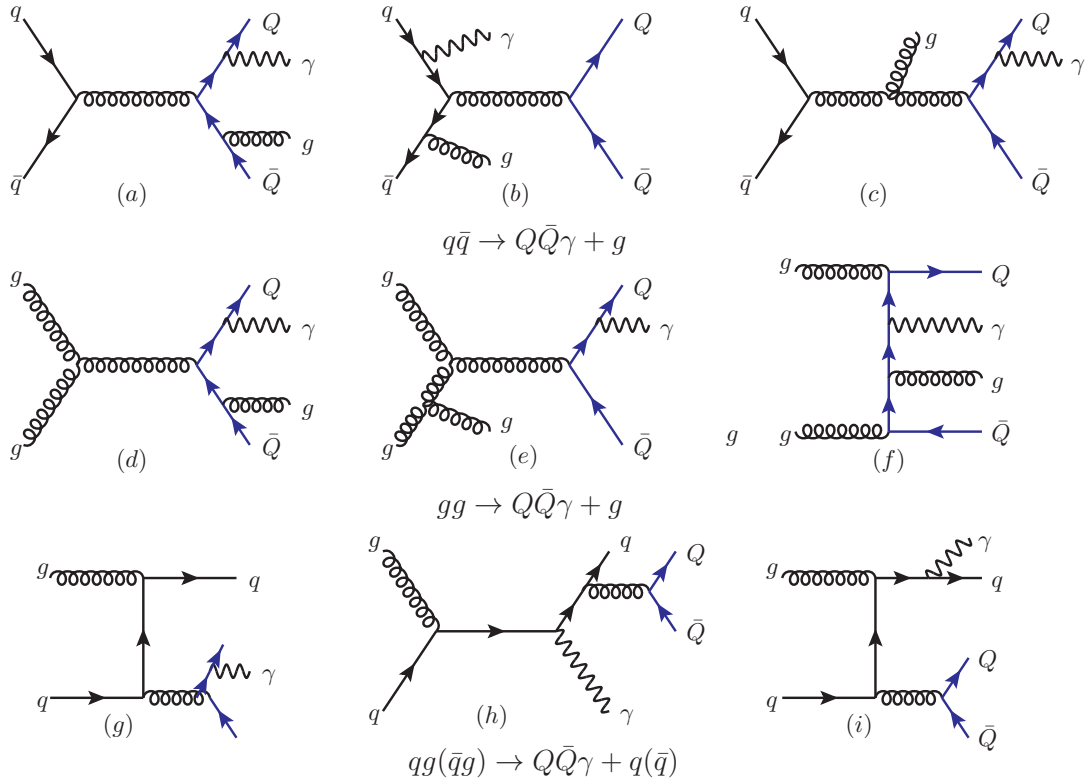


Figure 2.16: Examples of  $\mathcal{O}(\alpha_s)$  real-emission corrections to  $Q\bar{Q}\gamma$  production in all three channels:  $q\bar{q} \rightarrow Q\bar{Q}\gamma + g$  (diagrams *a*, *b*, *c*),  $gg \rightarrow Q\bar{Q}\gamma + g$  (diagrams *d*, *e*, *f*), and  $qg(\bar{q}g) \rightarrow Q\bar{Q}\gamma + q(\bar{q})$  (diagrams *g*, *h*, *i*).

- a gluon emitted from an external heavy-quark line becomes soft (diagrams *a* and *d* in Fig. 2.16),
- a gluon emitted by an external massless-quark or gluon becomes soft and/or collinear with the emitter parton (diagrams *b* and *e* in Fig. 2.16),
- a  $q\bar{q}$  pair that comes from the splitting of an initial state gluon becomes collinear, where, either  $q$  or  $\bar{q}$  is a final state particle (diagram *g* in Fig. 2.16),
- a photon emitted from a massless final state quark line becomes collinear with the emitter quark (diagram *i* in Fig. 2.16).

In this section we focus on the first three cases while the treatment of the last case will be discussed in Sec. 2.5. To extract the QCD-originated IR singularities we use the two-cutoff Phase Space Slicing method (PSS2 method, see Ref. [85] for a detailed review). In order to illustrate how the phase-space-slicing method works in general, let us consider a one-dimensional example [86], e.g.

$$\mathcal{I} = \int_0^1 \frac{dx}{x} x^{-\epsilon} \mathcal{M}(x). \quad (2.64)$$

We can imagine that the integral represents the integration over a phase space variable of the extra parton emitted in a generic real correction.  $x$  could correspond to the gluon energy or the angle between two (collinear) partons. The factor of  $x^{-\epsilon}$  regularizes the divergence as  $x \rightarrow 0$  ( $\epsilon < 0$ ) and allows us to extract the existing singularities as poles in  $\epsilon$ . The real-emission matrix element,  $\mathcal{M}(x)$ , factorizes into the tree-level matrix element,  $\mathcal{M}(0)$ , multiplied by a universal singular function as  $x \rightarrow 0$ . To isolate the singular region of the integration, a parameter  $\delta$  is introduced. In the singular region, the factorized form of the matrix element is used. The integration now becomes,

$$\begin{aligned} \mathcal{I} &= \mathcal{M}(0) \int_0^\delta \frac{dx}{x} x^{-\epsilon} + \int_\delta^1 \frac{dx}{x} \mathcal{M}(x), \\ &= -\frac{1}{\epsilon} \delta^{-\epsilon} \mathcal{M}(0) + \int_\delta^1 \frac{dx}{x} \mathcal{M}(x), \\ &= \left( -\frac{1}{\epsilon} + \ln(\delta) \right) \mathcal{M}(0) + \int_\delta^1 \frac{dx}{x} \mathcal{M}(x), \end{aligned} \quad (2.65)$$

where we have expanded  $\delta^{-\epsilon}$  in the singular region and take  $\epsilon = 0$  in the non-singular region. The singularity in  $\mathcal{I}$  manifests itself as a  $1/\epsilon$  pole, while the remaining finite term can be integrated numerically. The final result, of course, should not depend on the slicing parameter  $\delta$ .

Returning to the calculation of the real corrections to  $Q\bar{Q}\gamma$  production at hadron colliders, the real-emission cross section can be written as:

$$d\hat{\sigma}_{ij}^{\text{real}} = dPS(Q\bar{Q}\gamma + f_k) \sum |\mathcal{M}(ij \rightarrow Q\bar{Q}\gamma + f_k)|^2. \quad (2.66)$$

We consider first the form of the matrix elements in the soft and collinear limits.

## 1. Soft limit

In the soft gluon limit, where  $E_g = k^0 \rightarrow 0$ , the real-emission matrix element factorizes to the eikonal current multiplied by the LO amplitude,

$$\mathcal{M}^c(ij \rightarrow Q\bar{Q}\gamma + g)_{\text{soft}} \simeq g_s \mu^\epsilon \left( \sum_{f=1}^4 \mathbf{T}_f^c \frac{p_f \cdot \varepsilon^*(k)}{p_f \cdot k} \right) \mathbf{M}(ij \rightarrow Q\bar{Q}\gamma), \quad (2.67)$$

where  $c$  is the color index of the emitted gluon and  $\mathbf{M}(ij \rightarrow Q\bar{Q}\gamma)$  is the LO color-correlated amplitude. The sum corresponds to the soft gluon that is emitted from the four external partons in turn.  $\mathbf{T}_f^c$  is the  $SU(N)$  color charge associated with the emitting parton  $f$ . If the emitting parton is a final state quark or an initial state anti-quark, the color charge is in the fundamental representation,  $(T^a)_{ij} = t_{ij}^a$ ,  $(i, j = 1, \dots, N)$ . For a final state anti-quark or an initial state quark,  $(T^a)_{ij} = -t_{ij}^a$ . If the emitting parton is a gluon, the color charge is in the adjoint representation,  $(T^a)_{bc} = if_{abc}$ . Squaring Eq. 2.67 and summing over the gluon polarizations gives:

$$\overline{\sum} |\mathcal{M}(ij \rightarrow Q\bar{Q}\gamma + g)|_{\text{soft}}^2 \simeq (4\pi\mu^{2\epsilon}\alpha_s) \sum_{f,f'=1}^4 \left( -\frac{p_f \cdot p_{f'}}{p_f \cdot k \ p_{f'} \cdot k} \right) \mathcal{M}_{ff'}(ij \rightarrow Q\bar{Q}\gamma), \quad (2.68)$$

where

$$\mathcal{M}_{ff'}(ij \rightarrow Q\bar{Q}\gamma) = (\mathbf{T}_f^c \mathbf{M})(\mathbf{T}_{f'}^c \mathbf{M})^\dagger, \quad (2.69)$$

is the color-connected LO amplitude squared. On the other hand, the  $Q\bar{Q}\gamma + g$  phase-space factor in the soft-gluon limit has the following form,

$$dPS(Q\bar{Q}\gamma + f_k)_{\text{soft}} \simeq dPS(Q\bar{Q}\gamma) \frac{d^{d-1}k}{(2\pi)^{d-1}2k^0}. \quad (2.70)$$

The real-emission cross section in the soft limit then becomes,

$$\begin{aligned} d\hat{\sigma}_{ij}^{\text{real}}|_{\text{soft}} &\simeq (4\pi\mu^{2\epsilon}\alpha_s) dPS(Q\bar{Q}\gamma) \frac{d^{d-1}k}{(2\pi)^{d-1}2k^0} \\ &\times \sum_{f,f'=1}^4 \left( -\frac{p_f \cdot p_{f'}}{p_f \cdot k \ p_{f'} \cdot k} \right) \mathcal{M}_{ff'}(ij \rightarrow Q\bar{Q}\gamma). \end{aligned} \quad (2.71)$$

## 2. Collinear limit

Suppose that the initial parton  $i$  splits into a pair of parton  $i' + f_k$ . In the collinear limit, where  $\cos\theta_{ik} \rightarrow 0$ , the factorization of the matrix elements and the four-body phase-space factor, with  $p_{i'} = zp_i$  and  $k = (1-z)p_i$  are

$$\overline{\sum} |\mathcal{M}(ij \rightarrow Q\bar{Q}\gamma + f_k)|_{\text{coll}}^2 \simeq (4\pi\mu^{2\epsilon}\alpha_s) \overline{\sum} |\mathcal{M}(i'j \rightarrow Q\bar{Q}\gamma)|^2 \frac{2P_{ii'}(z)}{zs_{ik}}, \quad (2.72)$$

$$dPS(Q\bar{Q}\gamma + k)_{\text{coll}} \simeq dPS(Q\bar{Q}\gamma) z \frac{d^{d-1}k}{(2\pi)^{d-1}2k^0}, \quad (2.73)$$

$$\begin{aligned} &= dPS(Q\bar{Q}\gamma) \frac{\Gamma(1-\epsilon)}{\Gamma(1-2\epsilon)} \frac{(4\pi)^\epsilon}{16\pi^2} \\ &\times z \, dz \, ds_{ik} [(1-z)s_{ik}]^{-\epsilon}, \end{aligned} \quad (2.74)$$

Table 2.5: All possible splittings of initial partons to be included in the calculation of the collinear cross section. For the  $i \rightarrow jk$  splitting process, the splitting function is given by  $P_{ij}(z)$ .

Subprocesses	Splitting	Emitting Leg(s)
$q\bar{q} \rightarrow Q\bar{Q}\gamma + g$	$q \rightarrow qg$	1
	$\bar{q} \rightarrow \bar{q}g$	2
$gg \rightarrow Q\bar{Q}\gamma + g$	$g \rightarrow gg$	1 and 2
$qg \rightarrow Q\bar{Q}\gamma + q$	$q \rightarrow gq$	1
	$g \rightarrow \bar{q}q$	2
$\bar{q}g \rightarrow Q\bar{Q}\gamma + \bar{q}$	$\bar{q} \rightarrow g\bar{q}$	1
	$g \rightarrow q\bar{q}$	2

where we have substituted  $d = 4 - 2\epsilon$  in Eq. 2.73. The real emission cross section in the collinear limit becomes

$$d\hat{\sigma}_{ij}^{\text{real}}|_{\text{coll}} \simeq (4\pi\mu^{2\epsilon}\alpha_s) \frac{\Gamma(1-\epsilon)}{\Gamma(1-2\epsilon)} \frac{(4\pi)^\epsilon}{16\pi^2} dPS(Q\bar{Q}\gamma) dz \quad (2.75)$$

$$\times \sum_i ds_{ik} [(1-z)s_{ik}]^{-\epsilon} \frac{2P_{ii'}(z)}{s_{ik}} \overline{\sum} |\mathcal{M}(i'j \rightarrow Q\bar{Q}\gamma)|^2.$$

In Table 2 we list all possible splittings of the initial partons that have to be taken into account when computing the collinear cross section.

Implementing the PSS2 method into our  $pp(p\bar{p}) \rightarrow Q\bar{Q}\gamma$  calculation, the real correction cross section is divided into the soft ( $d\hat{\sigma}_{ij}^s$ ), hard/collinear ( $d\hat{\sigma}_{ij}^{\text{hc}}$ ), and hard/noncollinear ( $d\hat{\sigma}_{ij}^{\text{hnc}}$ ) pieces,

$$d\hat{\sigma}_{ij}^{\text{real}} = d\hat{\sigma}_{ij}^s + d\hat{\sigma}_{ij}^{\text{hc}} + d\hat{\sigma}_{ij}^{\text{hnc}}. \quad (2.76)$$

The soft and collinear regions of the phase space are defined by the soft and collinear cutoffs,  $\delta_s$  and  $\delta_c$ , respectively. In the following, we will discuss the soft, hard/collinear and hard/noncollinear cross sections in more detail.

- **Real correction,  $ij \rightarrow Q\bar{Q}\gamma + f_k$ : soft region**

The soft cross section,  $d\hat{\sigma}_{ij}^s$ , only receives contributions from the  $q\bar{q}$ - and  $gg$ -initiated subprocesses, thus  $f_k = g$ . The soft region of the  $ij \rightarrow Q\bar{Q}\gamma + g$  phase space is defined by requiring that the energy of the emitted gluon satisfies

$$k^0 < \delta_s \frac{\sqrt{s_{12}}}{2}. \quad (2.77)$$

The integration over the emitted gluon phase space in Eq. 2.71 is carried out in  $d = 4 - 2\epsilon$  dimensions, in order to extract the IR singularities as poles in  $\epsilon$ , with the



condition in Eq. 2.77 imposed. The integrals needed to perform the energy and angular integration in  $d$ -dimension are given in [85, 87]. Since the IR singularity structures of the  $\mathcal{O}(\alpha_s)$  real corrections to  $Q\bar{Q}\gamma$  hadroproduction are exactly the same as for the  $Q\bar{Q}h$  hadroproduction, we will take all the corresponding results from the calculation of  $Q\bar{Q}h$  hadroproduction at NLO QCD [88, 89]. After integrating the eikonal current over  $k$  as in Eq. 2.71, for both the  $q\bar{q}$ - and  $gg$ -initiated subprocesses, one obtains:

$$d\hat{\sigma}_{q\bar{q}}^s = dPS(Q\bar{Q}\gamma) \frac{\alpha_s}{2\pi} \mathcal{N}_Q \sum \overline{|\mathcal{M}_0^{q\bar{q}}|^2} \left\{ \frac{X_{-2}^s}{\epsilon_{IR}^2} + \frac{X_{-1}^s}{\epsilon_{IR}} + NC_1^s + \frac{C_2^s}{N} \right\}, \quad (2.78)$$

$$d\hat{\sigma}_{gg}^s = dPS(Q\bar{Q}\gamma) \frac{\alpha_s}{2\pi} \mathcal{N}_Q \sum \overline{\left\{ C_1(\mathcal{M}_{S,\epsilon}^{(1)} + \mathcal{M}_S^{(1)}) + C_2(\mathcal{M}_{S,\epsilon}^{(2)} + \mathcal{M}_S^{(2)}) \right.}} \\ \left. + C_3(\mathcal{M}_{S,\epsilon}^{(3)} + \mathcal{M}_S^{(3)}) \right\}, \quad (2.79)$$

where  $X_{-2}^s$ ,  $X_{-1}^s$ ,  $C_1^s$ , and  $C_2^s$  are given in Eq. 34 of [88], while  $\mathcal{M}_{S,\epsilon}^{(1,2,3)}$  and  $\mathcal{M}_S^{(1,2,3)}$  are given in Eqs. 39 and 42 of [89].  $C_{1,2,3}$  are given in Eq. 2.58. We notice that the IR singularities in the virtual amplitudes, Eqs. 2.45 and 2.57, are cancelled by the corresponding singularities in the real corrections, Eqs. 2.78 and 2.79.

- **Real correction,  $ij \rightarrow Q\bar{Q}\gamma + f_k$ : hard/collinear region**

The hard/collinear region of the  $ij \rightarrow Q\bar{Q}\gamma + f_k$  phase space is defined by requiring that the energy of the emitted parton satisfies

$$k^0 > \delta_s \frac{\sqrt{s_{12}}}{2}, \quad (2.80)$$

and one of the following conditions on the angle between the initial and emitted parton is satisfied:

$$\begin{aligned} 1 - \cos \theta_{1k} &< \delta_c, \\ 1 - \cos \theta_{2k} &< \delta_c. \end{aligned} \quad (2.81)$$

Note that the soft singularity does not present in the  $gg$ -initiated subprocess, thus the energy of the emitted parton satisfies  $k^0 > 0$  instead of Eq. 2.80. Performing the integration over  $z$  and  $s_{ik}$  in Eq. 2.75, one obtains:

$$d\hat{\sigma}_{q\bar{q},gg}^{\text{hc}} = \frac{\alpha_s}{2\pi} \mathcal{N}_Q \left[ -\frac{1}{\epsilon} + \ln \delta_c \right] \quad (2.82)$$

$$\left\{ \int_0^{1-\delta_s} dz \left[ \frac{(1-z)^2}{2z} \frac{s_{i'j}}{m_Q^2} \right]^{-\epsilon} P_{ii'}(z) d\hat{\sigma}_{q\bar{q},gg}^{\text{LO}}(i'j \rightarrow Q\bar{Q}\gamma) + (i \leftrightarrow j) \right\},$$

$$d\hat{\sigma}_{gg}^{\text{hc}} = \frac{\alpha_s}{2\pi} \mathcal{N}_Q \left[ -\frac{1}{\epsilon} + \ln \delta_c \right] \int_0^1 dz \left[ \frac{(1-z)^2}{2z} \frac{s_{i'j}}{m_Q^2} \right]^{-\epsilon} \quad (2.83)$$

$$\left\{ P_{qg}(z) d\hat{\sigma}_{gg}^{\text{LO}}(g(p_{1'})g(p_2) \rightarrow Q\bar{Q}\gamma) + P_{gq}(z) d\hat{\sigma}_{q\bar{q}}^{\text{LO}}(q(p_1)\bar{q}(p_{2'}) \rightarrow Q\bar{Q}\gamma) \right\}.$$

- Real correction,  $ij \rightarrow Q\bar{Q}\gamma + f_k$ : hard/noncollinear region

The remaining real-emission cross section to be calculated in the PSS2 method is the hard/noncollinear contribution. The hard/noncollinear region of the  $ij \rightarrow Q\bar{Q}\gamma + f_k$  phase space is defined by requiring that the energy of the emitted gluon satisfies

$$k^0 > \delta_s \frac{\sqrt{s_{12}}}{2}, \quad (2.84)$$

and both conditions on the angle between the initial and emitted parton are satisfied:

$$\begin{aligned} 1 - \cos \theta_{1k} &> \delta_c, \\ 1 - \cos \theta_{2k} &> \delta_c. \end{aligned} \quad (2.85)$$

The hard/noncollinear cross section is very straightforward to evaluate since there is no singularity in this region. Eq. 2.66 can be integrated numerically in four dimensions by imposing the requirements in Eqs. 2.84 and 2.85. In our calculation the matrix elements for the  $ij \rightarrow Q\bar{Q}\gamma + f_k$  are generated using MadGraph [5] and interfaced with our in-house codes for numerical integration.

## 2.5 Photon isolation and quark-photon final state singularities

The production of photons in hadronic collisions can be described via two main mechanisms:

1. Prompt photon

Prompt-photon production includes both the case in which a photon is directly produced from hard scattering and the case in which a photon is produced from the fragmentation of a QCD parton (schematically shown in Fig 2.17). The probability for a parton  $i$  to fragment into a photon is represented by the corresponding photon fragmentation functions (FFs),  $D_{i \rightarrow \gamma}(z, M_F)$ , where  $z$  is the fraction of the parton momentum that is carried by the photon, and  $M_F$  is the fragmentation scale. Similar to PDFs, FFs have to be extracted from experimental data due to their non-perturbative nature. The cross section for prompt-photon production is given by

$$\sigma^\gamma(M_F) = \sigma_{\text{direct}}^\gamma + \int_0^1 dz \sum_a \sigma_f^a D_{a \rightarrow \gamma}(z, M_F), \quad (2.86)$$

where  $\sigma_{\text{direct}}^\gamma$  represents the cross section for the direct component while  $\sigma_f^a$  denotes the cross section for the production of a parton  $a$ , that further fragments to a photon. Examples of available FFs in the literature are the set by Bourhis, Fontannaz, and Guillet (set I and II) [90] and the one by Gehrmann-de Ridder and Glover [91].

2. Secondary photon

”Secondary” photons are coming from the activities of unstable hadrons, e.g.  $\pi^0 \rightarrow \gamma\gamma$

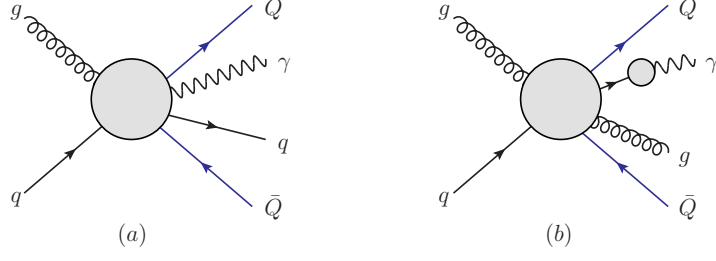


Figure 2.17: Prompt-photon production includes (a) the direct process and (b) the fragmentation process.

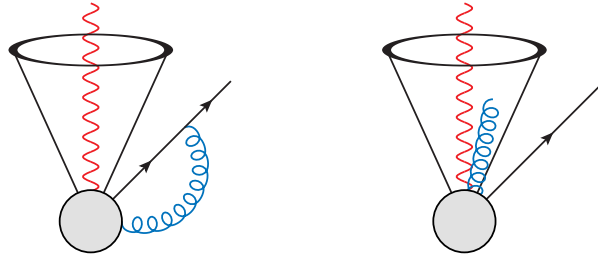


Figure 2.18: Photon isolation in the virtual corrections (left) and the real-emission corrections (right).

decay. The contribution from this mechanism can be suppressed by requiring that the photon is isolated. The photon isolation cut is realized by limiting the amount of hadronic activities inside a cone around the photon with radius  $R_0$ , given by

$$R_0 = \sqrt{\Delta\phi^2 + \Delta\eta^2}. \quad (2.87)$$

$\Delta\eta$  is the pseudorapidity difference between a photon and a jet, where the pseudorapidity is defined by,

$$\eta = \frac{1}{2} \ln \left( \frac{|\vec{p}| + p_z}{|\vec{p}| - p_z} \right), \quad (2.88)$$

while  $\Delta\phi$  is the photon-jet azimuthal angle difference. The hadronic activity is limited by imposing that

$$\sum_{\in R_0} E_T(\text{had}) < \epsilon_h p_T(\gamma) \quad \text{or} \quad \sum_{\in R_0} E_T(\text{had}) < E_T^{\text{max}}. \quad (2.89)$$

Hence the transverse hadronic energy,  $E_T(\text{had})$ , where  $E_T$  is defined by,

$$E_T = \sqrt{p_T^2 + m^2}, \quad (2.90)$$

is limited by some small fraction ( $\epsilon_h$ ) of the photon transverse momentum  $p_T(\gamma)$  or some fix upper value  $E_T^{\max}$ . After isolation cut, the value of  $z$  is typically large, and since the FFs are dominant in the low  $z$  region, the isolation procedure drops the fragmentation contribution substantially.

The singularity structures (both UV and IR) due to the NLO QCD corrections to the  $Q\bar{Q}\gamma$  production and their cancellation have been discussed in Sec. 2.3.1, 2.3.2 and 2.4. However, there is another IR singularity in the  $pp(p\bar{p}) \rightarrow Q\bar{Q}\gamma$  process that we still need to address, when the final-state photon and the massless extra parton become collinear<sup>1</sup>. This singularity arises in the real emission process, e.g. diagram  $i$  in Fig. 2.16. Imposing naive photon isolation criteria or a photon-jet separation cut,  $R(\gamma, j) > R_0$ , will make our NLO calculation IR unsafe. As illustrated in Fig. 2.18, a gluon that is emitted in the real-emission process has to be integrated over the entire phase space in order to cancel the singularity from the virtual counterpart. To take care of the final state quark-photon singularities, we have used Frixione's smooth cone isolation [92]. The isolation prescription is as follows:

1. Reject the event unless the following condition is fulfilled,

$$\sum_i E_T^i \theta(R - R_{i,\gamma}) < E_T^\gamma \left( \frac{1 - \cos R}{1 - \cos R_0} \right) \quad \text{for all } R \leq R_0, \quad (2.91)$$

where the  $i$  summation runs over all final-state partons in the process.  $E_T^{i(\gamma)}$  is the transverse energy of the parton (photon).  $R_0$  is the size of the isolation cone and

$$R_{i,\gamma} = \sqrt{(\Delta\eta_{i,\gamma})^2 + (\Delta\phi_{i,\gamma})^2}.$$

The  $\theta$ -function ensures that the  $i$  summation only receives contributions from partons that lie inside the isolation cone.  $R = R_{i,\gamma}$  if there is only one parton inside the isolation cone, while for the case where more than one photon is present inside the cone,  $R$  is the largest  $R(i, \gamma)$  inside the cone.

2. Apply a jet algorithm of choice to the partons in the event. The jet algorithm will find  $m+n$  candidate jets, where  $m(n)$  is the number of candidate jets that lies outside (inside) the isolation cone.
3. Apply any other experimental cuts to the photon and to the  $m$  candidate jets that lies outside the isolation cone.

An event that passes the prescription above is defined as an isolated-photon plus  $m$ -jets event. The r.h.s of Eq. 2.91 vanishes as  $R \rightarrow 0$ , thus the collinear configurations are suppressed while the soft radiations are allowed to be present arbitrarily close to the photon. Since the collinear configurations are completely removed, there is no fragmentation component in Eq. 2.86.

---

<sup>1</sup>Note that the hard photon cut that is imposed in the calculation eliminates initial state parton-photon collinear singularities and all soft photon singularities.

## 2.6 NLO cross section for $pp(p\bar{p}) \rightarrow Q\bar{Q}\gamma$ production

Now that we have computed the separate pieces of the cross section, i.e. virtual parts ( $q\bar{q}$  and  $gg$ ) and real parts ( $q\bar{q}$ ,  $gg$  and  $qg$ ), we can collect all the results to build the NLO total and differential cross sections. As discussed in Sec. 2.3.1 and 2.3.2, the UV singularities in the virtual diagrams are cancelled by the renormalization procedure, while the final-state and part of the initial-state IR singularities are completely cancelled by the soft and collinear singularities in the real emission corrections. The remaining initial-state collinear singularities in the real corrections are reabsorbed into the renormalized parton distribution functions. In the  $\overline{\text{MS}}$ -subtraction scheme, the renormalized NLO parton distribution function for  $q \rightarrow qg$  splitting in the  $q\bar{q}$ -initiated subprocess is given by,

$$\begin{aligned} \mathcal{F}_q^{p/\bar{p}}(x, \mu_F) &= \mathcal{F}_q^{p/\bar{p}}(x) \left[ 1 - \frac{\alpha_s}{2\pi} \left( \frac{4\pi\mu_R^2}{\mu_F^2} \right)^\epsilon \Gamma(1+\epsilon) \left( \frac{1}{\epsilon} \right) C_F \left( 2\ln\delta_s + \frac{3}{2} \right) \right] \\ &+ \frac{\alpha_s}{2\pi} \left( \frac{4\pi\mu_R^2}{\mu_F^2} \right)^\epsilon \Gamma(1+\epsilon) \int_x^{1-\delta_s} \frac{dz}{z} \left( -\frac{1}{\epsilon} \right) P_{qq}(z) \mathcal{F}_q^{p/\bar{p}}\left(\frac{x}{z}\right), \end{aligned} \quad (2.92)$$

where  $C_F = (N^2 - 1)/2N$ , and  $\mathcal{F}_i^{p/\bar{p}}(x)$  is the bare parton distribution function. For the  $g \rightarrow gg$  splitting that appears in the  $gg$ -initiated subprocess, the  $\overline{\text{MS}}$  renormalized NLO PDF is given by

$$\begin{aligned} \mathcal{F}_g^{p/\bar{p}}(x, \mu_F) &= \mathcal{F}_g^{p/\bar{p}}(x) \left[ 1 - \frac{\alpha_s}{2\pi} \left( \frac{4\pi\mu_R^2}{\mu_F^2} \right)^\epsilon \Gamma(1+\epsilon) \left( \frac{1}{\epsilon} \right) N \left( 2\ln\delta_s + \frac{11}{6} - \frac{n_{\text{lf}}}{3N} \right) \right] \\ &+ \frac{\alpha_s}{2\pi} \left( \frac{4\pi\mu_R^2}{\mu_F^2} \right)^\epsilon \Gamma(1+\epsilon) \int_x^{1-\delta_s} \frac{dz}{z} \left( -\frac{1}{\epsilon} \right) P_{gg}(z) \mathcal{F}_g^{p/\bar{p}}\left(\frac{x}{z}\right), \end{aligned} \quad (2.93)$$

and finally for the  $g \rightarrow q\bar{q}$ ,  $q \rightarrow qg$  or  $\bar{q} \rightarrow \bar{q}g$  splittings in the tree-level  $qg$ -initiated subprocess, the  $\overline{\text{MS}}$  renormalized NLO PDF is given by

$$\mathcal{F}_{k'}^{p/\bar{p}}(x, \mu_F) = \mathcal{F}_{k'}^{p/\bar{p}}(x) + \frac{\alpha_s}{2\pi} \left( \frac{4\pi\mu_R^2}{\mu_F^2} \right)^\epsilon \Gamma(1+\epsilon) \int_x^1 \frac{dz}{z} \left( -\frac{1}{\epsilon} \right) P_{kk'}^A(z) \mathcal{F}_k^{p/\bar{p}}\left(\frac{x}{z}\right), \quad (2.94)$$

where  $(k, k') = (g, q), (g, \bar{q}), (q, g), (\bar{q}, g)$ .  $P_{ij}^A$  is the  $\mathcal{O}(1)$  part of the corresponding Altarelli-Parisi splitting functions. The quark-photon final state singularities that arise when the photon is emitted collinearly from final state massless partons are removed by imposing Frixione's smooth-cone isolation prescription, as discussed in Sec. 2.5. The NLO cross section is now free from both UV and IR singularities.

By convoluting the leading order, virtual and real emission partonic cross sections with the renormalized parton distribution functions, given in Eqs. 2.92 - 2.94. The NLO cross

sections are found to be

$$\begin{aligned}
d\sigma_{q\bar{q}+gg}^{\text{NLO}} &= \sum_{ij=q\bar{q}, \bar{q}q, gg} \int dx_1 dx_2 \mathcal{F}_i^p(x_1, \mu) \mathcal{F}_j^{p/\bar{p}}(x_2, \mu) \\
&\times \left[ d\hat{\sigma}_{ij}^{\text{LO}}(x_1, x_2, \mu) + d\hat{\sigma}_{ij}^{\text{V+CT+S}}(x_1, x_2, \mu) \right] \\
&+ \sum_{ij=q\bar{q}, \bar{q}q, gg} \int dx_1 dx_2 \left\{ \int_{x_1}^{1-\delta_s} \frac{dz}{z} \mathcal{F}_i^p\left(\frac{x_1}{z}, \mu\right) \mathcal{F}_j^{p/\bar{p}}(x_2, \mu) d\hat{\sigma}_{ij}^{\text{LO}}(x_1, x_2, \mu) \right. \\
&\times \frac{\alpha_s}{2\pi} \left[ P_{ii}^4(z) \ln\left(\frac{s_{12}}{\mu^2} \frac{(1-z)^2}{z} \frac{\delta_c}{2}\right) - P'_{ii}(z) \right] + (1 \leftrightarrow 2) \Big\} \\
&+ \sum_{ij=q\bar{q}, \bar{q}q, gg} \int dx_1 dx_2 \mathcal{F}_i^p(x_1, \mu) \mathcal{F}_j^{p/\bar{p}}(x_2, \mu) d\hat{\sigma}_{ij}^{\text{hnc}}(x_1, x_2, \mu), \tag{2.95}
\end{aligned}$$

$$\begin{aligned}
d\sigma_{qg}^{\text{NLO}} &= \frac{\alpha_s}{2\pi} \sum_{i=q, \bar{q}} \int dx_1 dx_2 \left\{ \int_{x_1}^1 \frac{dz}{z} \mathcal{F}_i^p\left(\frac{x_1}{z}, \mu\right) \mathcal{F}_g^{p/\bar{p}}(x_2, \mu) d\hat{\sigma}_{gg}^{\text{LO}}(x_1, x_2, \mu) \right. \\
&\times \left[ P_{ig}^4(z) \ln\left(\frac{s_{12}}{\mu^2} \frac{(1-z)^2}{z} \frac{\delta_c}{2}\right) - P'_{ig}(z) \right] \\
&+ \int_{x_1}^1 \frac{dz}{z} \mathcal{F}_g^p\left(\frac{x_1}{z}, \mu\right) \mathcal{F}_i^{p/\bar{p}}(x_2, \mu) d\hat{\sigma}_{q\bar{q}}^{\text{LO}}(x_1, x_2, \mu) \\
&\times \left[ P_{gi}^4(z) \ln\left(\frac{s_{12}}{\mu^2} \frac{(1-z)^2}{z} \frac{\delta_c}{2}\right) - P'_{gi}(z) \right] + (1 \leftrightarrow 2) \Big\} \\
&+ \sum_{i=q, \bar{q}} \int dx_1 dx_2 \{ \mathcal{F}_i^p(x_1, \mu) \mathcal{F}_g^{p/\bar{p}}(x_2, \mu) d\hat{\sigma}_{qg}^{\text{hnc}}(x_1, x_2, \mu) + (1 \leftrightarrow 2) \}. \tag{2.96}
\end{aligned}$$

where we have set  $\mu_R = \mu_F = \mu$ , and  $P'_{ij}$  is the  $\mathcal{O}(\epsilon)$  part of the Altarelli-Parisi splitting functions. The LO partonic cross section is given in Eq. 2.21,  $d\hat{\sigma}_{ij}^{\text{hnc}}$  is obtained from Eq. 2.66 by imposing the hard/non-collinear cuts, while

$$\begin{aligned}
d\hat{\sigma}_{q\bar{q}}^{\text{V+CT+S}} &= dPS(Q\bar{Q}\gamma) \left\{ 2\mathcal{R}e \overline{\sum} (\mathcal{M}_0^{q\bar{q}})^* \mathcal{M}_{\text{virt}}^{q\bar{q}}|_{\text{finite}} \right. \\
&\quad + 2\mathcal{R}e \overline{\sum} (\mathcal{M}_0^{q\bar{q}})^* \mathcal{M}_{\text{virt}}^{q\bar{q}}|_{UV} \quad (\text{from Eq. 2.30}) \\
&\quad + 2\mathcal{R}e \overline{\sum} (\mathcal{M}_0^{q\bar{q}})^* \mathcal{M}_{\text{virt}}^{q\bar{q}}|_{IR} \quad (\text{from Eq. 2.45}) \Big\} \\
&+ d\hat{\sigma}_{q\bar{q}}^s \quad (\text{from Eq. 2.78}), \tag{2.97}
\end{aligned}$$

$$\begin{aligned}
d\hat{\sigma}_{gg}^{\text{V+CT+S}} &= dPS(Q\bar{Q}\gamma) \left\{ 2\mathcal{R}e \overline{\sum} (\mathcal{M}_0^{gg})^* \mathcal{M}_{\text{virt}}^{gg}|_{\text{finite}} \right. \\
&\quad + 2\mathcal{R}e \overline{\sum} (\mathcal{M}_0^{gg})^* \mathcal{M}_{\text{virt}}^{gg}|_{UV} \quad (\text{from Eq. 2.49}) \\
&\quad + 2\mathcal{R}e \overline{\sum} (\mathcal{M}_0^{gg})^* \mathcal{M}_{\text{virt}}^{gg}|_{IR} \quad (\text{from Eq. 2.57}) \Big\} \\
&+ d\hat{\sigma}_{gg}^s \quad (\text{from Eq. 2.79}). \tag{2.98}
\end{aligned}$$

## 2.7 Treatment of bottom quarks in the final state

The calculation of  $Q\bar{Q}\gamma$  production at hadron colliders at NLO accuracy allows us to study the phenomenology of both  $t\bar{t}\gamma$  and  $b\bar{b}\gamma$  production. Practically, one can simply specify the mass ( $m_Q = m_t$  or  $m_b$ ) as well as the charge of the heavy quark ( $Q_Q = Q_t$  or  $Q_b$ ) to switch from one to the other. The case of a final-state bottom-quark pair, however, requires an extra care due to both theoretical and experimental issues.

The short lifetime of the top quark allows it to decay (dominantly via  $t \rightarrow bW$ ) before it hadronizes. In calculating inclusive observables in  $t\bar{t}\gamma$  production, the top quark can be considered as a stable final state, as done in [45] and [46]. Alternatively, one can also consider more exclusive modes, where the decay of the top-quark pair is also considered. The study of  $t\bar{t}\gamma$  production including NLO QCD corrections both in the production and decay stages is done in [46]. We will consider only the stable top-quark case in this thesis. On the other hand, a bottom quark in the final state will form a jet that can be detected experimentally via  $b$ -tagging. A  $b$  jet differs from a light-quark jet due to the longer lifetime of a  $B$  hadron that allows the corresponding  $b$  jet to form a secondary vertex. For  $b\bar{b}\gamma$  production, we will consider the following cases:

- at least two  $b$  jets observed in the final state ( $pp(p\bar{p}) \rightarrow b\bar{b}\gamma + X$ , "2b-tag"),
- at least one  $b$  jet observed in the final state ( $pp(p\bar{p}) \rightarrow b(\bar{b})\gamma + X$ , "1b-tag").

The calculation of the case where at least one  $b$  jet is identified in the final state can be done using both the Five Flavor Number Scheme (5FNS) and the Four Flavor Number Scheme (4FNS), while the case of at least two  $b$  jets are identified in the final state can only be done in the 4FNS. In the 4FNS calculation, the final-state bottom quarks are treated as massive, and the number of light quarks,  $n_{\text{lf}}$ , is four and only light quarks and gluons are allowed in the initial state. Here, we take our  $Q\bar{Q}\gamma$  calculation and set  $m_Q = m_b$ ,  $Q_Q = Q_b$  and  $n_{\text{lf}} = 4$ , require only  $u$ ,  $d$ ,  $c$ ,  $s$  flavored quarks and gluons to contribute in the initial state, and specify how many  $b$  jets are identified in the final state by imposing a jet algorithm as well as selection cuts on the final state  $b$ -quark transverse momentum and rapidity. When a final state  $b$  quark is not identified, the integration over its phase space will generate logarithms of the form,

$$\ln\left(\frac{Q}{m_b}\right), \quad (2.99)$$

technically  $Q$  is the upper bound on the  $p_T$  of the unobserved  $b$ -quark which is typically of the order of the scale of the hard scattering. Due to the smallness of the bottom-quark mass, these logarithms can become large and spoil the convergence of the perturbative expansion of the cross section.

In the 5FNS calculation, bottom quarks are allowed in the initial state and treated as massless ( $n_{\text{lf}} = 5$ ). The logarithm in Eq. 2.99 can be factored out and resummed by introducing a bottom-quark PDF,

$$f_b^{p/\bar{p}}(x, \mu) = \frac{\alpha_s(\mu)}{2\pi} \ln\left(\frac{Q^2}{m_b^2}\right) \int_x^1 \frac{dy}{y} P_{gq}\left(\frac{x}{y}\right) f_g^{p/\bar{p}}(x, \mu), \quad (2.100)$$

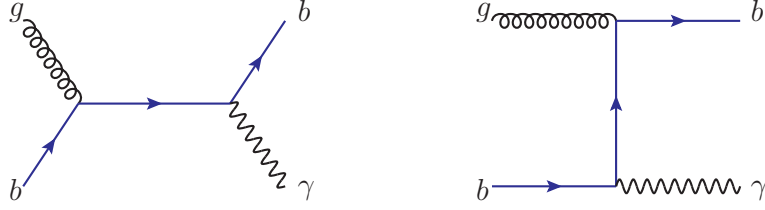


Figure 2.19: Feynman diagrams of  $gb \rightarrow b\gamma$  subprocess in the 5FNS calculation of  $pp(p\bar{p}) \rightarrow b(\bar{b})\gamma + X$  process.

where  $f_g^{p/\bar{p}}(x, \mu)$  is the gluon PDF and  $P_{gq}$  is the bAltarelli-Parisi splitting function for  $g \rightarrow q\bar{q}$  given by Eq. D.22. The resummation of different orders of leading logarithms in Eq. 2.99 is realized via renormalization group arguments in the form of DGLAP equations. By defining the  $b$ -quark PDF, the 5FNS approach restructures the calculation as an expansion in terms of  $\alpha_s$  and different powers of the logarithms in Eq. 2.99. As a result of the 5FNS approach, the process where at least one  $b$  jet is identified in the final state now starts at LO with the  $gb \rightarrow b\gamma$  subprocesses, shown in Fig. 2.19, with  $m_b = 0$ . It is important to notice that the factorization of the logarithms in the 5FNS relies on the approximation that the bottom quark that is not tagged, have small transverse momentum. The resummation of the collinear logarithm in the 5FNS leads to a more stable perturbative behavior, although it only takes into account certain region of kinematics (i.e. low- $p_T^b$  region). As already mentioned in Sec. 1.3, the 5FNS theoretical predictions for  $pp(p\bar{p}) \rightarrow \gamma + b + X$  has been reported in [57] at NLO QCD accuracy, including the fragmentation contributions also at NLO. In this thesis we will calculate  $\gamma + b + X$  process at NLO with the 4FNS approach and compare with the 5FNS results to identify how to obtain more reliable theoretical prediction.

## 2.8 Checks on the calculation

Given the complexity of NLO calculations, comprehensive cross checks need to be performed in order to obtain correct results and efficient numerical codes. We have performed several direct checks on our calculation, ranging from testing all building blocks of the calculation to comparing the final results (i.e. the total cross section and differential distributions) among independent calculation and codes. In addition, we also performed indirect checks, where we used the tools developed for our  $Q\bar{Q}\gamma$  calculation to calculate similar processes (by replacing the photon final state with other bosons, such as a scalar or pseudoscalar Higgs boson), available in the literature, as well as to produce some new results.

### 2.8.1 Direct checks on the calculation

We have performed a number of checks at various stages in our calculation:



- The virtual amplitudes have been cross checked against an independent calculation that uses NLOX, an automated package for one-loop calculations [16]. The checks are done at the level of the matrix-element squared for a few phase-space points, as well as at the level of the total cross section and the corresponding differential distributions.
- The implementation of tensor-integral reductions (à la Passarino-Veltman and à la Diakonidis et al.) is checked against independent routines that are part of the NLOX package.
- The real corrections are cross checked against an independent numerical implementation of the two-cut phase-space-slicing method both for few phase-space points and at the level of the total cross section and the corresponding differential distributions.
- The pole cancellation (both UV and IR) are checked analytically and numerically. We also confirmed that the renormalization scale dependence of the virtual amplitude has the form of Eq. 2.9.
- Our virtual routines have been interfaced with the SHERPA package, allowing us to have an independent cross check of the real corrections. SHERPA employs the dipole subtraction method to isolate the singularities in the real corrections. The total cross section obtained from SHERPA is in a perfect agreement with our result.
- We were able to reproduce the total cross section and differential distribution of the previously published result for  $t\bar{t}\gamma$  production [46].

### 2.8.2 $pp(p\bar{p}) \rightarrow Q\bar{Q} + h/A^0$ production: indirect checks on the calculation

Studying different processes using the NLO framework developed for  $Q\bar{Q}\gamma$  production is an efficient way to reproduce existing results and to provide new ones, and is also important as an indirect check of the building blocks of our codes. In particular, as such testing ground, we have considered the scalar- and pseudoscalar-Higgs production in association with a heavy-quark pair at hadron colliders, i.e.  $pp(p\bar{p}) \rightarrow Q\bar{Q} + h/A^0$ .

The differences between the calculation of  $Q\bar{Q} + \gamma$  and  $Q\bar{Q} + h/A^0$  productions are

1. The coupling between the bosons and the heavy quark.  
The couplings between the heavy quark and the boson ( $h/A^0/\gamma$ ) are diagrammatically shown in Fig. 2.20. Apart from the obvious difference in the overall coupling, the differences illustrated in Fig. 2.20 affect the structure of the  $\gamma$  matrices. The SMEs that are constructed for  $Q\bar{Q} + h/A^0$  production have simpler structure compared to the  $Q\bar{Q} + \gamma$  cases due to the scalar coupling. The  $Q\bar{Q} + A^0$  process, however, has an extra  $\gamma_5$  in the coupling. In addition,  $Q\bar{Q} + h/A^0$  production involves a smaller number of diagrams in the  $q\bar{q}$ -initiated subprocess since the diagrams involving a scalar/pseudoscalar Higgs boson emitted from the initial state (massless) quark do not contribute.
2. The masses of the final state bosons  
The fact that the scalar and pseudoscalar Higgs are massive while the photon is massless affects in particular the kind of scalar integrals that need to be calculated.

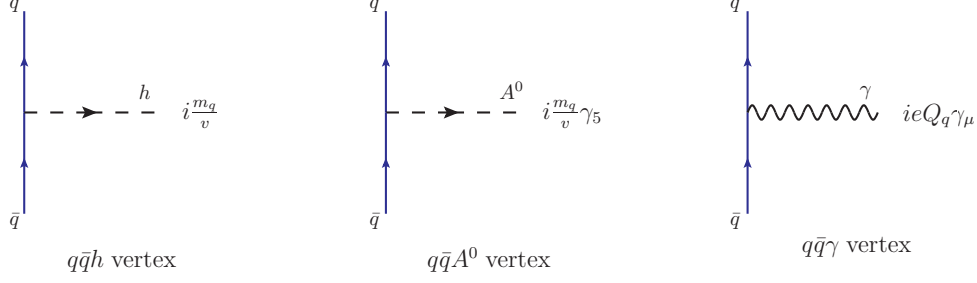


Figure 2.20: The  $q\bar{q}h$ ,  $q\bar{q}A^0$ ,  $q\bar{q}\gamma$  couplings that enter in the calculation of  $pp(p\bar{p}) \rightarrow Q\bar{Q} + h/A^0/\gamma$  process.

3. The contributions from the finite fermion-loop triangle diagrams.

The vanishing fermion-loop triangle diagrams in  $Q\bar{Q}\gamma$  production (shown in Figs. 2.8 and 2.12) are non-vanishing and finite in the  $Q\bar{Q} + h/A^0$  production.

$pp(p\bar{p}) \rightarrow t\bar{t}h$  production has been previously calculated [88, 89, 93, 94, 95, 96]. This has allowed us to comprehensively check our results both diagram-by-diagram and at the level of the total amplitudes at fixed phase space points as well as at the level of the integrated cross section and differential distributions. Similarly, the pseudoscalar case,  $pp(p\bar{p}) \rightarrow t\bar{t}A^0$ , has been computed recently and we have been able to reproduce the total cross section as well as the differential distributions reported in [95]. Our  $t\bar{t}A^0$  calculation also serves as an important cross check for the independent unitarity-based calculation of the virtual corrections performed in [97]. On the other hand we have obtained new results for the pseudoscalar Higgs production in association with bottom-quark pair,  $pp(p\bar{p}) \rightarrow b\bar{b}A^0$ , where we studied both the case in which at least one  $b$  jet and the case in which at least two  $b$  jets are observed in the final states [98].

## CHAPTER 3

# RESULTS FOR $t\bar{t}\gamma$ PRODUCTION AT HADRON COLLIDERS

In this Chapter we present numerical results for the inclusive production of a hard photon in association with a top- and antitop-quark pair at hadron colliders,  $pp(p\bar{p}) \rightarrow t\bar{t}\gamma + X$ , including the full effect of NLO QCD corrections, as described in Chapter 2. The dependence of the total cross section on the cutoff parameters in the PSS2 method,  $\delta_s$  and  $\delta_c$ , is first examined. The impact of renormalization and factorization scale variations on the total cross section of  $t\bar{t}\gamma$  production is studied, followed by the presentation of some interesting differential distributions both at LO and NLO accuracy.

### 3.1 The Setup

The numerical results for  $t\bar{t}\gamma$  production are presented for proton-proton collisions at the LHC with  $\sqrt{s} = 8$  TeV center-of-mass energy and for proton-antiproton collisions at the Tevatron with  $\sqrt{s} = 1.96$  TeV. The following SM parameters will be used in our calculation,

Parameter	Value
$m_t$	173.2 GeV
$\alpha$	1/137

where  $m_t$  and  $\alpha$  are the top-quark mass and the electromagnetic coupling constant respectively. We adopt the Five Flavor Number Scheme (5FNS) for the  $t\bar{t}\gamma$  calculation, in which the bottom quark is treated as massless, and the number of light quarks is set to  $n_{\text{lf}} = 5$ . For the LO results we use the CTEQ6L1 PDF set [99] and the one-loop evolution of the strong coupling  $\alpha_s$ , with  $\alpha_s^{\text{LO}}(M_Z) = 0.13$ , while for the NLO results we use the CT10 PDF set [68] and the two-loop evolution of  $\alpha_s$ , with  $\alpha_s^{\text{NLO}}(M_Z) = 0.118$ . The renormalization and factorization scales are set equal to one another, and the central scale is chosen to be the mass of the top quark,  $\mu_R = \mu_F = \mu_0 = m_t$ . The photon in the event is required to satisfy the Frixione isolation condition with the cone size  $R_0 = 0.4$  and to pass the following selection cuts,

$$p_T(\gamma) > 15 \text{ GeV} \quad \text{and} \quad |y(\gamma)| < 2.37, \quad (3.1)$$

Table 3.1: LO and NLO QCD total cross sections for  $pp(p\bar{p}) \rightarrow t\bar{t}\gamma + X$  at the LHC ( $\sqrt{s} = 8$  TeV) and the Tevatron ( $\sqrt{s} = 1.96$  TeV), together with their  $K$ -factor defined as  $K = \sigma_{\text{NLO}}/\sigma_{\text{LO}}$ . The uncertainties are due to renormalization/factorization scale dependence, obtained by evaluating the cross section at  $\mu = m_t/2$  for the upper value and at  $\mu = 2m_t$  for the lower value. The integration errors are at the ‰ level.

Collider	$\sigma_{\text{LO}}$ [fb]	$\sigma_{\text{NLO}}$ [fb]	$K$ -factor
LHC at 8 TeV	$521.5^{+35\%}_{-24\%}$	$738.4^{+10\%}_{-12\%}$	0.8 - 1.8
Tevatron at 1.96 TeV	$48.1^{+41\%}_{-27\%}$	$45.7^{+1.7\%}_{-10\%}$	0.3 - 1.4

where  $y(\gamma)$  is the rapidity of the photon, and the rapidity is defined by

$$y = \frac{1}{2} \ln \left( \frac{E + p_z}{E - p_z} \right). \quad (3.2)$$

Notice that for a massless particle (e.g. photon) the rapidity and pseudorapidity (see Eq. 2.88) coincide.

### 3.2 Numerical Results

We first check our implementation of the PSS2 method by examining the total cross section as the two cutoff parameters,  $\delta_s$  and  $\delta_c$ , are varied. The total cross section for  $t\bar{t}\gamma$  production at the LHC with  $\delta_c$  fixed at  $2 \times 10^{-6}$  and  $\delta_s$  varied from  $10^{-3}$  to  $10^{-5}$  is shown in Fig. 3.1. In addition, the total cross section for the same process with  $\delta_s$  fixed at  $10^{-4}$  and  $\delta_c$  varied from  $10^{-4}$  to  $10^{-6}$  is shown in Fig. 3.2. Similarly, the  $\delta_s$ - and  $\delta_c$ -dependence plots for  $t\bar{t}\gamma$  production at the Tevatron are shown in Figs. 3.3 and 3.4, respectively. We can see from Figs. 3.1 - 3.4 that the total cross section does not depend on the value of  $\delta_s$  and  $\delta_c$  and any choice in the broad ranges shown in the figures is equivalent. However, while smaller  $\delta_s$  and  $\delta_c$  give a better approximation of the soft and collinear cross sections, they also induce bigger numerical cancellations between the  $2 \rightarrow 4$  ( $\sigma_{\text{hard/non-collinear}}$ ) and the  $2 \rightarrow 3$  contributions ( $\sigma_{\text{soft}} + \sigma_{\text{hard/coll}} + \sigma_{\text{tree}} + \sigma_{\text{virt}}$ ), leading to a bigger integration error on the total cross section. To obtain the total cross section and differential distributions presented in this thesis we have used mid-range values, namely  $\delta_s = 10^{-4}$  and  $\delta_c = 10^{-5}$ .

In Figs. 3.5 and 3.6, we show the dependence of the total cross section on the renormalization and factorization scales at the LHC and at the Tevatron, respectively. The renormalization and factorization scale dependence are commonly used to estimate the ‘theoretical error’ due to the missing higher order terms when we perform the calculation at fixed order

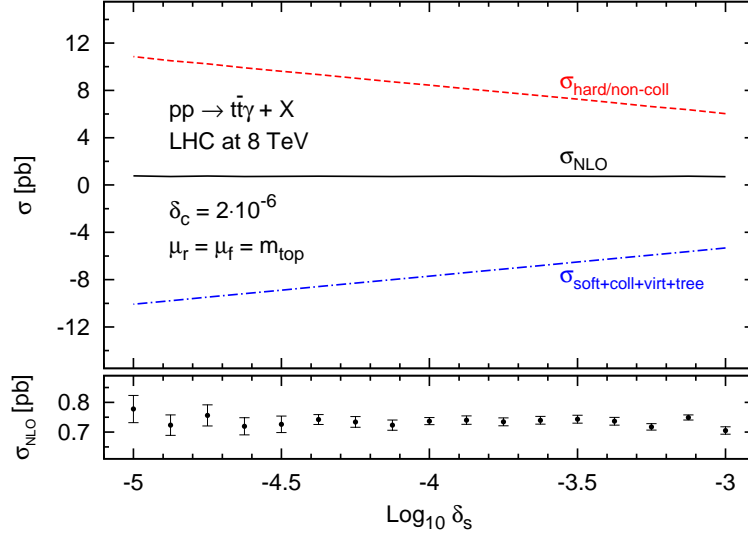


Figure 3.1: The upper plot shows the total cross section for  $pp \rightarrow t\bar{t}\gamma + X$  at the LHC with  $\sqrt{s} = 8$  TeV as a function of the (PSS2) cutoff  $\delta_s$ , while keeping  $\delta_c$  fixed at  $2 \times 10^{-6}$ . The total cross section (black solid line) receives contribution from  $2 \rightarrow 4$  and  $2 \rightarrow 3$  processes as shown in the plot. The  $2 \rightarrow 4$  part (red dashed line) consists of the hard/non-collinear cross section, while the  $2 \rightarrow 3$  part (blue dot-dashed line) consists of the tree level, virtual, soft and hard/collinear cross sections. The lower plot shows the blow up of the total NLO cross section (black solid line) together with the corresponding integration errors.

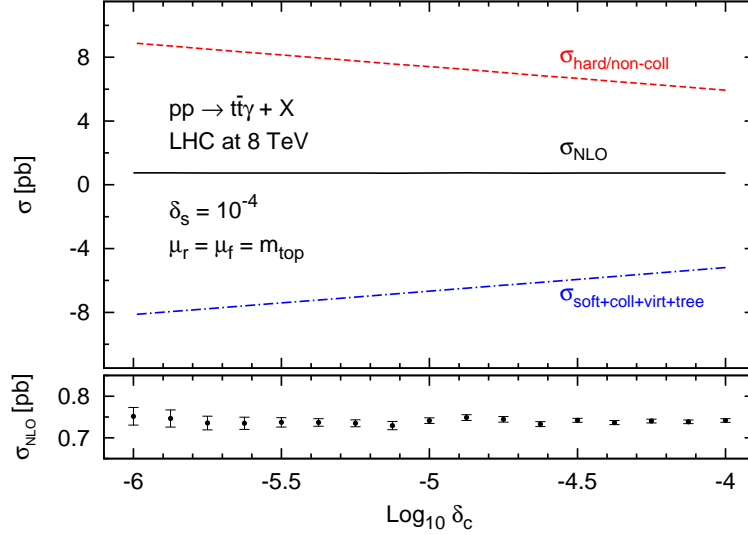


Figure 3.2: NLO total cross section for  $pp \rightarrow t\bar{t}\gamma + X$  at the LHC with  $\sqrt{s} = 8$  TeV as a function of the (PSS2) cutoff  $\delta_c$ , while keeping  $\delta_s$  fixed at  $10^{-4}$ . See caption of Fig. 3.1 for details.

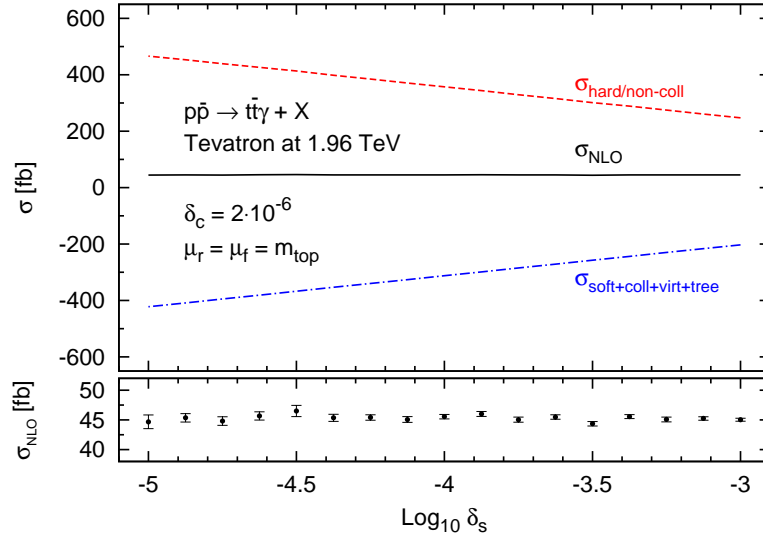


Figure 3.3: NLO total cross section for  $p\bar{p} \rightarrow t\bar{t}\gamma + X$  at the Tevatron with  $\sqrt{s} = 1.96$  TeV as a function of the (PSS2) cutoff  $\delta_s$ , while keeping  $\delta_c$  fixed at  $2 \times 10^{-6}$ . See caption of Fig. 3.1 for details.

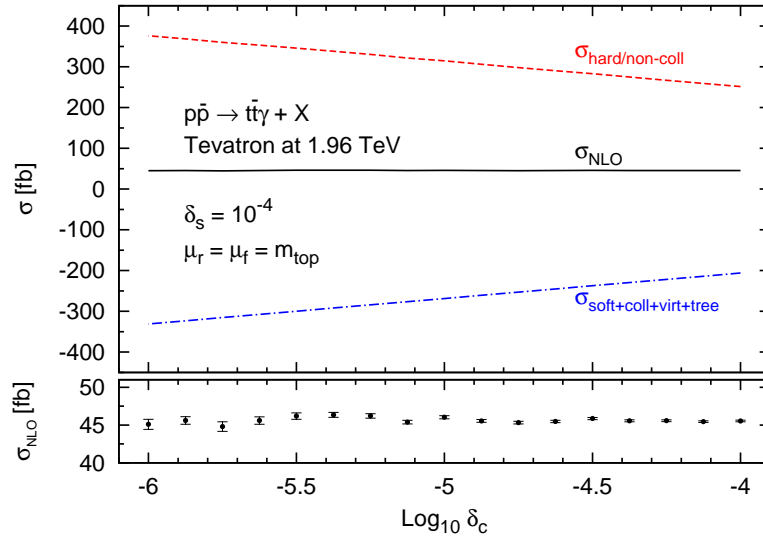


Figure 3.4: NLO total cross section for  $p\bar{p} \rightarrow t\bar{t}\gamma + X$  at the Tevatron with  $\sqrt{s} = 1.96$  TeV as a function of the (PSS2) cutoff  $\delta_c$ , while keeping  $\delta_s$  fixed at  $10^{-4}$ . See caption of Fig. 3.1 for details.

in perturbation theory. We see that both at the LHC and at the Tevatron the scale dependence of the cross section improves when we include the effect of NLO QCD corrections. The improvement of the scale dependence, however, is more pronounced at the Tevatron. This can be understood by looking at the relative size of the different subprocesses that contribute to the total cross section, i.e.  $q\bar{q}$ ,  $gg$ , and  $qg$  as shown in Figs. 3.7 and 3.8. As expected, the  $gg$  initiated subprocess dominates at the LHC, while the  $q\bar{q}$  initiated subprocess dominates at Tevatron and they are both very well-behaved at NLO, since they both start at LO and they only have a very mild scale dependence by the time NLO corrections are added. The residual scale dependence is induced by the third subchannel,  $qg$ , which enters only at NLO as a tree level contribution, and has therefore still a very strong scale dependence. Its effect is more visible at the LHC where it plays a more important role due to the PDF density. The overall impact of the NLO QCD corrections on the cross section is conventionally represented as a  $K$ -factor,  $K = \sigma_{\text{NLO}}/\sigma_{\text{LO}}$ , where, in our case,  $\sigma_{\text{NLO}}$  and  $\sigma_{\text{LO}}$  have been calculated using the set up described in Sec. 3.1. At the LHC, the  $K$ -factor varies from 0.9 to 1.8 in the  $m_t/4 \leq \mu \leq 4m_t$  interval, and above  $\mu = 0.4m_t$  the impact of NLO QCD corrections is quite sizeable. At the Tevatron, the  $K$ -factor varies from 0.3 to 1.4 in the  $m_t/4 \leq \mu \leq 4m_t$  interval, and above  $\mu = 1.5m_t$ , the impact of NLO QCD corrections is somewhat moderate. For completeness, we also present in Table 3.1, the numbers for LO and NLO cross sections for  $t\bar{t}\gamma$  production at both the LHC and the Tevatron. The uncertainty due to scale variation is obtained by evaluating the cross section at  $\mu = m_t/2$  ( $\mu = 2m_t$ ) for the upper (lower) value. We observe that at the LHC the scale uncertainty of the inclusive cross section is reduced from  $\sim 30\%$  to  $\sim 10\%$  when we go from LO to NLO, while at the Tevatron, the reduction of scale uncertainty is even bigger. In this thesis we only report the uncertainty of the theoretical prediction due to the scale variation, while the other sources of theoretical error, i.e. PDF,  $\alpha_s$ , and several input parameters such as  $m_t$  and  $\alpha$  are not included.

Finally, we present some interesting kinematic distributions for  $t\bar{t}\gamma$  production both at LO and NLO. For a particular kinematic distribution, the  $K$ -factor is defined by,

$$K(\mathcal{O}) = \frac{d\sigma_{\text{NLO}}}{d\mathcal{O}} \bigg/ \frac{d\sigma_{\text{LO}}}{d\mathcal{O}}, \quad (3.3)$$

where  $\mathcal{O}$  is a kinematic variable of interest, and the  $K$ -factor is calculated on a bin-by-bin basis. In Fig. 3.9, we show the photon and top-quark transverse-momentum distributions at the LHC, together with their  $K$ -factor. We see that the differential distributions also show an improved scale dependence from LO to NLO. The  $K$ -factor for the photon transverse-momentum distribution is quite stable at  $K \sim 1.4$  in the entire  $p_T(\gamma)$  region, while for the top-quark transverse-momentum distribution the  $K$ -factor decreases as  $p_T(t)$  increases. This demonstrates that simple rescaling of the LO differential distributions using a global  $K$ -factor would not guarantee the correctness of the shape and normalization of the NLO differential distributions. In Fig. 3.10, we show the photon and top-quark rapidity distributions at the LHC, together with their  $K$ -factor. Similar to the top-quark  $p_T$  distribution, the  $K$ -factors for the rapidity distribution, both for photon and top quark, are not uniform. The  $K$ -factor for the top-quark rapidity distribution is  $\sim 1.3$  in the central region ( $y(t) = 0$ ) and  $\sim 2.2$  at  $|y(t)| = 3$ . For the photon rapidity distribution, the  $K$ -factor is  $\sim 1.3$  in the

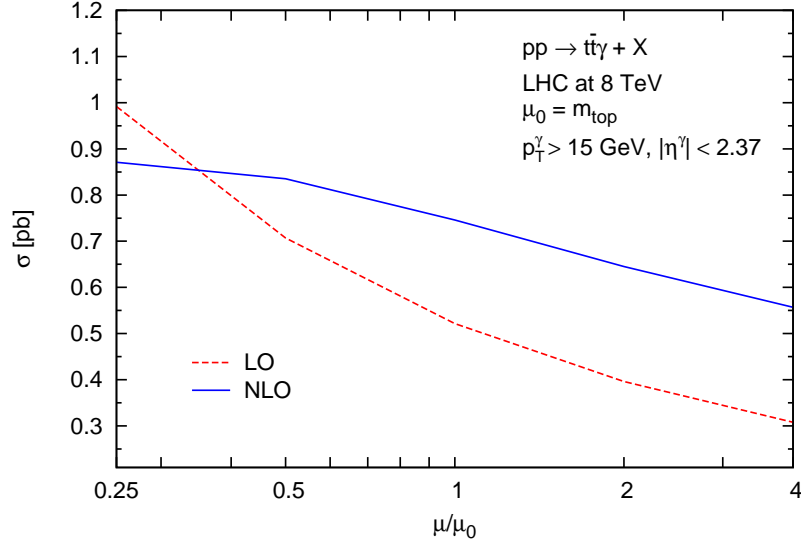


Figure 3.5: Dependence of the  $pp \rightarrow t\bar{t}\gamma + X$  LO (red) and NLO (blue) cross section on the renormalization/factorization scale at the LHC with  $\sqrt{s} = 8$  TeV and  $\mu_R = \mu_F$ . The central scale is chosen to be  $\mu_0 = m_t$ .

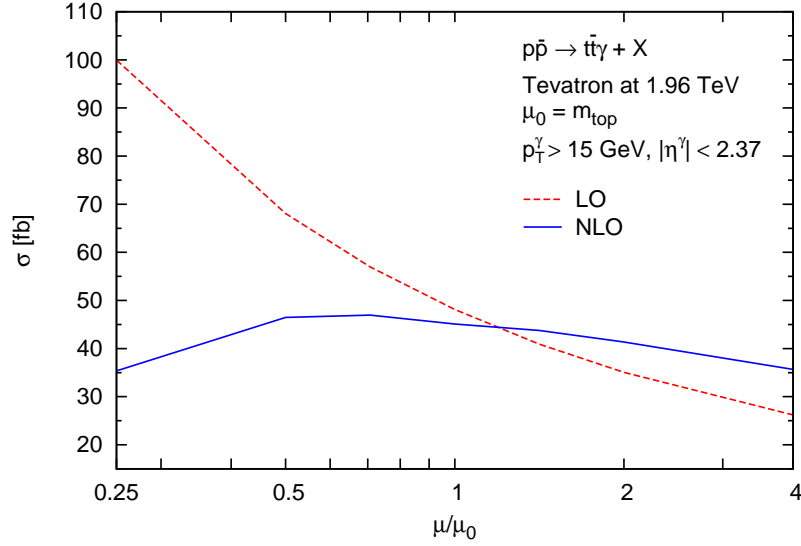


Figure 3.6: Dependence of the  $pp \rightarrow t\bar{t}\gamma + X$  LO (red) and NLO (blue) cross section to the renormalization/factorization scale at the Tevatron with  $\sqrt{s} = 1.96$  TeV and  $\mu_R = \mu_F$ . The central scale is chosen to be  $\mu_0 = m_t$ .



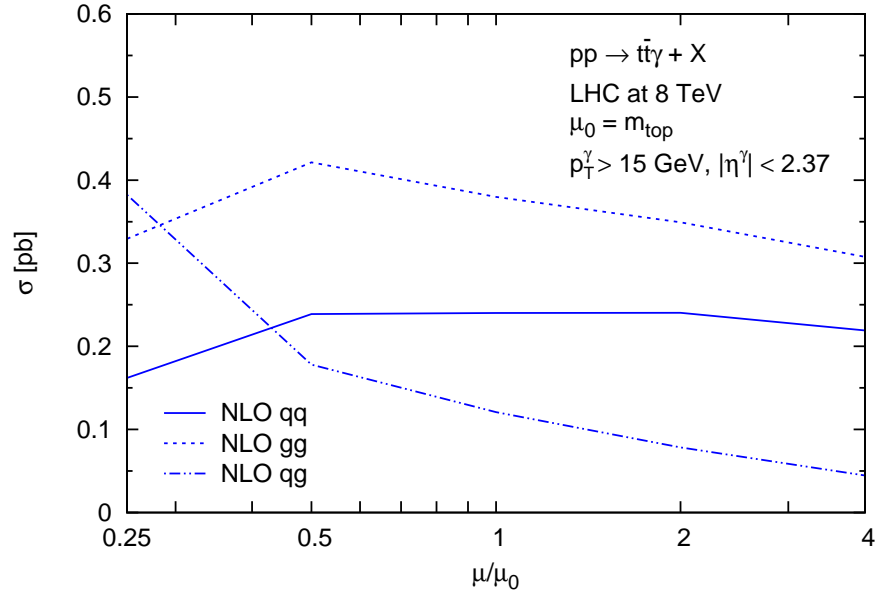


Figure 3.7: Scale dependence of the separate contributions to the NLO total  $pp \rightarrow t\bar{t}\gamma + X$  cross section at the LHC with  $\sqrt{s} = 8$  TeV.

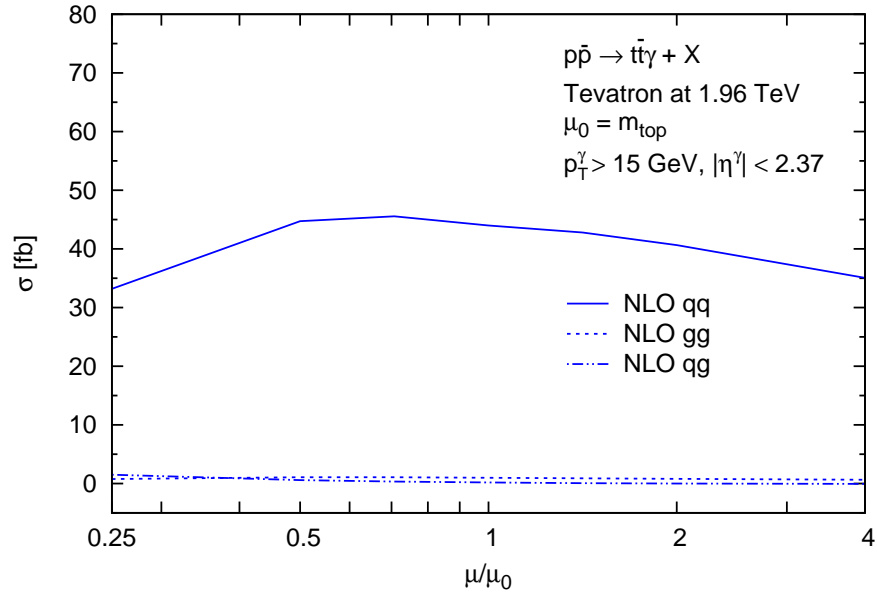


Figure 3.8: Scale dependence of the separate contributions to the NLO total  $pp \rightarrow t\bar{t}\gamma + X$  cross section at the Tevatron with  $\sqrt{s} = 1.96$  TeV.

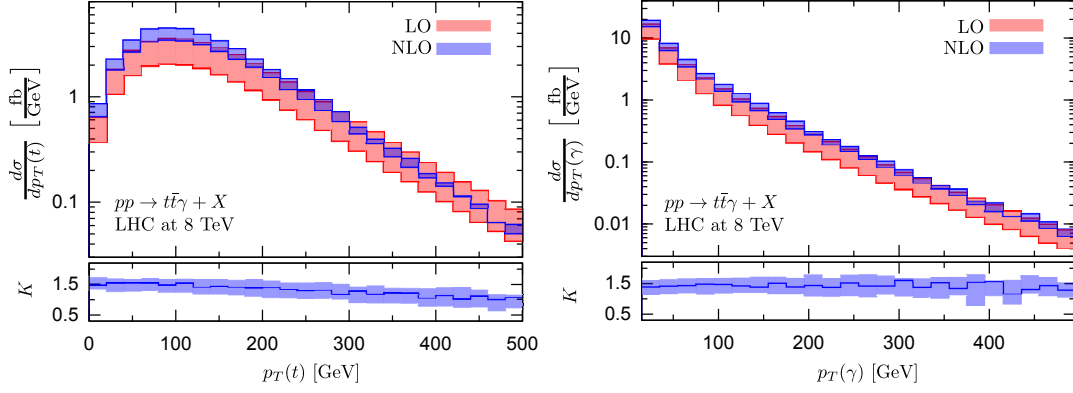


Figure 3.9: Transverse-momentum distributions of the photon (left) and top quark (right) for the  $pp \rightarrow t\bar{t}\gamma + X$  process at the LHC with  $\sqrt{s} = 8$  TeV. The bands correspond to the variation of the renormalization and factorization scales in the interval  $m_t/2 < \mu < 2m_t$ . The lower plot shows the bin-by-bin  $K$ -factor for the distribution, defined in Eq. 3.3.

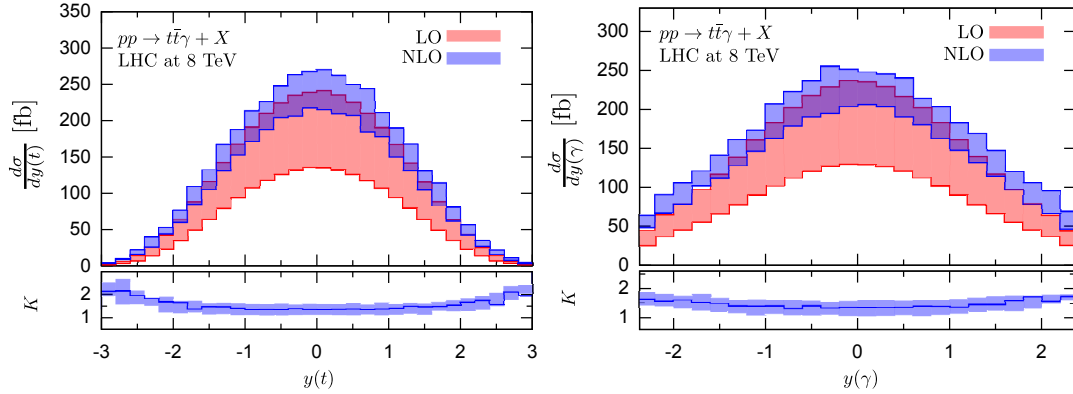


Figure 3.10: Rapidity distributions of the photon (left) and top quark (right) for the  $pp \rightarrow t\bar{t}\gamma + X$  process at the LHC with  $\sqrt{s} = 8$  TeV. The bands correspond to the variation of the renormalization and factorization scales in the interval  $m_t/2 < \mu < 2m_t$ . The lower plot shows the bin-by-bin  $K$ -factor for the distribution, defined in Eq. 3.3.

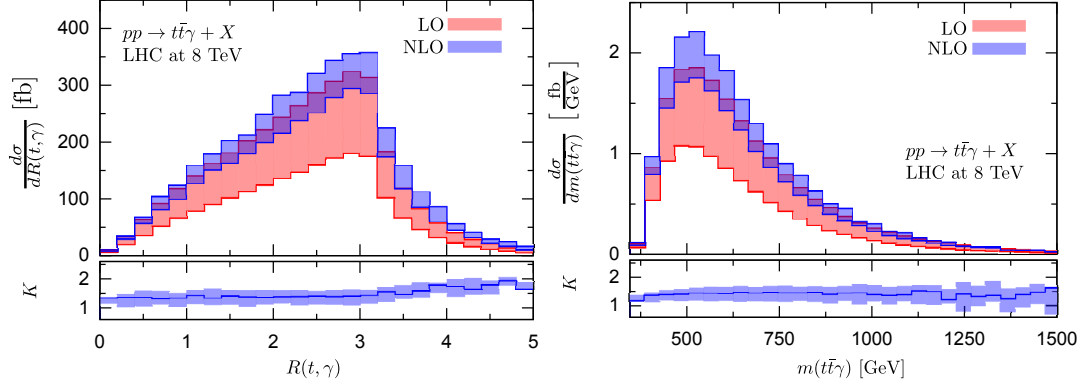


Figure 3.11: Distributions of the top-quark to photon separation (left) and of the invariant mass of the  $t\bar{t}\gamma$  system for the  $pp \rightarrow t\bar{t}\gamma + X$  process at the LHC with  $\sqrt{s} = 8$  TeV. The bands correspond to the variation of the renormalization and factorization scales in the interval  $m_t/2 < \mu < 2m_t$ . The lower plot shows the bin-by-bin  $K$ -factor for the distribution, defined in Eq. 3.3.

central region ( $y(\gamma) = 0$ ) and  $\sim 1.6$  at  $|y(\gamma)| = 3$ . We also show distributions for the separation of top-quark and photon,  $R(t, \gamma)$ , and for the invariant mass of the  $t\bar{t}\gamma$  system  $m(t\bar{t}\gamma)$  at the LHC in Fig. 3.11. The  $K$ -factor for the  $R(t, \gamma)$  distribution is constant up to  $R(t, \gamma) = 3.2$ , while beyond that it starts to increase. For the  $m(t\bar{t}\gamma)$  distribution, the plot starts at  $m(t\bar{t}\gamma) = 2m_t$ , which is the threshold for the  $t\bar{t}\gamma$  final state, and, although the  $K$ -factor seems to be smaller in the low  $m(t\bar{t}\gamma)$  region, it is quite stable in the intermediate to high  $m(t\bar{t}\gamma)$  region.

Switching the discussion to the kinematic distributions at the Tevatron, in Figs. 3.12 - 3.14 we show the transverse-momentum and rapidity distributions both for the top quark and the photon, as well as the  $R(t, \gamma)$  and  $m(t\bar{t}\gamma)$  distributions. Similar to what we have observed in the total cross section, the improvement of the scale uncertainty in the differential distributions including the effect of NLO QCD corrections is more pronounced at the Tevatron than at the LHC. The enhancement due to NLO QCD corrections, however, is much smaller at Tevatron in comparison with the LHC. While the NLO distributions are always above the LO distributions at the LHC, they are always inside or below the LO distributions band at the Tevatron. The  $K$ -factor for the  $p_T(t)$ ,  $p_T(\gamma)$  and  $m(t\bar{t}\gamma)$  distributions decreases as  $p_T(t)$ ,  $p_T(\gamma)$  or  $m(t\bar{t}\gamma)$  increases respectively. The  $K$ -factor starts at  $\sim 1$  and drops to  $\sim 0.5 - 0.75$  at the tail of the  $p_T(t)$ ,  $p_T(\gamma)$ , or  $m(t\bar{t}\gamma)$  distributions. The  $K$ -factor of the  $y(\gamma)$  and  $R(t, \gamma)$  distributions on the other hand, seems to be stable throughout all the  $y(\gamma)$  and  $R(t, \gamma)$  regions. One of the most interesting distribution in the Tevatron case, perhaps, is the rapidity distribution of the top quark, shown in Fig. 3.13 (left), in which the charge or forward-backward asymmetry of the top quark is observed. We can compute

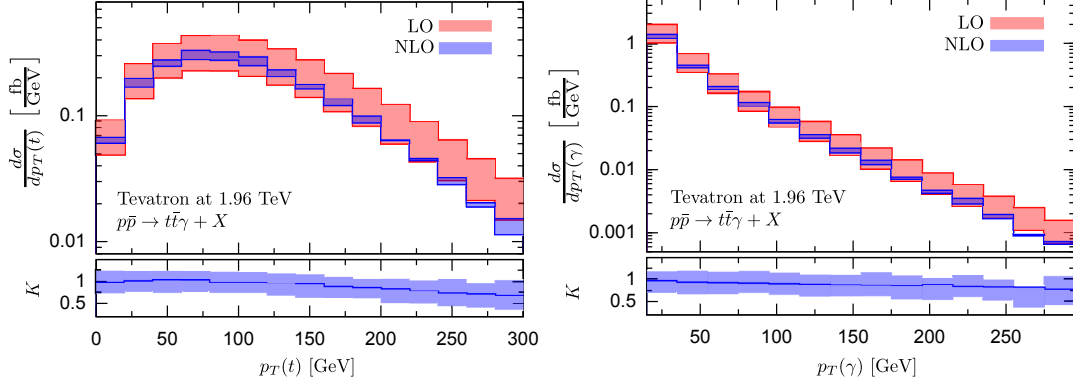


Figure 3.12: Transverse-momentum distributions of final state photon (left) and top quark (right) for  $p\bar{p} \rightarrow t\bar{t}\gamma + X$  process at the Tevatron with  $\sqrt{s} = 1.96$  TeV. The bands correspond to the variation of the renormalization and factorization scales in the interval  $m_t/2 < \mu < 2m_t$ . The lower plot shows the bin-by-bin  $K$ -factor for the distribution, defined in Eq. 3.3.

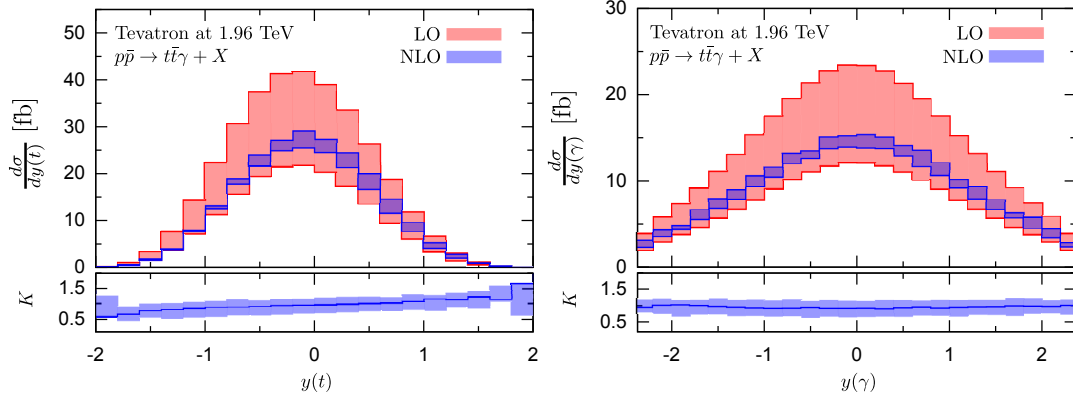


Figure 3.13: Rapidity distributions of final state photon (left) and top quark (right) for  $p\bar{p} \rightarrow t\bar{t}\gamma + X$  process at the Tevatron with  $\sqrt{s} = 1.96$  TeV. The bands correspond to the variation of the renormalization and factorization scales in the interval  $m_t/2 < \mu < 2m_t$ . The lower plot shows the bin-by-bin  $K$ -factor for the distribution, defined in Eq. 3.3.

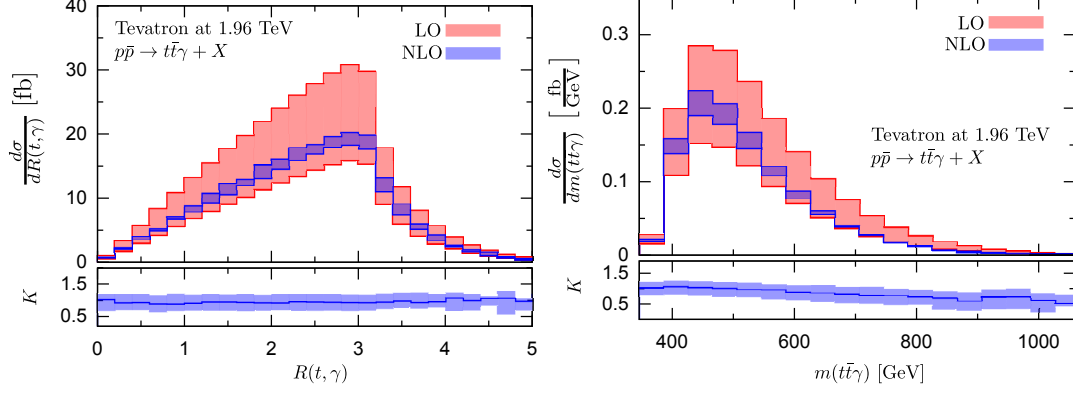


Figure 3.14: The distributions of top quark-photon separation (left) and invariant mass of the  $t\bar{t}\gamma$  system for  $p\bar{p} \rightarrow t\bar{t}\gamma + X$  process at the Tevatron with  $\sqrt{s} = 1.96$  TeV. The bands correspond to the variation of the renormalization and factorization scales in the interval  $m_t/2 < \mu < 2m_t$ . The lower plot shows the bin-by-bin  $K$ -factor for the distribution, defined in Eq. 3.3.

the forward-backward asymmetry by defining [51, 46],

$$A_t = \frac{\sigma[y(t) > 0] - \sigma[y(t) < 0]}{\sigma[y(t) > 0] + \sigma[y(t) < 0]}. \quad (3.4)$$

We found that, the top-quark forward-backward asymmetry calculated at LO and including the NLO QCD corrections are

$$A_t^{\text{LO}} = -17.45^{+0.0}_{-0.0} \%, \quad A_t^{\text{NLO}} = -12.42^{+3.2}_{-0.8} \%, \quad (3.5)$$

where the upper (lower) values are obtained by evaluating  $A_t$  at  $\mu = m_t/2$  ( $\mu = 2m_t$ ). The  $K$ -factor for the top-quark rapidity distribution is also asymmetric, it increases in the forward region ( $y(t) > 0$ ) but it decreases in the backward region ( $y(t) < 0$ ).

# CHAPTER 4

## RESULTS FOR $b\bar{b}\gamma$ PRODUCTION AT HADRON COLLIDERS

In this Chapter we present the numerical results for the inclusive hard-photon production in association with a bottom- and antibottom-quark pair at hadron colliders,  $pp(p\bar{p}) \rightarrow b\bar{b}\gamma + X$  including the full effect of NLO QCD corrections as described in Chapter 2. As discussed in Sec. 2.7, in the case of  $b\bar{b}\gamma$  production we can study two different final states:  $\gamma + 2b + X$ , where at least two  $b$  jets identified in the final state ( $2b$ -tag), or  $\gamma + b + X$ , where at least one  $b$  jet identified in the final state ( $1b$ -tag). We will show the results for the total cross section and differential distributions both at LO and NLO. For the  $1b$ -tag case, we will compare the results obtained from our 4FNS calculation with the results obtained from the 5FNS calculation at NLO in QCD. Finally, we will provide a qualitative comparison for  $\gamma + b + X$  between the theoretical prediction (taking into account NLO QCD corrections on  $pp(p\bar{p}) \rightarrow b\bar{b}\gamma$ ) and the measurement by the CDF collaboration.

### 4.1 The Setup

The numerical results for  $b\bar{b}\gamma$  production will be presented for proton-proton collisions at the LHC with  $\sqrt{s} = 8$  TeV center-of-mass energy and proton-antiproton collisions at the Tevatron with  $\sqrt{s} = 1.96$  TeV. The following SM parameters will be used in the numerical evaluation,

Parameter	Value
$m_b$	4.62 GeV
$m_t$	173.2 GeV
$\alpha$	1/137

where  $m_t$ ,  $m_b$ , and  $\alpha$  are the top-quark mass, bottom-quark mass, and electromagnetic coupling constant respectively. The bottom quark is treated as massive, with the number of light quark entering any fermion loop set to  $n_{\text{lf}} = 4$ . This means that any fermion loop that enters in the virtual correction consists of four light-quark, one bottom-quark and one top-quark loop. The LO results use the CTEQ6L1 PDF set [99] and the one-loop evolution of the strong coupling,  $\alpha_s$ , with  $\alpha_s^{\text{LO}}(M_Z) = 0.13$ , while the NLO results use the CT10 PDF set [68] and the two-loop evolution of  $\alpha_s$ , with  $\alpha_s^{\text{NLO}}(M_Z) = 0.118$ . The renormalization

Table 4.1: LO and NLO QCD Total cross sections for  $pp(p\bar{p}) \rightarrow b\bar{b}\gamma + X$  production with at least two  $b$  jets tagged in the final state at the LHC ( $\sqrt{s} = 8$  TeV) and the Tevatron ( $\sqrt{s} = 1.96$  TeV), together with their  $K$ -factor. The uncertainties are due to the dependence on the renormalization/factorization scale, obtained by evaluating the cross section at  $\mu = p_T(\gamma)/4$  for the upper value and at  $\mu = 4p_T(\gamma)$  for the lower value. The integration errors are well below 1%

Collider	$\sigma_{\text{LO}}$ [pb]	$\sigma_{\text{NLO}}$ [pb]	$K$ -factor
LHC at 8 TeV	$29.5^{+38\%}_{-73\%}$	$45.3^{+27\%}_{-60\%}$	1.4 - 1.8
Tevatron at 1.96 TeV	$2.18^{+43\%}_{-104\%}$	$3.24^{+30\%}_{-42\%}$	1.0 - 1.8

and factorization scales are set equal to one another, and the central scale is chosen to be the dynamical scale given by,

$$\mu_R = \mu_F = \mu_0 = p_T(\gamma), \quad (4.1)$$

for both the  $2b$ - and  $1b$ -tag case. We have explored other possibilities and will comment on our choice in Sec. 4.2. The selection cuts for the photon are:  $p_T(\gamma) > 30$  GeV and  $|\eta(\gamma)| < 1$  for the Tevatron and  $p_T(\gamma) > 25$  GeV and  $|\eta(\gamma)| < 1.37$  for the LHC, with the Frixione isolation cone,  $R_0 = 0.4$ . The jets (originated from the bottom and the light quarks) are clustered with the anti- $k_T$  jet algorithm, with pseudo cone size  $R = 0.4$ , and are required to pass the following selection cuts:

$$\begin{aligned} \text{LHC:} \quad & p_T(b, j) > 25 \text{ GeV}, |\eta(b, j)| < 2.1 \\ \text{Tevatron:} \quad & p_T(b, j) > 20 \text{ GeV}, |\eta(b, j)| < 1.5. \end{aligned}$$

Since we consider inclusive observables, we include events with both 0 and 1 identified light-parton jet in our calculation. In contrast to the top quarks in  $t\bar{t}\gamma$  production, here the bottom quarks have to be included in the hadronic energy contribution in the Frixione isolation, following the prescription described in Sec. 2.5.

## 4.2 $pp(p\bar{p}) \rightarrow b\bar{b}\gamma + X$ : at least two $b$ jets identified in the final state

In this section we present results for  $b\bar{b}\gamma$  production where at least two  $b$  jets are tagged in the final state. We first assess the impact of NLO QCD corrections on the perturbative stability of the total cross section, by showing in Fig. 4.1 the dependence on the renormalization/factorization scale at the LHC and at the Tevatron. The residual scale dependence still turns out to be strong at the LHC when NLO QCD corrections are included, while at the Tevatron a very little improvement is observed. At the LHC the  $K$ -factor for the total

cross section varies from 1.4 to 1.8 in the  $\mu_0/4 \leq \mu \leq 4\mu_0$  interval, while at the Tevatron the  $K$ -factor varies from 1 to 1.8 in the  $\mu_0/4 \leq \mu \leq 4\mu_0$  interval. To study where the strong scale dependence comes from, we take a look into the scale dependence of the different subprocesses that contribute to the total NLO cross section, as shown in Fig 4.2. At the LHC, both at LO and NLO, the  $gg$  channel dominates over the  $q\bar{q}$  channel, as opposed to the Tevatron case, where the  $q\bar{q}$  channel dominates over the  $gg$  channel. It is interesting to see that both at the LHC and at the Tevatron, at NLO, the scale dependence of the  $q\bar{q}$  and  $gg$  channels are improved, as we can see from the plateau in the scale-dependence plot while the residual scale dependence is due to the  $qg$  channel that comes in at tree level in the NLO corrections. We also try four different central-scale choices to see the stability of each subprocess with respect to different dynamical scales. From the four plots that are shown in Fig. 4.3, where we take the LHC at 8 TeV as an example, it is evident that the NLO cross sections are shifted when a different central scale is chosen. By investigating the separate contribution from each subprocess, we see that the shifting of the total NLO cross section is driven by the  $qg$  channel and is therefore part of the theoretical uncertainty introduced by this channel. On the other hand, both the  $q\bar{q}$  and  $gg$  channels are relatively insensitive to the different choice of central scale. In presenting our results for  $b\bar{b}\gamma$  production we have chosen the scale to be fixed by the photon transverse momentum. In Table. 4.1, we also present the numbers for LO and NLO cross sections for both the LHC at 8 TeV and the Tevatron at 1.96 TeV. The uncertainty due to scale variations is obtained by evaluating the cross section at  $\mu = p_T(\gamma)/4$  ( $\mu = 4p_T(\gamma)$ ) for the upper (lower) value.

We now turn the discussion to the differential distributions for  $b\bar{b}\gamma$  production where at least two  $b$  jets identified in the final state. In Figs. 4.4 and 4.5 we show the photon and the leading  $b$ -jet (tagged  $b$  jet with highest  $p_T$ , further denoted by  $b_1$ ) transverse-momentum distributions as well as the photon pseudorapidity and photon to leading  $b$ -jet separation ( $R(\gamma, b_1)$ ) distributions at the LHC. The impact of the NLO QCD corrections on the differential distributions is sizeable. At the LHC, the  $K$ -factor for the photon- $p_T$  distribution is  $\sim 1.7$  in the low- $p_T$  region, and grows as  $p_T$  increases. For the leading  $b$ -jet distribution, the  $K$ -factor is  $\sim 2.3$  at low  $p_T(b_1)$ , drops a little bit in the intermediate  $p_T(b_1)$  region, and slightly increases in the higher  $p_T(b_1)$  region. For the photon pseudorapidity distribution, the  $K$ -factor is quite large and the shape of the distribution also slightly changes at NLO, becoming flatter due to less photon events that populate the perpendicular direction with respect to the beam axis. In the  $R(\gamma, b_1)$  distribution we observe an accidental pinching of the scale variation band at  $R(\gamma, b_1) \sim 2.4$ . The  $K$ -factor is also not well-defined for  $R(\gamma, b_1) < 1.7$ , where at LO there is no event. In Figs. 4.6 and 4.7 we show the photon and leading  $b$ -jet transverse-momentum distributions as well as the photon pseudorapidity and  $R(\gamma, b_1)$  distributions at the Tevatron. The impact of the NLO QCD corrections on the differential distributions are sizeable, similar to the LHC case. At the Tevatron, the  $K$ -factor for both the  $p_T(\gamma)$  and  $p_T(b_1)$  distributions decreases as  $p_T$  grows. The photon pseudorapidity and  $R(\gamma, b_1)$  distributions are similar in comparison to the LHC case, both in terms of shape and  $K$ -factor.

The strong residual scale dependence at NLO is also manifest in the differential distributions at the LHC where in Fig. 4.4, both for  $p_T(\gamma)$  and  $p_T(b_1)$ , the NLO bands are



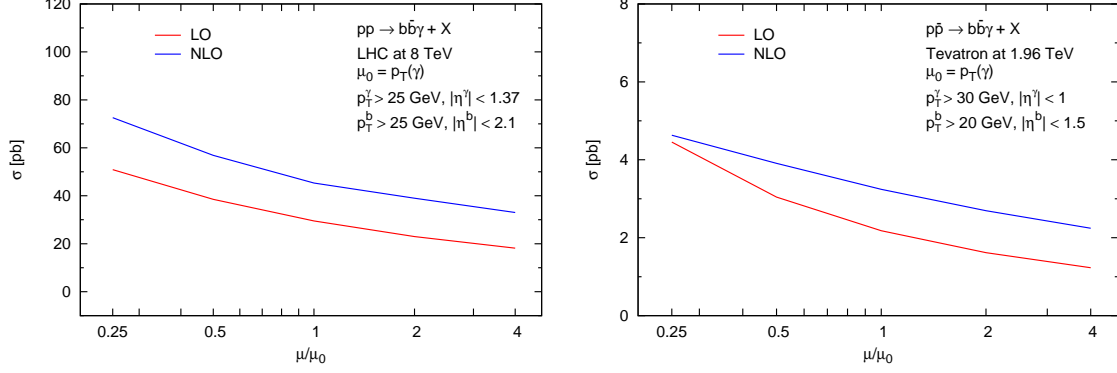


Figure 4.1: Dependence of the  $pp \rightarrow b\bar{b}\gamma + X$  (at least two  $b$  jets identified in the final state) LO (red) and NLO (blue) cross section on the renormalization/factorization scale at the LHC with  $\sqrt{s} = 8$  TeV (left) and at the Tevatron with  $\sqrt{s} = 1.96$  TeV (right).

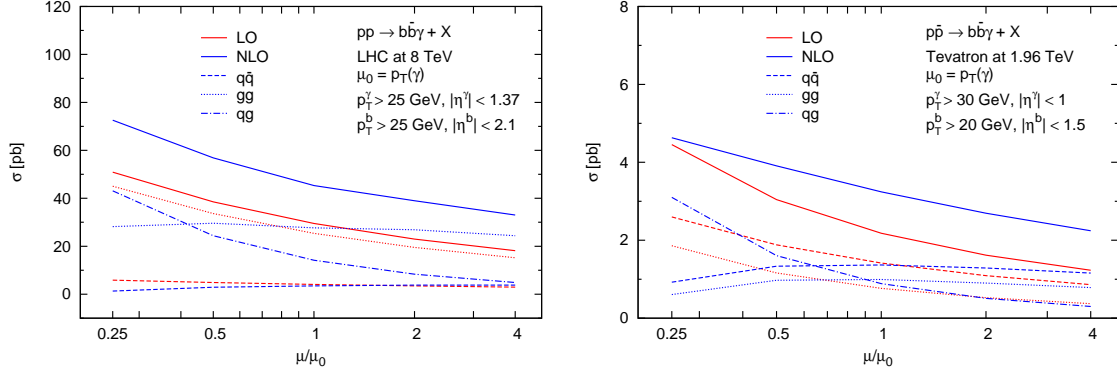


Figure 4.2: Dependence of the  $pp \rightarrow b\bar{b}\gamma + X$  (at least two  $b$  jets identified in the final state) LO (red) and NLO (blue) cross section, with the  $q\bar{q}$  (dashed),  $gg$  (dotted) and  $qg$  (dash-dotted) channels individually shown, on the renormalization/factorization scale at the LHC with  $\sqrt{s} = 8$  TeV (left) and at the Tevatron with  $\sqrt{s} = 1.96$  TeV (right).

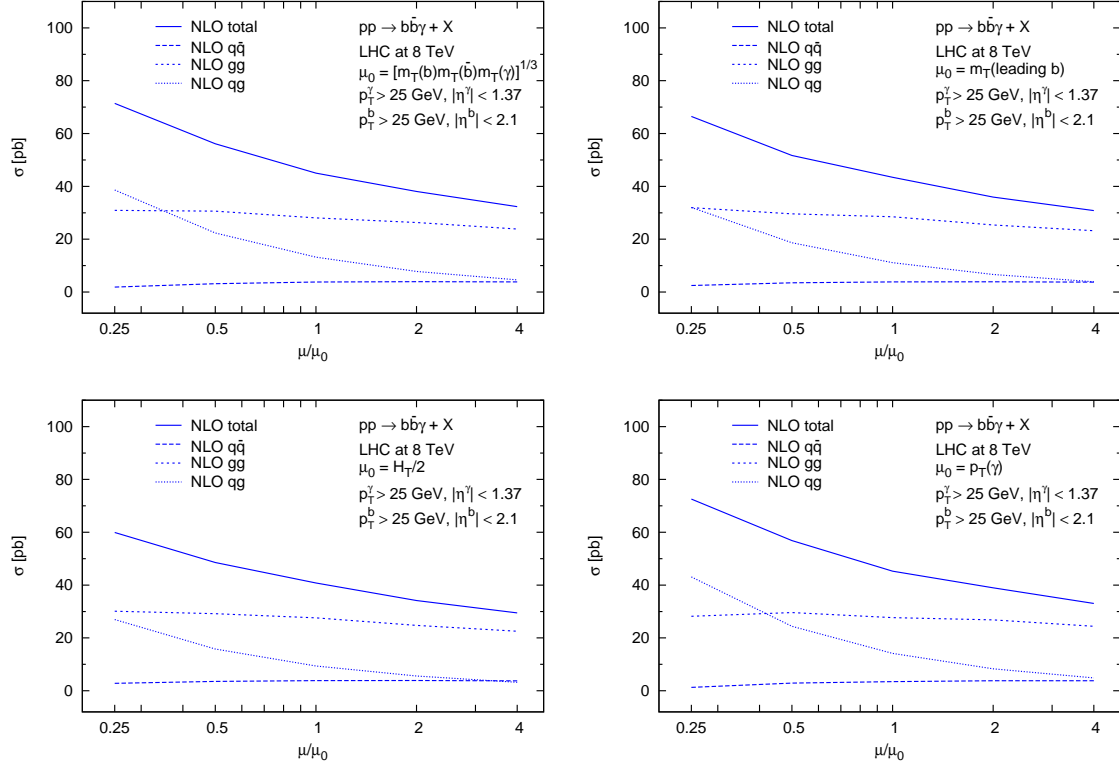


Figure 4.3: Scale dependence of the  $q\bar{q}$ - (dashed),  $gg$ - (dotted),  $qg$ - (dash-dotted) subprocess and the NLO total cross section (solid) for the  $pp \rightarrow b\bar{b}\gamma + X$  (at least two  $b$  jets identified in the final state) for four different choices of the central scale:  $\mu_0 = (m_T(b)m_T(\bar{b})m_T(\gamma))^{1/3}$  (top-left),  $\mu_0 = m_T(\text{leading } b)$  (top-right),  $\mu_0 = H_T/2 = \sum_{i=b,\bar{b},\gamma} E_T^i/2$  (bottom-left),  $\mu_0 = p_T(\gamma)$  (bottom-right).

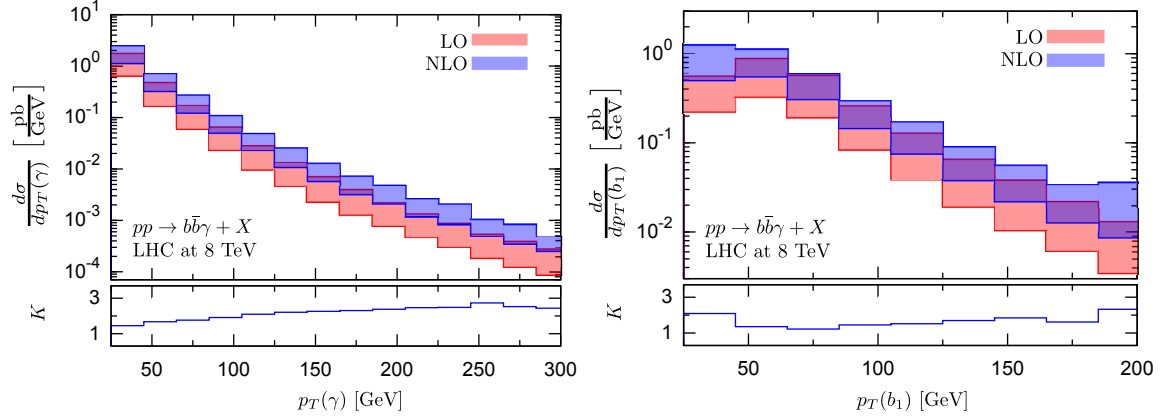


Figure 4.4: The upper plot shows the transverse-momentum distributions of the photon (left) and the leading  $b$  jet (right) for  $pp \rightarrow b\bar{b}\gamma + X$  (at least 2  $b$  jets identified in the final state) at the LHC with  $\sqrt{s} = 8$  TeV. The bands correspond to the variation of the renormalization and factorization scales in the interval  $\mu_0/4 < \mu < 4\mu_0$ . The lower plot shows the bin-by-bin  $K$ -factor for the corresponding distribution.

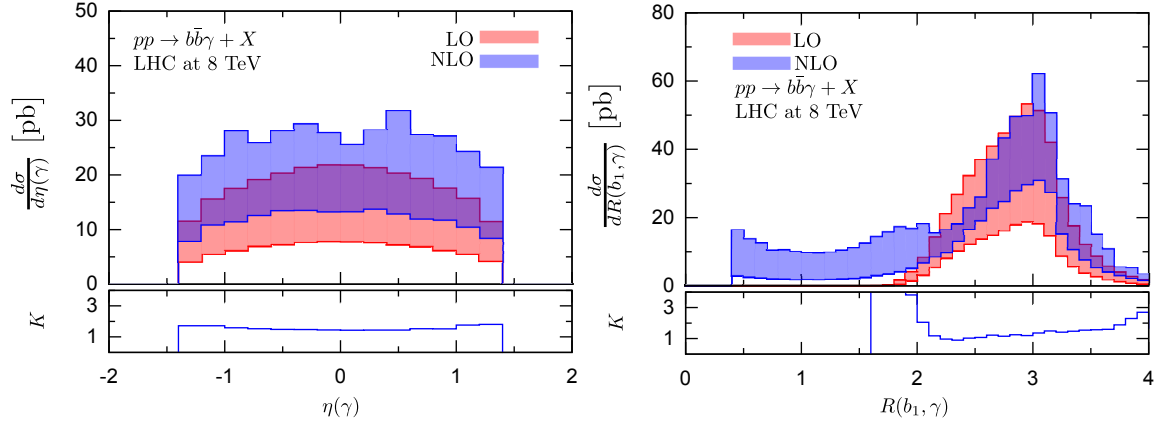


Figure 4.5: The upper plot shows the pseudorapidity distribution of the photon (left) and the separation between the leading  $b$  jet and the photon (right) for  $pp \rightarrow b\bar{b}\gamma + X$  (at least two  $b$  jets identified in the final state) at the LHC with  $\sqrt{s} = 8$  TeV. The bands correspond to the variation of the renormalization and factorization scales in the interval  $\mu_0/4 < \mu < 4\mu_0$ . The lower plot shows the bin-by-bin  $K$ -factor for the corresponding distribution.

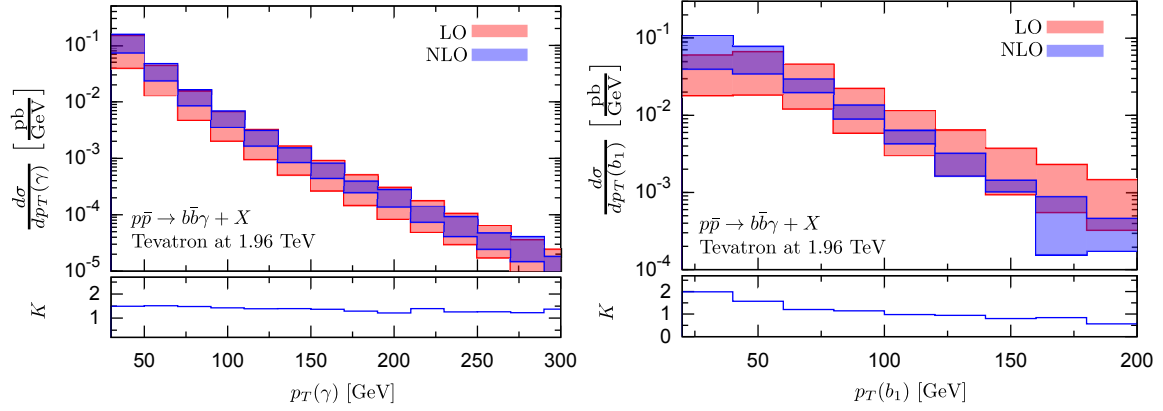


Figure 4.6: The upper plot shows the transverse-momentum distributions of the photon (left) and the leading  $b$  jet (right) for  $p\bar{p} \rightarrow b\bar{b}\gamma + X$  (at least two  $b$  jets identified in the final state) at the Tevatron with  $\sqrt{s} = 1.96$  TeV. The bands correspond to the variation of the renormalization and factorization scales in the interval  $\mu_0/4 < \mu < 4\mu_0$ . The lower plot shows the bin-by-bin  $K$ -factor for the corresponding distribution.

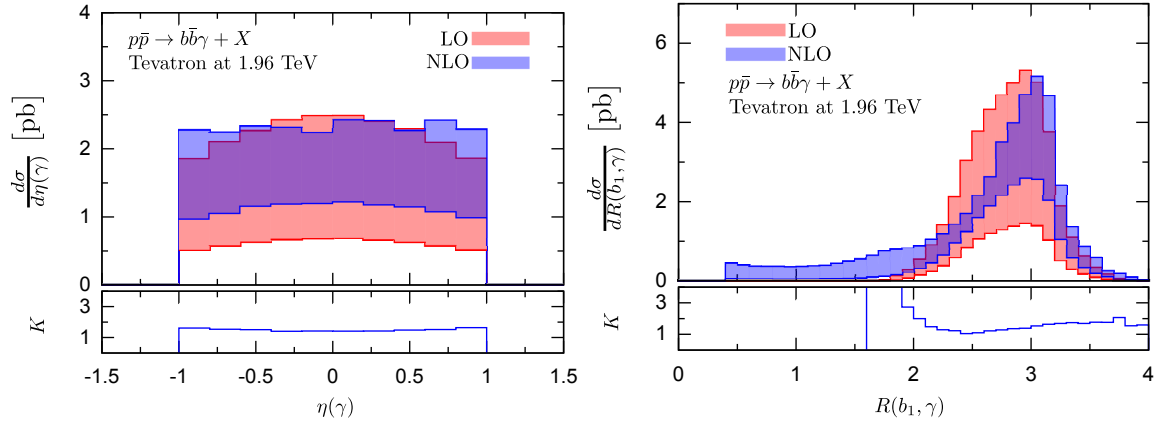


Figure 4.7: The upper plot shows the pseudorapidity distribution of final state photon (left) and the separation between the leading  $b$  jet and the photon (right) for  $p\bar{p} \rightarrow b\bar{b}\gamma + X$  (at least two  $b$  jets identified in the final state) at the Tevatron with  $\sqrt{s} = 1.96$  TeV. The bands correspond to the variation of the renormalization and factorization scales in the interval  $\mu_0/4 < \mu < 4\mu_0$ . The lower plot shows the bin-by-bin  $K$ -factor for the corresponding distribution.

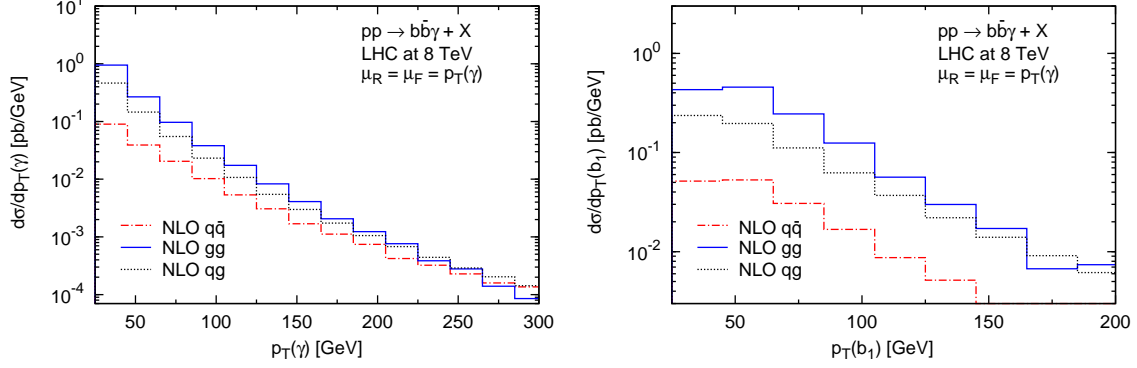


Figure 4.8: Individual contribution of the  $q\bar{q}$  (red),  $gg$  (blue) and  $qg$  (black) channels to the transverse-momentum distributions of the photon (left) and the leading  $b$  jet (right) for  $pp \rightarrow b\bar{b}\gamma + X$  (at least two  $b$  jets identified in the final state) at the LHC with  $\sqrt{s} = 8$  TeV, with  $\mu = p_T(\gamma)$ .

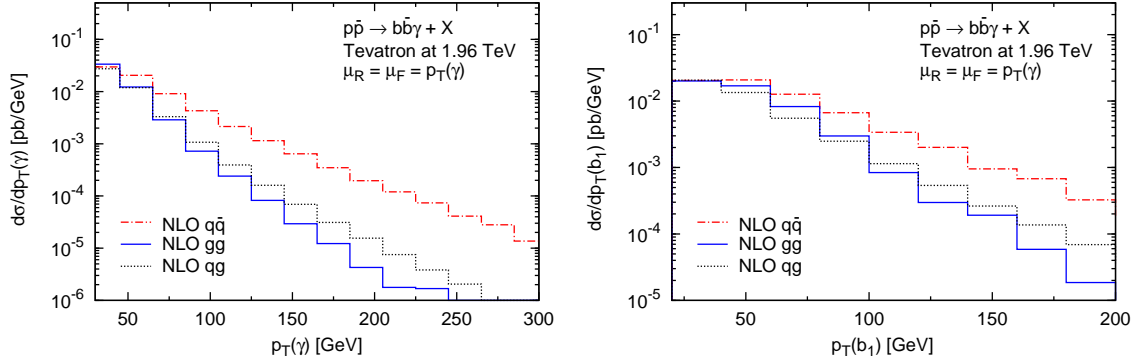


Figure 4.9: Individual contribution of the  $q\bar{q}$  (red),  $gg$  (blue) and  $qg$  (black) channels to the transverse-momentum distributions of the photon (left) and the leading  $b$  jet (right) for  $p\bar{p} \rightarrow b\bar{b}\gamma + X$  (at least two  $b$  jets identified in the final state) at the Tevatron with  $\sqrt{s} = 1.96$  TeV, with  $\mu = p_T(\gamma)$ .

Table 4.2: LO and NLO QCD total cross sections for  $pp(p\bar{p}) \rightarrow b(\bar{b})\gamma + X$  with at least one  $b$  jet tagged in the final state at the LHC ( $\sqrt{s} = 8$  TeV) and at the Tevatron ( $\sqrt{s} = 1.96$  TeV), together with their  $K$ -factor. The uncertainties are due to the dependence on the renormalization/factorization scale, obtained by evaluating the cross section at  $\mu = p_T(\gamma)/4$  for the upper value and at  $\mu = 4p_T(\gamma)$  for the lower value. The integration errors are well below 1%

Collider	$\sigma_{\text{LO}}$ [pb]	$\sigma_{\text{NLO}}$ [pb]	$K$ -factor
LHC at 8 TeV	$303^{+35\%}_{-59\%}$	$467^{+27\%}_{-53\%}$	1.4 - 1.7
Tevatron at 1.96 TeV	$14.4^{+45\%}_{-107\%}$	$26.9^{+35\%}_{-62\%}$	1.5 - 2.2

as large as the LO bands, in the whole  $p_T$  region. In contrast, at the Tevatron, the NLO bands are as large as the LO bands at low  $p_T$  and as  $p_T$  increases the NLO bands shrink noticeably. This can be understood by looking at the contribution of the different channels to the NLO differential distribution as shown in Figs. 4.8 and 4.9. At the LHC, both for  $p_T(\gamma)$  and  $p_T(b_1)$ , although the  $gg$  channel dominates, the contribution of the  $q\bar{q}$  channel, which suffers from strong scale dependence, is quite large. On the other hand, at the Tevatron, although in the low- $p_T$  region the  $gg$  and  $q\bar{q}$  channels dominate, starting from the intermediate- $p_T$  region, the  $q\bar{q}$  channel, which receives quite considerable improvement in the scale dependence when the NLO QCD corrections are included, starts to dominate while the contributions of the  $gg$  and  $qg$  channels drop rapidly.

### 4.3 $pp(p\bar{p}) \rightarrow b(\bar{b})\gamma + X$ : at least one $b$ jet identified in the final state

In this section we present the numerical results for  $b\bar{b}\gamma$  production where at least one  $b$  jet is tagged in the final state. This set of events include events with  $2b$  jets (see Sec. 4.2) as well as events with just  $1b$  jet that can result from either a single  $b$  or  $\bar{b}$  as well as from recombination of  $b$  and  $\bar{b}$ , or  $b$ ,  $\bar{b}$  and a light parton (quark/gluon) into a  $b$  jet that passes the selection cuts.

The scale dependence of the total cross section both for the LHC and the Tevatron are shown in Fig. 4.10. Similar to the  $2b$ -tag case, the improvement of the scale dependence is not significant when we go from LO to NLO. The  $K$ -factors are also sizeable in the  $1b$ -tag case, 1.4 to 1.7 for the LHC and 1.5 to 2.2 for the Tevatron, in the  $\mu_0/4 < \mu < 4\mu_0$  interval. The strong scale dependence at NLO is also due to the  $q\bar{q}$  channel, while the scale dependence of the  $q\bar{q}$  and  $gg$  channels are improved when the NLO QCD corrections are included, as shown in Fig. 4.11. We notice that the leading subprocesses in the total cross

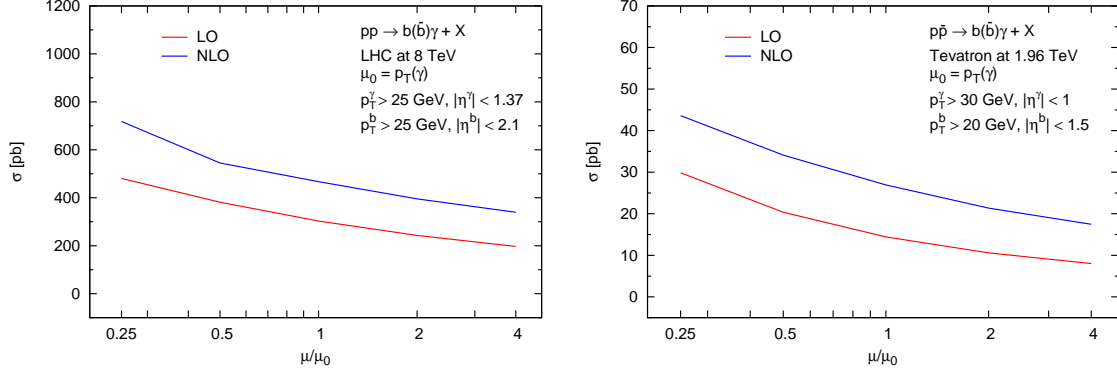


Figure 4.10: Dependence of the  $pp \rightarrow b(\bar{b})\gamma + X$  (at least one  $b$  jet identified in the final state) LO (red) and NLO (blue) cross section on the renormalization/factorization scale at the LHC with  $\sqrt{s} = 8$  TeV (left) and at the Tevatron with  $\sqrt{s} = 1.96$  TeV (right).

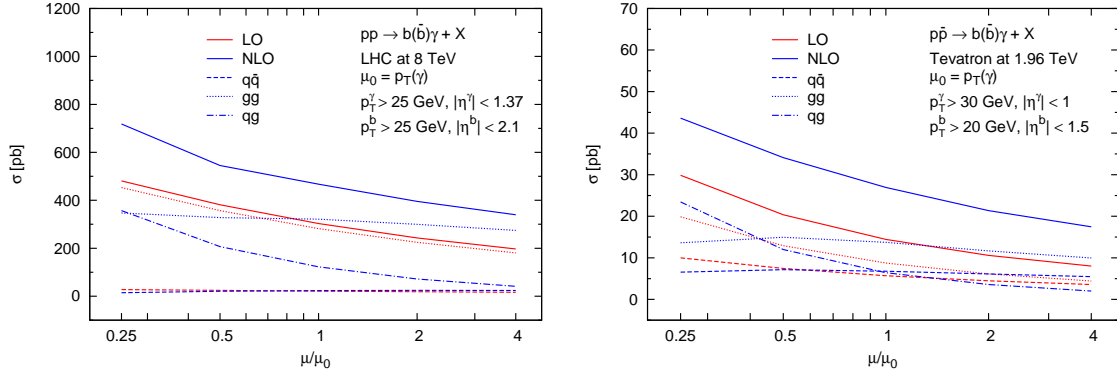


Figure 4.11: Dependence of the  $pp \rightarrow b(\bar{b})\gamma + X$  (at least one  $b$  jet identified in the final state) LO (red) and NLO (blue) cross section, with the  $q\bar{q}$  (dashed),  $gg$  (dotted), and  $qg$  (dash-dotted) channels individually shown, on the renormalization/factorization scale at the LHC with  $\sqrt{s} = 8$  TeV (left) and at the Tevatron with  $\sqrt{s} = 1.96$  TeV (right).

section are now  $gg$  and  $qg$  at both at the Tevatron and at the LHC. However, as we will see in Fig. 4.17, this is true at the level of distributions only for the LHC, while at the Tevatron the  $q\bar{q}$  subprocesses still dominates at medium and large  $p_T(\gamma)$  and  $p_T(b)$ . This will be important to understand the comparison between FFS/4FNS and VFS/5FNS that we will discuss in Sec. 4.4.

In Figs. 4.12 and 4.13 we show the photon and the  $b$ -jet transverse-momentum distribution, the photon pseudorapidity and the photon to  $b$ -jet separation ( $R(\gamma, b)$ ) distributions at the LHC. The impact of NLO QCD corrections to the differential distributions are quite significant. Similar to the  $2b$ -tag case, the  $K$ -factor for  $p_T(\gamma)$  and  $p_T(b)$  grows as  $p_T$  increases. The  $R(\gamma, b)$  distribution, however, does not exhibit the pinching that is present in the  $2b$ -tag case. In Figs. 4.14 and 4.15 we show the photon and the  $b$ -jet transverse-momentum distribution, the photon pseudorapidity, and the photon to  $b$ -jet separation distributions at the Tevatron. The  $K$ -factor for both the  $p_T(\gamma)$  and  $p_T(b)$  decreases as we go from the low- to high- $p_T$  region, similar to what we observed in the  $2b$ -tag case. In Figs. 4.16 and 4.17, the contribution of the  $q\bar{q}$ ,  $gg$ , and  $qg$  channels to the NLO distributions are shown, allowing us to argue that the strong scale dependence in the  $p_T(\gamma)$  and  $p_T(b)$  distributions at the LHC are due to the  $qg$  channel that contributes significantly, almost as much as the  $gg$  channel. On the other hand, at the Tevatron the scale dependence in the distributions shows quite an improvement as  $p_T(\gamma)$  or  $p_T(b)$  grows, due to the  $q\bar{q}$  channel that dominates in the intermediate- to high- $p_T$  regions.

## 4.4 Comparison between 5FNS and 4FNS calculations

In Sec. 2.7, we have discussed that the predictions for direct photon production in association with a bottom quark at hadron colliders,  $pp(p\bar{p}) \rightarrow \gamma + b + X$ , can be obtained from two different schemes. The first one is the 4FNS, where there is no initial state bottom quark in the partonic subprocess and the mass of the bottom quark is retained in the calculation. This is essentially the  $b\bar{b}\gamma$  calculation with at least one  $b$  jet tagged in the final state, whose results have been presented in the Sec. 4.3. The second scheme is the 5FNS, where the bottom quark is treated as massless and can be present in the initial state. In this scheme, the large logarithm that appears due to the phase-space integration of the unobserved  $b$  quark in the 4FNS is resummed and absorbed into the bottom-quark PDF. The calculation of  $pp(p\bar{p}) \rightarrow \gamma + b + X$  in the 5FNS has been reported in [57], where the fragmentation component up to  $\mathcal{O}(\alpha\alpha_s^2)$  is included. In this Section, we would like to compare the results for  $pp(p\bar{p}) \rightarrow \gamma + b + X$  from the two schemes at NLO QCD accuracy.

Since in our 4FNS calculation we employ the Frixione prescription for the photon isolation, we have to compare to 5FNS results that are obtained using the same photon isolation prescription. Since the 5FNS calculation in [57] includes the photon fragmentation contributions and uses a fixed cone isolation, we decided to reproduce results for the 5FNS with the Frixione isolation prescription using MCFM. In Table 4.4, we list all the subprocesses that contribute to the LO and NLO  $\gamma + b$  process. The required LO, virtual, and real matrix



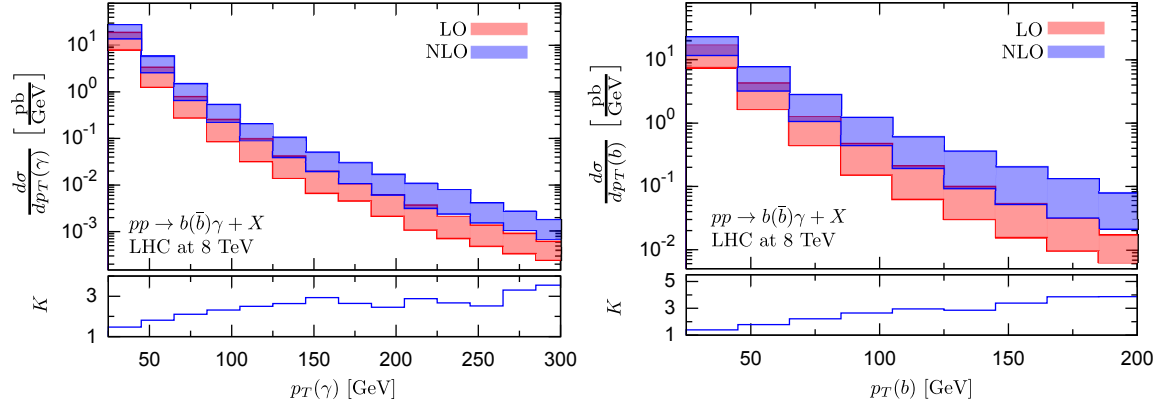


Figure 4.12: The upper plot shows the transverse-momentum distributions of the photon (left) and the  $b$  jet (right) for  $pp \rightarrow b(\bar{b})\gamma + X$  (at least one  $b$  jet identified in the final state) at the LHC with  $\sqrt{s} = 8$  TeV. The bands correspond to the variation of the renormalization and factorization scales in the interval  $\mu_0/4 < \mu < 4\mu_0$ . The lower plot shows the bin-by-bin  $K$ -factor for the corresponding distribution.

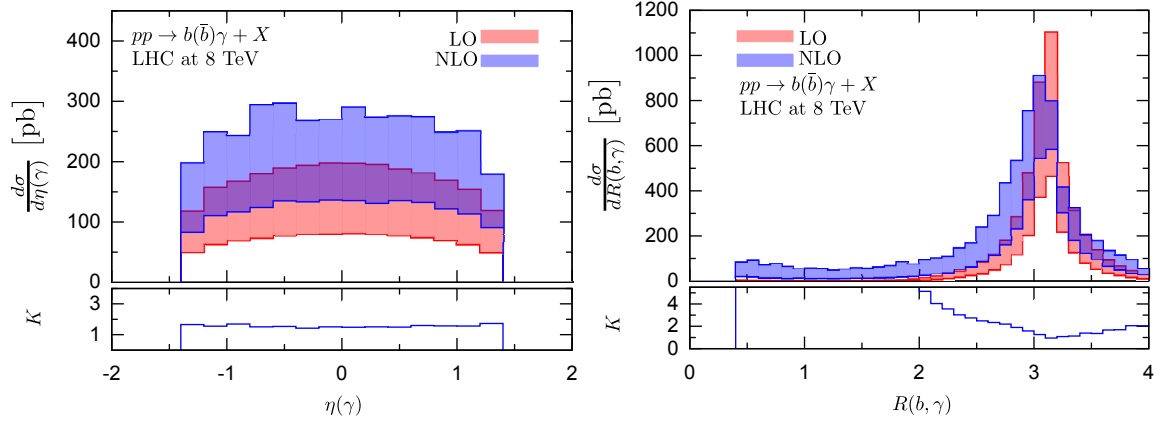


Figure 4.13: The upper plot shows the pseudorapidity distribution of the photon (left) and the separation between the  $b$  jet and the photon (right) for  $pp \rightarrow b(\bar{b})\gamma + X$  (at least one  $b$  jet identified in the final state) at the LHC with  $\sqrt{s} = 8$  TeV. The bands correspond to the variation of the renormalization and factorization scales in the interval  $\mu_0/4 < \mu < 4\mu_0$ . The lower plot shows the bin-by-bin  $K$ -factor for the corresponding distribution.

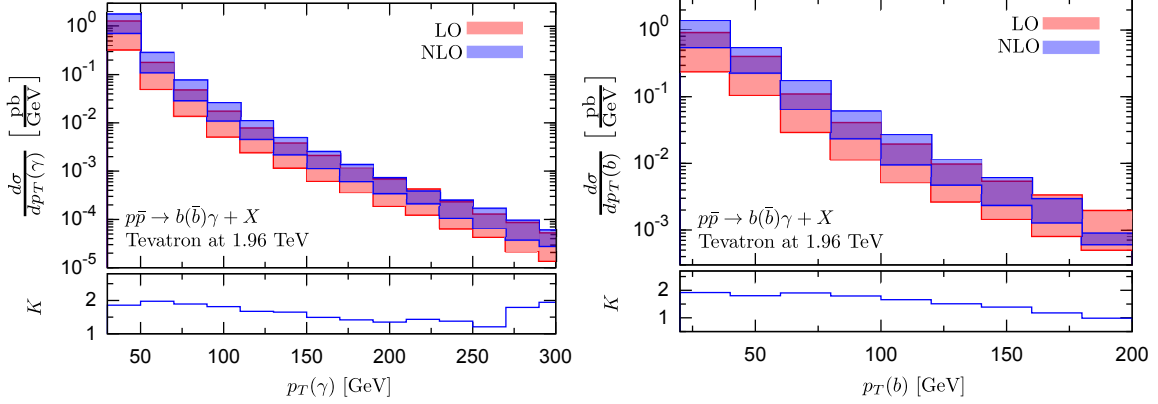


Figure 4.14: The upper plot shows the transverse-momentum distributions of the photon (left) and the  $b$  jet (right) for  $p\bar{p} \rightarrow b(\bar{b})\gamma + X$  (at least one  $b$  jet identified in the final state) at the Tevatron with  $\sqrt{s} = 1.96$  TeV. The bands correspond to the variation of the renormalization and factorization scales in the interval  $\mu_0/4 < \mu < 4\mu_0$ . The lower plot shows the bin-by-bin  $K$ -factor for the corresponding distribution.

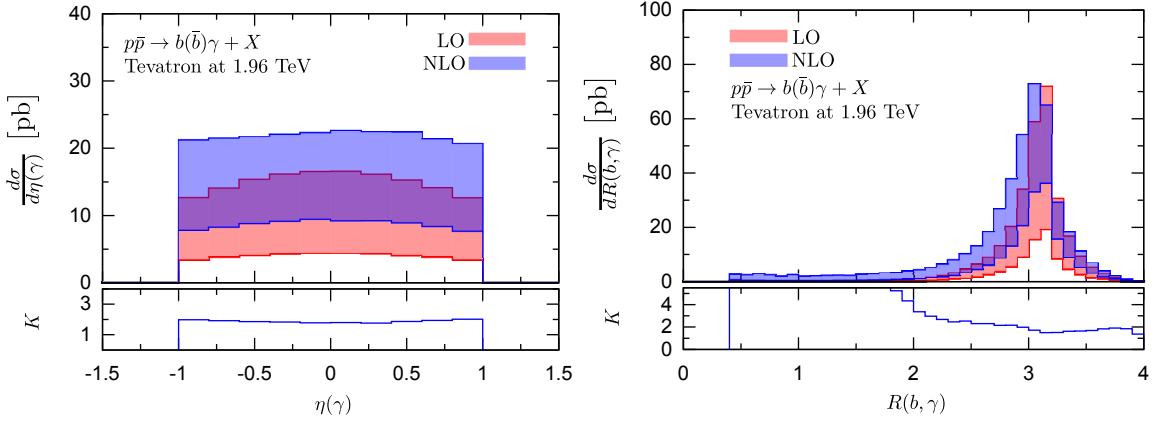


Figure 4.15: The upper plot shows the pseudorapidity distribution of the photon (left) and the separation between the  $b$  jet and the photon (right) for  $p\bar{p} \rightarrow b(\bar{b})\gamma + X$  (at least one  $b$  jet identified in the final state) at the Tevatron with  $\sqrt{s} = 1.96$  TeV. The bands correspond to the variation of the renormalization and factorization scales in the interval  $\mu_0/4 < \mu < 4\mu_0$ . The lower plot shows the bin-by-bin  $K$ -factor for the corresponding distribution.

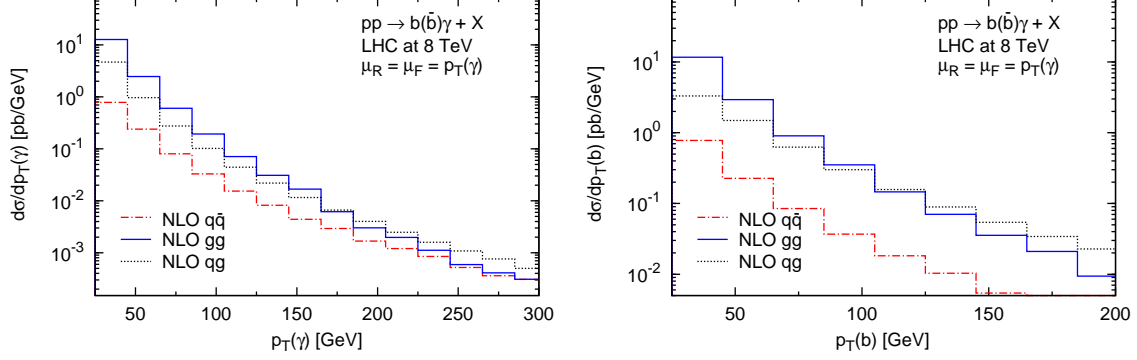


Figure 4.16: Individual contribution of the  $q\bar{q}$  (red),  $gg$  (blue) and  $qg$  (black) channels to the transverse-momentum distributions of the photon (left) and the  $b$  jet (right) for  $pp \rightarrow b(\bar{b})\gamma + X$  (at least one  $b$  jet identified in the final state) at the LHC with  $\sqrt{s} = 8$  TeV, with  $\mu = p_T(\gamma)$ .

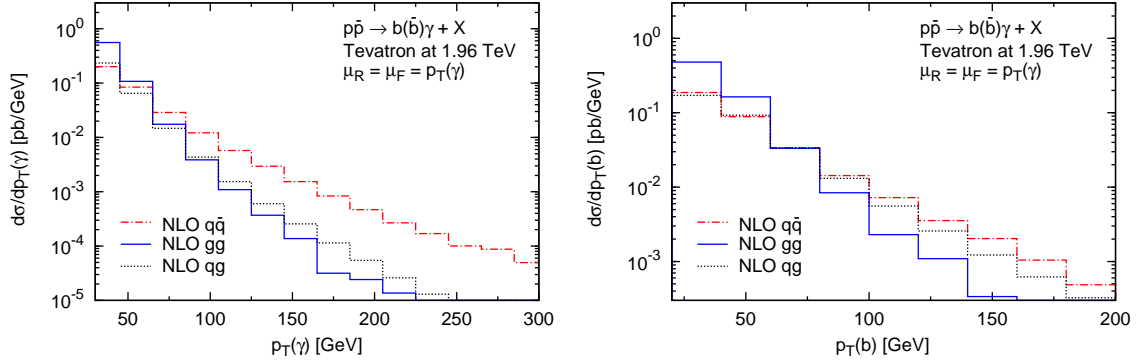


Figure 4.17: Individual contribution of the  $q\bar{q}$  (red),  $gg$  (blue) and  $qg$  (black) channels to the transverse-momentum distributions of the photon (left) and the  $b$  jet (right) for  $pp \rightarrow b(\bar{b})\gamma + X$  (at least one  $b$  jet identified in the final state) at the Tevatron with  $\sqrt{s} = 1.96$  TeV, with  $\mu = p_T(\gamma)$ .

Table 4.3: List of subprocesses that contribute to LO and NLO 5FNS calculation of  $pp(p\bar{p}) \rightarrow \gamma b + X$  process, with  $i = q, \bar{q}$  and  $Q = b, \bar{b}$ .

Part	Subprocess
LO and NLO virtual	$Qg \rightarrow \gamma Q$
NLO real	$Qg \rightarrow \gamma Qg$
	$iQ \rightarrow \gamma Qi$
	$QQ \rightarrow \gamma QQ$
	$q\bar{q} \rightarrow \gamma b\bar{b}$
	$gg \rightarrow \gamma b\bar{b}$

elements have been implemented in **MCFM** for direct photon production at hadron colliders,  $pp(p\bar{p}) \rightarrow \gamma + \text{jet} + X$ . Our task is to select the partonic channels that are listed in Table 4.4 from the  $pp(p\bar{p}) \rightarrow \gamma + \text{jet} + X$  process and to implement the correct  $b$ -jet selection criteria.

In Figs. 4.18 and 4.19, the comparison between the 4FNS and 5FNS calculations for the photon and the  $b$ -jet transverse-momentum distributions at the LHC and at the Tevatron are shown. Both at the LHC and at the Tevatron, the 4FNS calculation is compatible with the 5FNS calculation. The behavior of the scale variation band is, however, different from the LHC and the Tevatron. At the LHC the distributions from the 5FNS calculation have smaller scale-uncertainty band compared to the 4FNS counterparts. As it has been discussed in [57], at the LHC, the dominant contribution to the  $p_T(\gamma)$  distribution comes from the  $Qg \rightarrow \gamma Q$ ,  $gg \rightarrow \gamma b\bar{b}$ , and  $Qg \rightarrow \gamma Qg$  channels, where the potentially large logarithms have been resummed in the  $b$ -PDF resulting in the better scale-dependence behavior. On the other hand, at the Tevatron, while the scale-variation bands from the 5FNS calculation are smaller than the 4FNS calculation at low- $p_T$ , as  $p_T$  increases, the 5FNS bands are getting larger, while the 4FNS bands get slightly smaller. As we have seen in Fig. 4.20, the  $q\bar{q} \rightarrow b\bar{b}\gamma$  channel dominates in the intermediate- to high- $p_T$  region, and since this piece of the calculation enters in the 5FNS real correction as a tree level process, it still has a strong scale dependence.

#### 4.5 Impact of NLO QCD corrections on $p\bar{p} \rightarrow b\bar{b}\gamma$ process to the $\gamma + b + X$ theoretical prediction in comparison to the Tevatron data

The calculation of  $b\bar{b}\gamma$  production at NLO QCD accuracy allows us to improve the theoretical prediction of the  $pp(p\bar{p}) \rightarrow \gamma + b + X$  process at hadron colliders. Such theoretical prediction can be compared with the recent measurements of the  $\gamma + b + X$  process at the

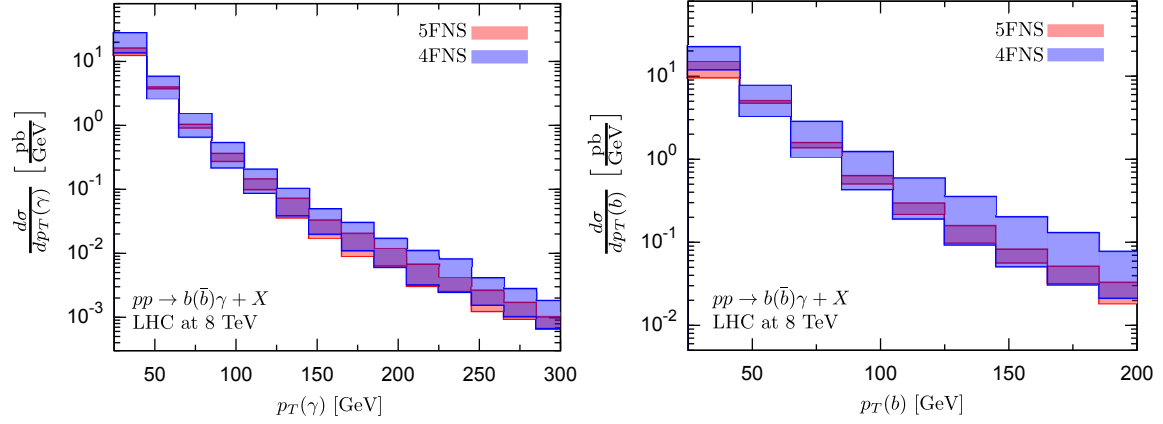


Figure 4.18: Transverse-momentum distributions of the photon (left) and the  $b$  jet (right) for  $pp \rightarrow \gamma + b + X$  (at least one  $b$  jet identified in the final state) at the LHC with  $\sqrt{s} = 8$  TeV, obtained from the 4FNS (blue) and the 5FNS (red) calculations. The bands correspond to the variation of the renormalization and factorization scales in the interval  $\mu_0/4 < \mu < 4\mu_0$ .

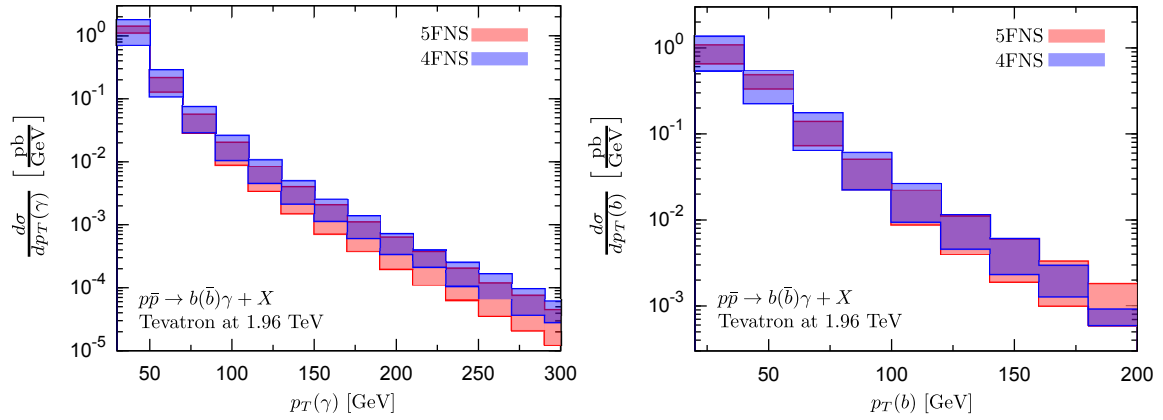


Figure 4.19: Transverse-momentum distributions of the photon (left) and the  $b$  jet (right) for  $p\bar{p} \rightarrow \gamma + b + X$  (at least one  $b$  jet identified in the final state) at the Tevatron with  $\sqrt{s} = 1.96$  TeV, obtained from the 4FNS (blue) and the 5FNS (red) calculations. The bands correspond to the variation of the renormalization and factorization scales in the interval  $\mu_0/4 < \mu < 4\mu_0$ .

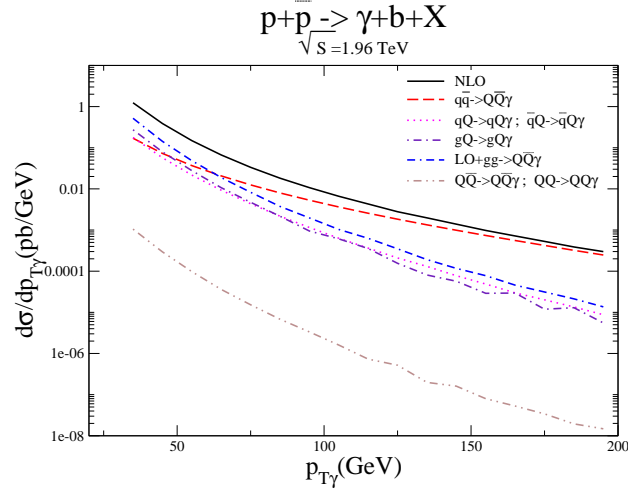


Figure 4.20: Different subprocesses that contribute to the NLO photon transverse-momentum distribution for  $p\bar{p} \rightarrow \gamma + b + X$  process, calculated using 5FNS approach, at the Tevatron [57]

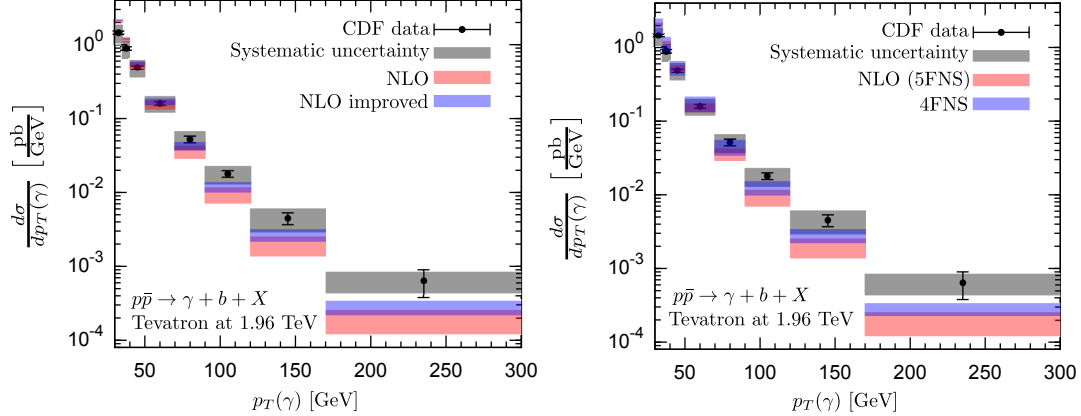


Figure 4.21: The photon- $p_T$  distribution for  $\gamma + b + X$  at the Tevatron with  $\sqrt{s} = 1.96$  TeV. The numbers for the CDF data and the NLO 5FNS calculation (red) [57] are taken from [56]. The bands correspond to the variation of the renormalization and factorization scales in the interval  $\mu_0/2 < \mu < 2\mu_0$ . The left plot shows the CDF data and the prediction from NLO 5FNS calculation compared with improved NLO 5FNS prediction (blue) that includes the NLO QCD corrections only to the  $q\bar{q} \rightarrow b(\bar{b})\gamma$  subprocess. The right plot shows the CDF data and the prediction from NLO 5FNS calculation compared with the prediction from the pure 4FNS calculation (blue).

Tevatron by the CDF [56] and the D0 [55] collaboration. However, the measurement of the  $\gamma + b + X$  process at the Tevatron employed the fixed-cone photon isolation as opposed to the Frixione’s smooth-cone isolation. This prevents us, at this point, to make a direct comparison with the Tevatron data, since in our calculation we have used the Frixione’s smooth-cone isolation. The proper comparison can be realized by including the fragmentation contribution to  $b\bar{b}\gamma$  production such that the fixed-cone photon isolation prescription can be used in the theoretical prediction. Nevertheless, as pointed out in Sec. 2.5, the photon isolation suppresses not only the ”secondary” photon production but also reduces the fragmentation contribution substantially. In view of this, a qualitative understanding on how the 4FNS calculation will affect the NLO prediction for the  $\gamma + b + X$  process is presented in this Section, and we expect that the final theoretical prediction (with the fragmentation component included and the fixed-cone isolation imposed) would be similar to our current prediction, since the contribution of the fragmentation process is relatively small.

In Sec. 1.3, we have discussed that the latest measurement on the  $\gamma + b + X$  final state at the Tevatron by both the CDF and D0 collaborations shows disagreement between the NLO 5FNS prediction and the experimental data in the  $p_T(\gamma) > 70$  GeV region (see Fig. 1.3). In this thesis we only show the comparison with the CDF data, since we have used their setup in obtaining numerical results for  $b\bar{b}\gamma$  production in Secs. 4.2 and 4.3. The very same comparison with the D0 data can be made, and will be presented in the forthcoming publication [61]. We obtain the approximate comparison between the NLO calculation and the CDF data by using two different approaches:

- The NLO 5FNS calculation for  $p\bar{p} \rightarrow \gamma + b + X$  is improved by including the NLO QCD corrections to the  $q\bar{q} \rightarrow b(\bar{b})\gamma$  subprocess in the whole  $p_T(\gamma)$  region. This approach relies on the fact that, as shown in Fig. 4.20, the tree level  $q\bar{q} \rightarrow b(\bar{b})\gamma$  subprocess, that comes in as a real correction in the NLO 5FNS calculation, is dominant in the  $p_T(\gamma) > 70$  GeV region. In the left panel of Fig. 4.21, we show the comparison of the improved NLO 5FNS calculation with the CDF data for the  $\gamma + b + X$  process, where we have included the NLO QCD corrections to the  $q\bar{q} \rightarrow b(\bar{b})\gamma$  subprocess.
- The theoretical prediction is obtained from the pure NLO 4FNS calculation of the  $p\bar{p} \rightarrow \gamma + b + X$  process. As demonstrated in Sec. 4.4, our 4FNS calculation for the  $\gamma + b + X$  production at hadron colliders is compatible with the 5FNS calculation. In the right panel of Fig. 4.21, we show the comparison of the pure NLO 4FNS calculation with the CDF data for the  $\gamma + b + X$  process at the Tevatron.

We see in Fig. 4.21 that the inclusion of the NLO QCD corrections to the  $p\bar{p} \rightarrow b(\bar{b})\gamma$  process via two approaches that are discussed above improve the agreement between NLO 5FNS calculation and the Tevatron data. Still, we need to take this comparison with some caution since the 4FNS result that we add indeed uses a different isolation prescriptions for the photon that the experimental measurement (i.e. Frixione’s vs fixed-cone isolation). In addition, in the first approach, where the NLO 5FNS calculation is improved by including the NLO QCD corrections to the  $q\bar{q} \rightarrow b(\bar{b})\gamma$  subprocess, we need to properly add the  $(gg, qg) \rightarrow b(\bar{b})\gamma$  channel from the 4FNS calculation by including subtraction terms that avoid the double counting of the logarithmic terms already resummed into the  $b$ -quark PDF.

A final comparison between the Tevatron data and the NLO prediction will be provided once the fragmentation contributions in  $b\bar{b}\gamma$  production are implemented.



## CHAPTER 5

# CONCLUSIONS AND OUTLOOK

In this thesis we have presented the calculation of the heavy-quark associated production with a hard photon at hadron colliders ( $pp(p\bar{p}) \rightarrow Q\bar{Q}\gamma + X$ ) where we have considered the top and the bottom quarks in the final state ( $Q = t, b$ ), including NLO QCD corrections. The calculation of the  $\mathcal{O}(\alpha_s)$  virtual amplitudes is performed using the Feynman-diagram approach while the singularities in the  $\mathcal{O}(\alpha_s)$  real-correction amplitudes are isolated using the phase-space slicing method with two cutoffs [85]. Cross checks are done both on the virtual corrections, by using the NLOX package [16] to compute one-loop amplitudes, and on the real corrections, using independent implementation of the PSS2 method as well as interfacing with the SHERPA package [19, 20] that implements the Catani-Seymour dipole subtraction method [21, 22]. The presence of the photon in the final state requires an isolation procedure to suppress the "secondary" photon production, and we have used the Frixione smooth cone isolation prescription [92] to handle the quark-photon final state singularities that appear in our calculation.

We have found that NLO QCD corrections to  $t\bar{t}\gamma$  production both at the LHC with  $\sqrt{s} = 8$  TeV and at the Tevatron with  $\sqrt{s} = 1.96$  TeV improve the renormalization/factorization scale dependence of the total cross section and the differential distributions. NLO QCD corrections are sizeable at the LHC and moderate at the Tevatron. We noticed also the presence of a top-quark forward-backward asymmetry at the Tevatron, and such asymmetry is reduced from LO to NLO. For  $b\bar{b}\gamma$  production, we consider the final states where at least two  $b$  jets are identified ( $2b$ -tag) and at least one  $b$  is identified ( $1b$ -tag). For both the  $2b$ -tag and the  $1b$ -tag case, at the LHC and at the Tevatron, the NLO QCD corrections are large and there is no improvement in renormalization/factorization scale dependence from LO to NLO. The  $q\bar{q}$  and  $gg$  channels themselves are well-behaved when the NLO QCD corrections are included. The strong residual scale dependence is due to the  $qg$  channel that enters the NLO calculation at tree level. The results for  $b\bar{b}\gamma$  production where at least one  $b$  jet is identified in the final state can be obtained from both the 4FNS and the 5FNS approaches. We found that our  $b\bar{b}\gamma$  calculation, which uses the 4FNS approach, is compatible with the 5FNS calculation as implemented in MCFM [8]. We finally address the comparison between the theoretical prediction and the measurement by the CDF collaboration of the  $\gamma + b + X$  process at the Tevatron [56]. The very same comparison, however, can be obtained also for the D0 measurement, which we will present in the forthcoming publication [61]. We

only show the comparison for the CDF measurement in this thesis since we have used the setup from the CDF measurement to present the numerical results for  $b\bar{b}\gamma$  production at the Tevatron. There are some discrepancies between the measured  $p_T(\gamma)$  distribution (both from the CDF and D0 collaborations) and the NLO 5FNS calculation [57] at  $p_T(\gamma) > 70$  GeV. Our 4FNS calculation can not be compared directly to the experimental data due to the different photon isolation prescription. However, we presented approximate comparisons of the theoretical prediction with the CDF data both by including the NLO QCD corrections to the  $q\bar{q} \rightarrow b(\bar{b})\gamma$  channel in the NLO 5FNS calculation and by taking the pure NLO 4FNS calculation of the  $p\bar{p} \rightarrow b(\bar{b})\gamma$  process, resulting in a better agreement between the theoretical predictions and the data.

A final comparison with the  $\gamma + b$  measurement can be obtained by including the photon-fragmentation contributions to the 4FNS calculation which would allow to impose the fixed-cone isolation prescription as used in the experiments. Such fragmentation contributions are currently being implemented and a comparison between the data and the theoretical prediction will be presented in the near future. Another possible extension of our  $t\bar{t}\gamma$  and  $b\bar{b}\gamma$  calculation would be to study the effect of showering with both the MC@NLO method [28] by using the SHERPA interface, and the POWHEG method [29, 30] by using the POWHEG-BOX framework [100]. In addition, it is also important to include the NLO QCD corrections to the  $qg(\bar{q}g) \rightarrow b\bar{b}\gamma + q(\bar{q})$  subprocess to obtain an improvement on its scale uncertainty. Strictly speaking, this would be part of the NNLO QCD corrections to  $\gamma + b$  hadroproduction, but represents a self-contained and gauge-invariant subset of NNLO corrections and it is therefore interesting to study its effect on the total and differential cross sections, at least to the extent that it could dramatically reduce the uncertainty due to the scale dependence.

# APPENDIX A

## THE STANDARD MODEL

The Standard Model is a quantum field theory based on the gauge groups  $SU(3)$  for color,  $SU(2)$  for weak isospin, and  $U(1)$  for hypercharge, as dictated by the local gauge symmetry invariance observed in the behavior of fundamental particles. The color quantum number is associated with the dynamics of the strong interactions, which by itself is the subject of Quantum Chromodynamics (QCD), while the weak isospin and hypercharge quantum numbers are fundamental to the dynamics of electroweak interactions.

The SM Lagrangian can be written as

$$\mathcal{L}_{SM} = \mathcal{L}_{YM} + \mathcal{L}_f + \mathcal{L}_H + \mathcal{L}_{Yuk} , \quad (\text{A.1})$$

where  $\mathcal{L}_{YM}$  is the Yang-Mills Lagrangian,  $\mathcal{L}_f$  the fermion Lagrangian,  $\mathcal{L}_H$  the Higgs Lagrangian and  $\mathcal{L}_{Yuk}$  contains the Yukawa interactions of the theory.  $\mathcal{L}_{YM}$  describes the dynamics of the pure gauge fields (kinetic terms + self-interactions) and includes the following terms

$$\begin{aligned} \mathcal{L}_{YM} &= \mathcal{L}_{QCD} + \mathcal{L}_{I_w} + \mathcal{L}_Y \\ &= -\frac{1}{4} \sum_{A=1}^8 G_{\mu\nu}^A G^{A\mu\nu} - \frac{1}{4} \sum_{a=1}^3 F_{\mu\nu}^a F^{a\mu\nu} - \frac{1}{4} B_{\mu\nu} B^{\mu\nu}. \end{aligned} \quad (\text{A.2})$$

The color field strength tensor is given by

$$G_{\mu\nu}^A = \partial_\mu A_\nu^A - \partial_\nu A_\mu^A + g_1 f^{ABC} A_\mu^B A_\nu^C , \quad A, B, C = 1, \dots, 8 , \quad (\text{A.3})$$

with  $A_\mu^B$  the eight color gauge fields (so called gluons),  $g_1$  the dimensionless strong coupling constant, and  $f^{ABC}$  the structure constants of  $SU(3)$ . Analogously, the weak isospin,  $F_{\mu\nu}^a$ , and hypercharge,  $B_{\mu\nu}$ , field strength tensors are given by

$$F_{\mu\nu}^a = \partial_\mu W_\nu^a - \partial_\nu W_\mu^a + g_2 \epsilon^{abc} W_\mu^a W_\nu^b , \quad a, b, c = 1, 2, 3 , \quad (\text{A.4})$$

$$B_{\mu\nu} = \partial_\mu B_\nu - \partial_\nu B_\mu , \quad (\text{A.5})$$

where  $W_\mu^a$  and  $B_\mu$  are the 4 electroweak gauge bosons (a linear combination of which will become the weak  $W_\mu^\pm$  and  $Z_\mu^0$  weak gauge bosons plus the photon  $A_\mu$ ),  $g_2$  is the dimensionless

weak isospin coupling constant and  $\epsilon^{abc}$  are the structure constants of  $SU(2)$ . Throughout the body of this thesis we have denoted the strong coupling  $g_1$  as  $g_s$ , and the weak isospin coupling  $g_2$  as  $g_w$ . We also use the conventional definition  $\alpha_s = g_s^2/(4\pi)$ .

The second part of the SM Lagrangian in Eq. A.1,  $\mathcal{L}_f$ , describes the fermion fields and their interactions with the gauge bosons. The fermion fields are classified as quarks, which are triplets under the color gauge group, and leptons, which have no color. Taking into account the fact that the  $W$  boson couples only to left-handed helicity states of quarks and leptons, this part of the Lagrangian is built such that right-handed and left-handed components of the fermion fields couple independently to the gauge bosons. Using the notation  $(SU(2), SU(3))_Y$ , to denote weak isospin, color, and hypercharge quantum numbers assignments of the fermion fields, we can write that a quark weak doublet,  $\mathbf{Q}_L = (\mathbf{u}_L, \mathbf{d}_L)^T$ , is a  $(\mathbf{2}, \mathbf{3})_{y_1}$ , an up-type quark weak singlet,  $\mathbf{u}_R$ , is a  $(\mathbf{1}, \mathbf{3})_{y_2}$ , and a down-type quark weak singlet,  $\mathbf{d}_R$ , is a  $(\mathbf{1}, \mathbf{3})_{y_3}$ . On the other side, a weak doublet of leptons,  $L_L = (\nu_e, e)^T$ , is a  $(\mathbf{2}, \mathbf{1})_{y_4}$  and a lepton weak singlet,  $e_R$ , is a  $(\mathbf{1}, \mathbf{1})_{y_5}$ . The hypercharge quantum number,  $y_i$ , is given by the following relation,

$$y_i = Q_i - T_{3i}, \quad (\text{A.6})$$

where  $Q_i$  is the electric charge and  $T_{3i}$  is the third component of weak isospin of the field  $i$  respectively. The fermion Lagrangian  $\mathcal{L}_f$  then can be written as

$$\begin{aligned} \mathcal{L}_f = & \bar{\mathbf{Q}}_L \sigma^\mu \mathcal{D}_\mu \mathbf{Q}_L + \bar{\mathbf{u}}_R \sigma^\mu \mathcal{D}_\mu \mathbf{u}_R + \bar{\mathbf{d}}_R \sigma^\mu \mathcal{D}_\mu \mathbf{d}_R \\ & + \bar{L}_L \sigma^\mu \mathcal{D}_\mu L_L + \bar{e}_R \sigma^\mu \mathcal{D}_\mu e_R + \dots, \end{aligned} \quad (\text{A.7})$$

where the dots stand for similar terms for the remaining quarks and leptons. In Eq. A.7  $\sigma^\mu$  are the Pauli matrices ( $\sigma^0 = \mathbf{1}$ ), and  $\mathcal{D}_\mu$  are the covariant derivatives corresponding to each field,

$$\begin{aligned} \mathcal{D}_\mu \mathbf{Q}_L &= (\partial_\mu + g_1 \frac{i}{2} A_\mu^A \lambda^A + g_2 \frac{i}{2} W_\mu^a \tau^a + g_3 \frac{i}{2} y_1 B_\mu) \mathbf{Q}_L, \\ \mathcal{D}_\mu \mathbf{u}_R &= (\partial_\mu + g_1 \frac{i}{2} A_\mu^A \lambda^A + g_3 \frac{i}{2} y_2 B_\mu) \mathbf{u}_R, \\ \mathcal{D}_\mu \mathbf{d}_R &= (\partial_\mu + g_1 \frac{i}{2} A_\mu^A \lambda^A + g_3 \frac{i}{2} y_3 B_\mu) \mathbf{d}_R, \\ \mathcal{D}_\mu L_L &= (\partial_\mu + g_2 \frac{i}{2} W_\mu^a \tau^a + g_3 \frac{i}{2} y_4 B_\mu) L_L, \\ \mathcal{D}_\mu e_R &= (\partial_\mu + g_3 \frac{i}{2} y_5 B_\mu) e_R, \end{aligned} \quad (\text{A.8})$$

where  $g_3$  is the dimensionless hypercharge coupling constant, and  $\tau^a$  and  $\lambda^A$  are the Pauli and Gell-Mann matrices for  $SU(2)$  and  $SU(3)$  respectively.

Notice that a mass term for the fermion fields and for the vector boson fields (as needed for the weak vector bosons  $W_\mu^\pm$  and  $Z_\mu^0$ ) is not allowed by gauge invariance. The last two terms in the Standard Model Lagrangian shown in Eq. A.1 are introduced to remedy this problem. Indeed, the simplest way to preserve the gauge symmetry of the SM while generating massive electroweak gauge bosons is the so called Higgs mechanism, which we explain

in the following. A separate step needs to be taken to introduce massive fermions, and we will discuss this afterward.

The Higgs mechanism, in its simplest version [101, 102, 103, 104], starts by adding to the model another complex scalar field, called the Higgs field  $H$ , which transforms as a weak isospin doublet, a color singlet and it has hypercharge  $y_h$ :

$$H = \begin{pmatrix} H_1 \\ H_2 \end{pmatrix} \sim (\mathbf{2}, \mathbf{1}^c)_{y_h} . \quad (\text{A.9})$$

Its dynamics are dictated by the  $\mathcal{L}_H$  term in Eq. A.1, which can be written as

$$\mathcal{L}_H = (\mathcal{D}_\mu H)^\dagger (\mathcal{D}^\mu H) - V(H) , \quad (\text{A.10})$$

where  $\mathcal{D}_\mu H = (\partial_\mu + g_2 \frac{i}{2} W_\mu^a \tau^a + g_3 \frac{i}{2} y_h B_\mu) H$  is the covariant derivative of  $H$  and  $V(H)$  is the most general renormalizable potential invariant under  $SU(2) \times U(1)$ ,

$$V(H) = \mu^2 H^\dagger H + \lambda (H^\dagger H)^2 , \quad (\text{A.11})$$

with  $\mu^2$  and  $\lambda$  real arbitrary parameters.  $\lambda$  is a dimensionless parameter.

If  $\mu^2 < 0$  the field configurations that minimizes the potential  $V(H)$  have to satisfy:

$$H_{vac}^\dagger H_{vac} = \frac{-\mu^2}{2\lambda} \equiv \frac{v^2}{2} . \quad (\text{A.12})$$

So, once  $\mu^2 < 0$  the Higgs field develops a vacuum expectation value (VEV), which is degenerate over the sphere defined in the last equation. Picking one configuration breaks this degeneracy, causing the vacuum of the theory not to be  $SU(2) \times U(1)$  symmetric anymore. To illustrate the consequences, let us choose:

$$\langle H \rangle = \frac{v}{\sqrt{2}} \begin{pmatrix} 0 \\ 1 \end{pmatrix} . \quad (\text{A.13})$$

Indeed one can verify that this choice breaks the original gauge symmetry:

$$SU(2) \times U(1) \rightarrow U(1)_{EM} , \quad (\text{A.14})$$

where  $U(1)_{EM}$  is the electromagnetic  $U(1)$  symmetry.

When  $\mathcal{L}_H$  is expanded in the vicinity of the chosen minimum, by shifting the Higgs field as follows

$$H = \frac{1}{\sqrt{2}} \begin{pmatrix} 0 \\ v + h \end{pmatrix} , \quad (\text{A.15})$$

$\mathcal{L}_H$  becomes the Lagrangian of a real scalar field with mass  $m_h = 2v^2\lambda$ , the physical Higgs boson. Moreover, a mass term for the gauge bosons is generated by the first term in Eq. A.10, coming from

$$\frac{1}{2}(0, v) \left( \frac{1}{2} g_2 W_\mu^a \tau^a + \frac{1}{2} g_3 B_\mu \right)^2 \begin{pmatrix} 0 \\ v \end{pmatrix} . \quad (\text{A.16})$$

The corresponding mass eigenstates , i.e. the physical gauge fields, are obtained by diagonalizing the mass matrix of the vector fields  $W_\mu^a$  and  $B_\mu$ . The EW gauge bosons  $W_\mu^\pm$  and  $Z_\mu^0$ , as well as the photon  $A_\mu$ , are expressed as:

$$\begin{aligned} W_\mu^\pm &= \frac{1}{\sqrt{2}}(W_\mu^1 \mp iW_\mu^2) , \\ Z_\mu &= \frac{-g_3 B_\mu + g_2 W_\mu^3}{\sqrt{g_2^2 + g_3^2}} , \\ A_\mu &= \frac{g_2 B_\mu + g_3 W_\mu^3}{\sqrt{g_2^2 + g_3^2}} , \end{aligned} \tag{A.17}$$

with the associated masses:

$$\begin{aligned} M_W^2 &= \frac{1}{4}g_2^2 v^2 , \\ M_Z^2 &= \frac{1}{4}(g_2^2 + g_3^2)v^2 , \\ M_A &= 0 . \end{aligned} \tag{A.18}$$

These simple relations are found to agree with experiment ( $M_W = 80.4$  GeV,  $M_Z = 91.2$  GeV) with  $v \approx 174\sqrt{2}$  GeV. This is, of course, approximate as they are results based on the classical, or leading order approximation of the theory.

Finally let us focus on the last part of the SM Lagrangian presented in Eq. A.1. This term,  $\mathcal{L}_{\text{Yuk}}$ , couples massive fermion fields to the Higgs field via Yukawa type interaction. For example, the gauge invariant Yukawa coupling of the Higgs boson to the down quark,  $\mathbf{d}$ , is

$$-\lambda_d \overline{\mathbf{Q}}_L H \mathbf{d}_R + h.c. ,$$

where  $\overline{\mathbf{Q}}_L = (\overline{\mathbf{u}}, \overline{\mathbf{d}})_L$  and  $\lambda_d$  is the Yukawa coupling for the down quark. After the shift of Eq. A.15 this term gives the effective coupling

$$-\lambda_d \frac{1}{\sqrt{2}} \overline{\mathbf{Q}}_L \begin{pmatrix} 0 \\ v + h \end{pmatrix} \mathbf{d}_R + h.c. , \tag{A.19}$$

which gives a mass term to the down quark with

$$m_d = \frac{\lambda_d v}{\sqrt{2}} , \tag{A.20}$$

and defines the coupling between the down quark and the physical Higgs particle to be  $-\lambda_d/\sqrt{2}$ . Similar terms are added for each massive fermion field. Then  $\mathcal{L}_{\text{Yuk}}$  will contain 9 arbitrary parameters, the Yukawa couplings, standing for 6 quark masses and 3 lepton masses.

The Feynman rules for SM can be constructed from the Lagrangian in Eq. A.1, and the ones that are used in our calculation are shown in Fig A.1 for the interaction vertices, and

in Fig. A.2 for the propagators. The three- and four-gluon vertex functions in Fig. A.1 are given by,

$$V_{3;\mu\nu\rho}(k, p, q) = g_{\mu\nu}(k - p)_\rho + g_{\nu\rho}(p - q)_\mu + g_{\rho\mu}(q - k)_\nu, \quad (\text{A.21})$$

$$\begin{aligned} V_{4;\mu\nu\rho\sigma}^{abcd} = & f^{abe} f^{cde} (g_{\mu\rho} g_{\nu\sigma} - g_{\mu\sigma} g_{\nu\rho}) + f^{ace} f^{bde} (g_{\mu\nu} g_{\rho\sigma} - g_{\mu\sigma} g_{\nu\rho}) \\ & + f^{ace} f^{bde} (g_{\mu\nu} g_{\rho\sigma} - g_{\mu\rho} g_{\nu\sigma}). \end{aligned} \quad (\text{A.22})$$

$$\begin{aligned}
& \text{Quark-Gluon vertex: } i \text{ (quark), } j \text{ (quark), } \mu, a \text{ (gluon)} \quad = ig_s t_{ij}^a \gamma_\mu \\
& \text{Quark-Photon vertex: } i \text{ (quark), } j \text{ (quark), } \mu \text{ (photon)} \quad = ie Q_q \delta_{ij} \gamma_\mu \\
& \text{Three-gluon vertex: } \mu, a, \rho, c, \nu, b \text{ (gluons)} \quad = g_s f^{abc} V_{3; \mu \nu \rho}(k, p, q) \\
& \text{Quark-Ghost vertex: } a \text{ (ghost), } \mu, b \text{ (gluon)} \quad = -g_s f^{abc} p_\mu \\
& \text{Four-gluon vertex: } \mu, a, \nu, b, \rho, c, \sigma, d \text{ (gluons)} \quad = -ig_s^2 V_{4; \mu \nu \rho \sigma}
\end{aligned}$$

Figure A.1: SM Feynman rules for interaction vertices that are used in the calculation of  $Q\bar{Q}\gamma$  production.

$$\begin{aligned}
& \text{Gluon propagator: } \mu, a, \nu, b \text{ (gluons), } k \text{ (momentum)} \quad = \frac{-ig_{\mu\nu} \delta^{ab}}{k^2 + i\epsilon} \\
& \text{Quark propagator: } j, i \text{ (quarks), } p \text{ (momentum)} \quad = \frac{i\delta_{ij} (\not{p} + m_q)}{p^2 - m_q^2 + i\epsilon} \\
& \text{Ghost propagator: } b, a \text{ (ghosts), } p \text{ (momentum)} \quad = \frac{i\delta^{ab}}{p^2 + i\epsilon}
\end{aligned}$$

Figure A.2: SM Feynman rules for the propagators that are used in the calculation of  $Q\bar{Q}\gamma$  production.



# APPENDIX B

## LEADING ORDER AMPLITUDES

In this Appendix we present the explicit expressions for the LO amplitudes for  $Q\bar{Q}\gamma$  production at hadron colliders. The Feynman diagrams for the LO process are shown in Figs. 2.2 and 2.3. The structure of the LO amplitudes both for the  $q\bar{q}$  and the  $gg$  subprocesses is briefly discussed in Sec. 2.2. The LO amplitudes evaluated using the standard Dirac spinor technique are presented in Sec. B.1, while the ones obtained using the spinor-helicity formalism are presented in Sec. B.2.

### B.1 LO amplitudes using Dirac spinor technique

Given the momenta assignment in Eq. 2.10, the individual tree-level contributions to the  $q\bar{q} \rightarrow Q\bar{Q}\gamma$  amplitude in Eq. 2.13, are given by,

$$\mathcal{A}_1^{q\bar{q}} = i \frac{eg_s^2 Q_Q}{s_{12}s_{35}} [\bar{v}_2 \gamma^\mu u_1] [\bar{u}_3 \not{\epsilon}_5^* (\not{p}_3 + \not{p}_5 + m_Q) \gamma_\mu v_4], \quad (\text{B.1})$$

$$\mathcal{A}_2^{q\bar{q}} = i \frac{eg_s^2 Q_Q}{s_{12}s_{45}} [\bar{v}_2 \gamma^\mu u_1] [\bar{u}_3 \gamma_\mu (-\not{p}_4 - \not{p}_5 + m_Q) \not{\epsilon}_5^* v_4], \quad (\text{B.2})$$

$$\mathcal{A}_3^{q\bar{q}} = -i \frac{eg_s^2 Q_q}{(s_{34} + 2m_t^2)s_{15}} [\bar{v}_2 \gamma^\mu (\not{p}_1 - \not{p}_5) \not{\epsilon}_5^* u_1] [\bar{u}_3 \gamma_\mu v_4], \quad (\text{B.3})$$

$$\mathcal{A}_4^{q\bar{q}} = -i \frac{eg_s^2 Q_q}{(s_{34} + 2m_t^2)s_{25}} [\bar{v}_2 \not{\epsilon}_5^* (-\not{p}_2 + \not{p}_5) \gamma^\mu u_1] [\bar{u}_3 \gamma_\mu v_4], \quad (\text{B.4})$$

where  $e$  and  $g_s$  are the EM and strong coupling constants, respectively, and  $Q_Q$  ( $Q_q$ ) is the electric charge of the heavy (light) quark in units of  $|e|$ . The amplitudes in Eqs. B.1 - B.4 have been labelled after the Feynman diagrams in Fig. 2.2. Similarly, the individual tree-level contributions to the  $gg \rightarrow Q\bar{Q}\gamma$  amplitude in Eq. 2.16, with momenta assignment as

in Eq. 2.11, are given by,

$$\mathcal{A}_1^{gg} = i \frac{e g_s^2 Q Q}{s_{35} s_{12}} [\bar{u}_3 \gamma^\lambda (\not{p}_3 + \not{p}_5 + m_Q) \gamma_\nu v_4] V_3^{\mu\nu\sigma}(p_1, -p_1 - p_2, p_2) \varepsilon_{1\mu} \varepsilon_{2\nu} \varepsilon_{5\lambda}^*, \quad (\text{B.5})$$

$$\mathcal{A}_2^{gg} = i \frac{e g_s^2 Q Q}{s_{45} s_{12}} [\bar{u}_3 \gamma_\rho (-\not{p}_4 - \not{p}_5 + m_Q) \gamma^\lambda v_4] V_3^{\mu\nu\sigma}(p_1, -p_1 - p_2, p_2) \varepsilon_{1\mu} \varepsilon_{2\nu} \varepsilon_{5\lambda}^*, \quad (\text{B.6})$$

$$\mathcal{A}_3^{gg} = i \frac{e g_s^2 Q Q}{s_{35} s_{24}} [\bar{u}_3 \not{\epsilon}_5^* (\not{p}_3 + \not{p}_5 + m_Q) \not{\epsilon}_1 (\not{p}_2 - \not{p}_4 + m_Q) \not{\epsilon}_2 v_4], \quad (\text{B.7})$$

$$\mathcal{A}_4^{gg} = -i \frac{e g_s^2 Q Q}{s_{13} s_{24}} [\bar{u}_3 \not{\epsilon}_1 (-\not{p}_1 + \not{p}_3 + m_Q) \not{\epsilon}_5^* (\not{p}_2 - \not{p}_4 + m_Q) \not{\epsilon}_2 v_4], \quad (\text{B.8})$$

$$\mathcal{A}_5^{gg} = i \frac{e g_s^2 Q Q}{s_{45} s_{13}} [\bar{u}_3 \not{\epsilon}_1 (-\not{p}_1 + \not{p}_3 + m_Q) \not{\epsilon}_2 (-\not{p}_4 - \not{p}_5 + m_Q) \not{\epsilon}_5^* v_4], \quad (\text{B.9})$$

$$\mathcal{A}_6^{gg} = \mathcal{A}_3^{gg}(p_1 \leftrightarrow p_2), \quad (\text{B.10})$$

$$\mathcal{A}_7^{gg} = \mathcal{A}_4^{gg}(p_1 \leftrightarrow p_2), \quad (\text{B.11})$$

$$\mathcal{A}_8^{gg} = \mathcal{A}_5^{gg}(p_1 \leftrightarrow p_2), \quad (\text{B.12})$$

where  $V_3^{\mu\nu\rho}$  is the triple gluon vertex given in Eq. A.21, and the amplitudes in Eqs B.5 - B.12 have been labelled after the Feynman diagrams in Fig 2.3. Using the standard *trace technology* and the sums of external polarization vectors for photon and gluons given in Eqs. 2.19 and 2.20, one can easily calculate the tree-level matrix element squared,  $\sum |\mathcal{A}_0|^2$ , taking into account the color factors, according to Eqs. 2.17 and 2.18. The resulting  $\sum |\mathcal{M}|^2$  is expressed in terms of scalar product of 4-vectors,  $p_i \cdot p_j$ , masses of external particles, and some constants.

## B.2 LO amplitudes using spinor-helicity formalism

The spinor-helicity formalism [105, 106] has been widely used in the calculation of scattering amplitudes for massless particles, and considered as one of the most efficient approaches since it provides compact expressions. Several extensions of the spinor-helicity formalism for massive particles has been constructed (see, for example [107, 108]), and a few recent calculations have implemented them [109, 110, 111]. In this Appendix, we will briefly discuss the spinor-helicity formalism both for massless and massive particles, and show explicit expressions for the LO  $q\bar{q} \rightarrow Q\bar{Q}\gamma$  amplitudes. Detailed review on spinor helicity formalism can be found in [112, 113, 11].

In this Appendix we will use the following notation for massless spinors (of momentum  $p_i$ ),

$$\begin{aligned} |i\rangle &= |i+\rangle = u_+(p_i) = v_-(p_i), \\ |i] &= |i-\rangle = u_-(p_i) = v_+(p_i), \\ \langle i| &= \langle i-| = \bar{u}_-(p_i) = \bar{v}_+(p_i), \\ [i| &= \langle i+| = \bar{u}_+(p_i) = \bar{v}_-(p_i), \end{aligned} \quad (\text{B.13})$$

where

$$u_+(p_i) = P_R u(p_i), \quad (\text{B.14})$$

$$u_-(p_i) = P_L u(p_i). \quad (\text{B.15})$$

$u(p_i)$  is the solution of massless Dirac equation,  $\not{p}_i u(p_i) = 0$ .  $P_R$  and  $P_L$  are right- and left-handed projection operators given by

$$P_R = \frac{1 + \gamma_5}{2} \quad \text{and} \quad P_L = \frac{1 - \gamma_5}{2}. \quad (\text{B.16})$$

The only non-zero massless spinor products are then defined as follows,

$$\langle ij \rangle = \bar{u}_-(p_i) u_+(p_j), \quad (\text{B.17})$$

$$[ij] = \bar{u}_+(p_i) u_-(p_j), \quad (\text{B.18})$$

while we use the following notation for spinor strings,

$$\langle i|m \cdots n|j \rangle = \bar{u}_-(p_i) \not{p}_m \cdots \not{p}_n u_-(p_j) \quad (\text{odd } \# \text{ of } p), \quad (\text{B.19})$$

$$\langle i|m \cdots n|j \rangle = \bar{u}_-(p_i) \not{p}_m \cdots \not{p}_n u_+(p_j) \quad (\text{even } \# \text{ of } p), \quad (\text{B.20})$$

$$[i|m \cdots n|j] = \bar{u}_+(p_i) \not{p}_m \cdots \not{p}_n u_-(p_j) \quad (\text{even } \# \text{ of } p). \quad (\text{B.21})$$

Massless spinor products are related to the corresponding 4-vector product by

$$\langle ij \rangle [ji] = 2p_i \cdot p_j, \quad (\text{B.22})$$

and satisfy the following relations, useful in simplifying the expression of the amplitude,

$$\langle ij \rangle = -\langle ji \rangle, \quad [ij] = -[ji], \quad \langle ii \rangle = 0, \quad [ii] = 0, \quad (\text{B.23})$$

$$\not{p}_i = |i\rangle\langle i| + |i][i|, \quad (\text{B.24})$$

$$\langle i|\gamma_\mu|j\rangle\langle k|\gamma^\mu|l\rangle = 2\langle ik\rangle[lj] \quad (\text{Fierz identity}), \quad (\text{B.25})$$

$$\langle ij\rangle\langle kl\rangle + \langle ik\rangle\langle lj\rangle + \langle il\rangle\langle jk\rangle = 0 \quad (\text{Schouten identity}). \quad (\text{B.26})$$

The polarization vectors for massless external vector bosons can be expressed in terms of spinor string as follows,

$$\varepsilon_+^\mu(k, q) = \frac{\langle q|\gamma^\mu|k\rangle}{\sqrt{2}\langle qk\rangle}, \quad (\text{B.27})$$

$$\varepsilon_-^\mu(k, q) = \frac{[q|\gamma^\mu|k\rangle}{\sqrt{2}[qk]}, \quad (\text{B.28})$$

where  $q$  is an arbitrary massless reference vector.

For massive particle, we can decompose a massive momentum into two massless momenta by

$$p_i = p_i^b + \frac{m_i^2}{2p_i^b \cdot \eta} \eta, \quad (\text{B.29})$$

where  $p_i^\flat$  is a massless vector while  $\eta$  is an arbitrary massless reference vector. A massive spinor can then be constructed from the corresponding massless spinor as follows

$$\begin{aligned}
\bar{u}_+(p_i, m_i; p_i^\flat, \eta) &= [i^\flat + \frac{m_i}{\langle \eta i^\flat \rangle} \langle \eta | & , \\
\bar{u}_-(p_i, m_i; p_i^\flat, \eta) &= \langle i^\flat + \frac{m_i}{[\eta i^\flat]} [\eta | & , \\
v_+(p_i, m_i; p_i^\flat, \eta) &= i^\flat] - \frac{m_i}{\langle i^\flat \eta \rangle} \eta \rangle & , \\
v_-(p_i, m_i; p_i^\flat, \eta) &= i^\flat \rangle - \frac{m_i}{[i^\flat \eta]} \eta] & .
\end{aligned} \tag{B.30}$$

In this approach we add spin/helicity label to the spinors and polarization vectors, i.e.

$$u(p_i) \rightarrow u_{s_i}(p_i) \quad \text{and} \quad \varepsilon_\mu^*(p_i) \rightarrow \varepsilon_{\mu, s_i}^*(p_i),$$

and we specify a given spin amplitude as follows

$$\mathcal{A}_0^{q\bar{q}} \rightarrow \mathcal{A}_0^{q\bar{q}}(1_q^{s_1}, 2_{\bar{q}}^{s_2}, 3_Q^{s_3}, 4_{\bar{Q}}^{s_4}, 5_\gamma^{s_5}), \tag{B.31}$$

where  $1_q^{s_1}$  denotes a particle  $q$  with a momentum  $p_1$  and a spin state  $s_1$ , and similarly for the other external particles.

There are 16 spin configurations that need to be calculated in the  $q\bar{q} \rightarrow Q\bar{Q}\gamma$  subprocess. However, half of them, which are the flipped helicity combinations, can be obtained via

$$\mathcal{A}_0^{q\bar{q}}(1_q^{-s_1}, 2_{\bar{q}}^{-s_2}, 3_Q^{-s_3}, 4_{\bar{Q}}^{-s_4}, 5_\gamma^{-s_5}) = \left[ \mathcal{A}_0^{q\bar{q}}(1_q^{s_1}, 2_{\bar{q}}^{s_2}, 3_Q^{s_3}, 4_{\bar{Q}}^{s_4}, 5_\gamma^{s_5}) \right]_{\langle ij \rangle \leftrightarrow [ij]}, \tag{B.32}$$

which is a manifestation of a complex conjugation operation. In addition, using the following relations,

$$\begin{aligned}
\frac{[i^\flat \eta]}{m_i} \bar{u}_-(p_i, m_i; \eta, p_i^\flat) &= \bar{u}_+(p_i, m_i; p_i^\flat, \eta), \\
\frac{\langle i^\flat \eta \rangle}{m_i} v_-(p_i, m_i; \eta, p_i^\flat) &= v_+(p_i, m_i; p_i^\flat, \eta),
\end{aligned} \tag{B.33}$$

one can get the amplitudes with different spin labels for massive spinor by exchanging  $p_i^\flat$  and  $\eta$ . This leaves us with only two independent spin configurations to be computed. In our case, we will take the independent spin configurations to be  $(+ - + + +)$  and  $(+ - + + -)$ .

Taking the individual contributions of the LO  $q\bar{q} \rightarrow Q\bar{Q}\gamma$  amplitude in Eqs. B.1 - B.4, projecting out the external spinors and polarization vectors into individual spin/polarization states and using the notation and relations that have been previously introduced, we can

write the  $(+ - + +)$  amplitude for the LO  $q\bar{q} \rightarrow Q\bar{Q}\gamma$  process as,

$$\begin{aligned}
\mathcal{A}_0^{q\bar{q}}(1_q^+, 2_{\bar{q}}^-, 3_Q^+, 4_{\bar{Q}}^+, 5_\gamma^+) &= i \frac{2\sqrt{2}eg_s^2}{\langle q5 \rangle} m_Q \\
&\times \left\{ \frac{Q_Q}{s_{12}s_{35}} \left[ [3^b 5] \langle q1 \rangle [24^b] + \frac{[3^b 5] \langle 1\eta_4 \rangle}{\langle \eta_4 4^b \rangle} \langle q|3+5|2 \right] \right. \\
&\quad \left. + \frac{\langle \eta_3 q \rangle [24^b]}{\langle \eta_3 3^b \rangle} \langle 1|3|5 \rangle + \frac{m_Q^2 \langle \eta_3 q \rangle [52] \langle 1\eta_4 \rangle}{\langle \eta_3 3^b \rangle \langle \eta_4 4^b \rangle} \right] \\
&+ \frac{Q_Q}{s_{12}s_{45}} \left[ [3^b 2] \langle 1q \rangle [54^b] - \frac{[3^b 2] \langle q\eta_4 \rangle}{\langle \eta_4 4^b \rangle} \langle 1|4|5 \rangle \right. \\
&\quad \left. - \frac{\langle \eta_3 1 \rangle [54^b]}{\langle \eta_3 3^b \rangle} \langle q|4+5|2 \rangle + \frac{m_Q^2 \langle \eta_3 1 \rangle [25] \langle q\eta_4 \rangle}{\langle \eta_3 3^b \rangle \langle \eta_4 4^b \rangle} \right] \\
&- \frac{Q_q \langle q|1|5 \rangle}{(s_{34} + 2m_Q^2)s_{15}} \left[ \frac{\langle \eta_4 1 \rangle [23^b]}{\langle \eta_4 4^b \rangle} + \frac{\langle \eta_3 1 \rangle [24^b]}{\langle \eta_3 3^b \rangle} \right] \\
&- \frac{Q_q \langle 25 \rangle}{(s_{34} + 2m_Q^2)s_{25}} \left[ \frac{\langle \eta_4 1 \rangle}{\langle \eta_4 4^b \rangle} \langle q|-2+5|3^b \rangle + \frac{\langle \eta_3 1 \rangle}{\langle \eta_3 3^b \rangle} \langle q|-2+5|4^b \rangle \right] \Big\}, \quad (\text{B.34})
\end{aligned}$$

and the  $(+ - + + -)$  amplitude as,

$$\begin{aligned}
\mathcal{A}_0^{q\bar{q}}(1_q^+, 2_{\bar{q}}^-, 3_Q^+, 4_{\bar{Q}}^+, 5_\gamma^-) &= i \frac{2\sqrt{2}eg_s^2}{[q5]} m_Q \\
&\times \left\{ \frac{Q_Q}{s_{12}s_{35}} \left[ [3^b q] \langle 51 \rangle [24^b] + \frac{[3^b q] \langle 1\eta_4 \rangle}{\langle \eta_4 4^b \rangle} \langle 5|3|2 \rangle \right. \right. \\
&\quad \left. \left. + \frac{\langle \eta_3 5 \rangle [24^b]}{\langle \eta_3 3^b \rangle} \langle 1|3+5|q \rangle + \frac{m_Q^2 \langle \eta_3 5 \rangle [q2] \langle 1\eta_4 \rangle}{\langle \eta_3 3^b \rangle \langle \eta_4 4^b \rangle} \right] \right. \\
&+ \frac{Q_Q}{s_{12}s_{45}} \left[ \langle 3^b 2 \rangle \langle 15 \rangle [q4^b] - \frac{[3^b 2] \langle 5\eta_4 \rangle}{\langle \eta_4 4^b \rangle} \langle 1|4+5|q \rangle \right. \\
&\quad \left. - \frac{\langle \eta_3 1 \rangle [q4^b]}{\langle \eta_3 3^b \rangle} \langle 5|4|2 \rangle + \frac{m_Q^2 \langle \eta_3 1 \rangle [2q] \langle 5\eta_4 \rangle}{\langle \eta_3 3^b \rangle \langle \eta_4 4^b \rangle} \right] \\
&- \frac{Q_q \langle 51 \rangle}{(s_{34} + 2m_Q^2)s_{15}} \left[ \frac{\langle 23^b \rangle}{\langle \eta_4 4^b \rangle} \langle \eta_4|1-5|q \rangle + \frac{\langle 24^b \rangle}{\langle \eta_3 3^b \rangle} \langle \eta_3|1-5|q \rangle \right] \\
&+ \frac{Q_q \langle 5|2|q \rangle}{(s_{34} + 2m_Q^2)s_{25}} \left[ \frac{\langle \eta_4 1 \rangle [23^b]}{\langle \eta_4 4^b \rangle} + \frac{\langle \eta_3 1 \rangle [24^b]}{\langle \eta_3 3^b \rangle} \right] \Big\}. \quad (\text{B.35})
\end{aligned}$$

The amplitudes in Eqs. B.34 and B.35, which are expressed in terms of spinor products, masses of external particles, and some constants, can be evaluated numerically as complex numbers. The LO matrix element squared is simply a multiplication of two complex numbers, which makes the computation less expensive numerically. The expression for LO  $gg \rightarrow Q\bar{Q}\gamma$  spin amplitudes can also be obtained using the very same technique. A package **SQM** [114], that implements spinor helicity formalism in **Mathematica**, is a useful tool in performing spinor manipulation as well as numerical evaluation of spinor products.

## APPENDIX C

### REDUCTION OF TENSOR INTEGRALS

In evaluating one-loop amplitudes, which are part of any Next-to-Leading Order calculation, we need to compute one-loop integrals, that consist of tensor and scalar integrals as discussed in Sec. 2.3. In this Appendix, we will explicitly demonstrate an example of tensor-integral reduction using the Passarino-Veltman (PV) method [75].

The form of the one-loop integral associated to the diagram shown in Fig. 2.4 is given by Eq. 2.23. As discussed in Sec. 2.3, the one-loop tensor integrals are first decomposed into a linear combination of tensor-integral coefficients multiplied by all possible tensor structures built of products of external momenta and the metric tensor. In our discussion, the arguments of the tensor-integral coefficients will be suppressed for simplicity. By construction, the index of the tensor-integral coefficients are symmetric under all possible permutations. As a convention we always use the one with  $i \leq j \leq k \leq \dots$  for the tensor-integral coefficient in the Lorentz decomposition. For example,  $C_{112}$  is used for one of the rank-3 3-point tensor coefficients instead of  $C_{121}$  or  $C_{211}$ .

The tensor integrals appearing in the NLO calculation of  $pp(p\bar{p}) \rightarrow Q\bar{Q}\gamma$  and their tensor decomposition is given in the following. The decomposition of 2-point tensor integrals up to rank 2 is given by,

$$B_\mu(p_1; m_0, m_1) = p_{1\mu} B_1, \tag{C.1}$$

$$B_{\mu\nu}(p_1; m_0, m_1) = g_{\mu\nu} B_{00} + p_{1\mu} p_{1\nu} B_{11}. \tag{C.2}$$

Similarly, 3-point tensor integrals up to rank 3 can be decomposed as follows

$$C_\mu(p_1, p_2; m_0, m_1, m_2) = \sum_{i=1}^2 p_{i\mu} C_i, \quad (\text{C.3})$$

$$C_{\mu\nu}(p_1, p_2; m_0, m_1, m_2) = g_{\mu\nu} C_{00} + \sum_{i,j=1}^2 p_{i\mu} p_{j\nu} C_{ij}, \quad (\text{C.4})$$

$$\begin{aligned} C_{\mu\nu\rho}(p_1, p_2; m_0, m_1, m_2) &= \sum_{i=1}^2 (g_{\mu\nu} p_{i\rho} + g_{\mu\rho} p_{i\nu} + g_{\nu\rho} p_{i\mu}) C_{00i} \\ &+ \sum_{i,j,k=1}^2 p_{i\mu} p_{j\nu} p_{k\rho} C_{ijk}, \end{aligned} \quad (\text{C.5})$$

and 4-point tensor integrals up to rank 4 as:

$$D_\mu(p_1, p_2, p_3; m_0, m_1, m_2, m_3) = \sum_{i=1}^3 p_{i\mu} D_i, \quad (\text{C.6})$$

$$D_{\mu\nu}(p_1, p_2, p_3; m_0, m_1, m_2, m_3) = g_{\mu\nu} D_{00} + \sum_{i,j=1}^3 p_{i\mu} p_{j\nu} D_{ij}, \quad (\text{C.7})$$

$$\begin{aligned} D_{\mu\nu\rho}(p_1, p_2, p_3; m_0, m_1, m_2, m_3) &= \sum_{i=1}^3 (g_{\mu\nu} p_{i\rho} + g_{\mu\rho} p_{i\nu} + g_{\nu\rho} p_{i\mu}) D_{00i} \\ &+ \sum_{i,j,k=1}^3 p_{i\mu} p_{j\nu} p_{k\rho} D_{ijk}, \end{aligned} \quad (\text{C.8})$$

$$\begin{aligned} D_{\mu\nu\rho\sigma}(p_1, p_2, p_3; m_0, m_1, m_2, m_3) &= (g_{\mu\nu} g_{\rho\sigma} + g_{\mu\rho} g_{\nu\sigma} + g_{\nu\rho} g_{\mu\sigma}) D_{0000} \\ &+ \sum_{i,j=1}^3 (g_{\mu\nu} p_{i\rho} p_{j\sigma} + g_{\mu\rho} p_{i\nu} p_{j\sigma} + g_{\mu\sigma} p_{i\nu} p_{j\rho} \\ &\quad + g_{\nu\rho} p_{i\mu} p_{j\sigma} + g_{\nu\sigma} p_{i\mu} p_{j\rho} + g_{\rho\sigma} p_{i\mu} p_{j\nu}) D_{00ij} \\ &+ \sum_{i,j,k,l=1}^3 p_{i\mu} p_{j\nu} p_{k\rho} p_{l\sigma} D_{ijkl}. \end{aligned} \quad (\text{C.9})$$

Finally, 5-point tensor integrals up to rank 4 can be decomposed as:

$$E_\mu(p_1, p_2, p_3, p_4; m_0, m_1, m_2, m_3, m_4) = \sum_{i=1}^4 p_{i\mu} E_i, \quad (\text{C.10})$$

$$E_{\mu\nu}(p_1, p_2, p_3, p_4; m_0, m_1, m_2, m_3, m_4) = \sum_{i,j=1}^4 p_{i\mu} p_{j\nu} E_{ij}, \quad (\text{C.11})$$

$$E_{\mu\nu\rho}(p_1, p_2, p_3, p_4; m_0, m_1, m_2, m_3, m_4) = \sum_{i,j,k=1}^4 p_{i\mu} p_{j\nu} p_{k\rho} E_{ijk}, \quad (\text{C.12})$$

$$E_{\mu\nu\rho\sigma}(p_1, p_2, p_3, p_4; m_0, m_1, m_2, m_3, m_4) = \sum_{i,j,k,l=1}^4 p_{i\mu} p_{j\nu} p_{k\rho} p_{l\sigma} E_{ijkl}. \quad (\text{C.13})$$

As an example, we discuss in this appendix the reduction of  $C_{\mu\nu}$ , a rank-2 3-point function, using the PV method. Writing explicitly the decomposition of  $C_{\mu\nu}$  in Eq. C.4,

$$C_{\mu\nu} = g_{\mu\nu} C_{00} + p_{1\mu} p_{1\nu} C_{11} + p_{2\mu} p_{2\nu} C_{22} + (p_{1\mu} p_{2\nu} + p_{2\mu} p_{1\nu}) C_{12}, \quad (\text{C.14})$$

and saturating Eq. C.14 with the external momenta  $p_1$  and  $p_2$ , we obtain the following system of equations

$$\begin{aligned} p_1^\nu C_{\mu\nu} &= p_{1\mu} C_{00} + p_{1\mu} p_1^2 C_{11} + p_{2\mu} p_1 \cdot p_2 C_{22} + (p_{1\mu} p_1 \cdot p_2 + p_{2\mu} p_1^2) C_{12}, \\ p_2^\nu C_{\mu\nu} &= p_{2\mu} C_{00} + p_{1\mu} p_1 \cdot p_2 C_{11} + p_{2\mu} p_2^2 C_{22} + (p_{1\mu} p_2^2 + p_{2\mu} p_1 \cdot p_2) C_{12}. \end{aligned} \quad (\text{C.15})$$

On the other hand, according to Eq. 2.23,

$$C_{\mu\nu} = \frac{16\pi^2}{i} \mu^{2\epsilon} \int \frac{d^d k}{(2\pi)^d} \frac{k_\mu k_\nu}{D_0 D_1 D_2}, \quad (\text{C.16})$$

with

$$\begin{aligned} D_0 &= k^2 - m_0^2, \\ D_1 &= (k + p_1)^2 - m_1^2, \\ D_2 &= (k + p_1 + p_2)^2 - m_2^2. \end{aligned} \quad (\text{C.17})$$

Saturating Eq. C.16 with the external momenta  $p_1$  and  $p_2$ , we can obtain a system of equations to be compared with Eq. C.15. Starting from,

$$\begin{aligned} p_1^\nu C_{\mu\nu} &= \frac{16\pi^2}{i} \mu^{2\epsilon} \int \frac{d^d k}{(2\pi)^d} \frac{k_\mu p_1 \cdot k}{D_0 D_1 D_2}, \\ p_2^\nu C_{\mu\nu} &= \frac{16\pi^2}{i} \mu^{2\epsilon} \int \frac{d^d k}{(2\pi)^d} \frac{k_\mu p_2 \cdot k}{D_0 D_1 D_2}, \end{aligned} \quad (\text{C.18})$$

we can then rewrite the dot product between external momenta and the loop momentum,  $p_i \cdot k$ , in terms of the denominator factors  $D_i$  using Eq. C.17, i.e.

$$p_1 \cdot k = \frac{1}{2} [D_1 - D_0 + f_1], \quad \text{with} \quad f_1 = m_1^2 - m_0^2 - p_1^2 \quad (\text{C.19})$$

$$p_2 \cdot k = \frac{1}{2} [D_2 - D_1 + f_2], \quad \text{with} \quad f_2 = m_2^2 - m_1^2 - p_2^2 - p_1 \cdot p_2. \quad (\text{C.20})$$



Substituting  $p_{1,2} \cdot k$  from Eqs. C.19 and C.20 in Eq. C.18, simplifying factors of  $D_i$ , defining the resulting tensor integrals using Eqs. 2.23 and 2.26, and decomposing them into tensor-integral coefficients, we obtain,

$$\begin{aligned}
p_1^\nu C_{\mu\nu} &= \frac{1}{2} \left[ (p_1 + p_2)_\mu B_1(p_1 + p_2; m_0, m_2) - p_{2\mu} B_1(p_2; m_1, m_2) \right. \\
&\quad \left. + p_{1\mu} B_0(p_2; m_1, m_2) + f_1 p_{1\mu} C_1 + f_1 p_{2\mu} C_2 \right], \\
p_2^\nu C_{\mu\nu} &= \frac{1}{2} \left[ p_{1\mu} B_1(p_1; m_0, m_1) - (p_1 + p_2)_\mu B_1(p_1 + p_2; m_0, m_2) \right. \\
&\quad \left. + f_2 p_{1\mu} C_1 + f_2 p_{2\mu} C_2 \right].
\end{aligned} \tag{C.21}$$

Note that when we cancel  $D_0$  in the reduction process, the integration over the loop momentum has to be shifted in order to match the definition of the one-loop integral in Eq. 2.23.

Equating the RHS of Eq. C.15 and C.21 we obtain a matrix equation of the form

$$\begin{pmatrix} p_1^2 & p_1 \cdot p_2 \\ p_1 \cdot p_2 & p_2^2 \end{pmatrix} \cdot \begin{pmatrix} C_{11} & C_{12} \\ C_{12} & C_{22} \end{pmatrix} = \begin{pmatrix} \mathcal{I}_{11} & \mathcal{I}_{12} \\ \mathcal{I}_{21} & \mathcal{I}_{22} \end{pmatrix}, \tag{C.22}$$

where

$$\mathcal{I}_{11} = \frac{1}{2} [B_1(p_1 + p_2; m_0, m_2) + B_0(p_2; m_1, m_2) + f_1 C_1] - C_{00}, \tag{C.23}$$

$$\mathcal{I}_{12} = \frac{1}{2} [B_1(p_1 + p_2; m_0, m_2) - B_1(p_2; m_1, m_2) + f_1 C_2], \tag{C.24}$$

$$\mathcal{I}_{21} = \frac{1}{2} [B_1(p_1; m_0, m_1) - B_1(p_1 + p_2; m_0, m_2) + f_2 C_1], \tag{C.25}$$

$$\mathcal{I}_{22} = \frac{1}{2} [-B_1(p_1 + p_2; m_0, m_2) + f_2 C_2] - C_{00}. \tag{C.26}$$

Solving Eq. C.22 for the  $C_{11}$ ,  $C_{12}$  and  $C_{22}$  coefficients, we find

$$\begin{pmatrix} C_{11} & C_{12} \\ C_{12} & C_{22} \end{pmatrix} = \begin{pmatrix} p_1^2 & p_1 \cdot p_2 \\ p_1 \cdot p_2 & p_2^2 \end{pmatrix}^{-1} \cdot \begin{pmatrix} \mathcal{I}_{11} & \mathcal{I}_{12} \\ \mathcal{I}_{21} & \mathcal{I}_{22} \end{pmatrix}, \tag{C.27}$$

$$= \frac{1}{\Delta_3} \begin{pmatrix} p_2^2 & -p_1 \cdot p_2 \\ -p_1 \cdot p_2 & p_1^2 \end{pmatrix} \cdot \begin{pmatrix} \mathcal{I}_{11} & \mathcal{I}_{12} \\ \mathcal{I}_{21} & \mathcal{I}_{22} \end{pmatrix}, \tag{C.28}$$

where  $\Delta_3$  is nothing else but the Gram determinant that is defined in Eq. 2.27 for 3-point function ( $N = 3$ ). The solutions for  $C_{11}$ ,  $C_{22}$ , and  $C_{12}$  are now expressed in terms of lower point tensor-integral coefficients as well as lower-rank three-point tensor-integral coefficients and  $C_{00}$ . To calculate the  $C_{00}$  coefficient we saturate Eqs. C.14 and C.16 with the metric tensor  $g_{\mu\nu}$  to get,

$$(4 - 2\epsilon)C_{00} + p_1^2 C_{11} + p_2^2 C_{22} + 2p_1 \cdot p_2 C_{12} = B_0(p_2; m_1, m_2) + m_1^2 C_0. \tag{C.29}$$

By substituting  $C_{11}$ ,  $C_{12}$ ,  $C_{22}$  and solving for  $C_{00}$ , we obtain,

$$C_{00} = \frac{1}{4(1-\epsilon)} \left[ 2m_1^2 C_0 - f_1 C_1 - f_2 C_2 + B_0(p_2; m_1, m_2) \right], \quad (\text{C.30})$$

$$= \frac{1}{4} \left[ 2m_1^2 C_0 - f_1 C_1 - f_2 C_2 + B_0(p_2; m_1, m_2) + 1 \right]. \quad (\text{C.31})$$

In Eq. C.28, we see that the one-stage reduction of rank-2 3-point tensor integrals introduces an inverse power of the GD. Using the reduction procedure that is outlined above, one can also derive the reduction of rank-1 3-point tensor integral, where in the reduction of the tensor-integral coefficients  $C_1$  and  $C_2$  to the scalar integrals  $C_0$  and  $B_0$ , another inverse power of the GD is introduced. Thus, the two-stage reduction process, i.e.  $C_{ij} \rightarrow C_i \rightarrow \{C_0, B_0\}$ , will introduce two powers of the inverse GD.

In Eq. C.30, the  $\mathcal{O}(\epsilon)$  terms have to be kept since  $B_0$  is UV-divergent. Expanding in  $\epsilon$ , a rational term is picked up when the  $\mathcal{O}(\epsilon)$  term multiplies the UV-divergent integral. In addition to the rational terms that are introduced in the reduction of the tensor integrals, there are also rational terms originated from the one-loop amplitude, i.e. when  $\mathcal{O}(\epsilon)$  terms in the numerator of the one-loop amplitude multiply the UV-divergent integrals. The rational terms that are picked up when  $\epsilon$  multiplies a UV-divergent coefficient can be obtained from the following table,

$$\epsilon A_0(m_0) = m_0^2, \quad (\text{C.32})$$

$$\epsilon B_0(p_1, m_0, m_1) = 1, \quad (\text{C.33})$$

$$\epsilon B_1(p_1, m_0, m_1) = -\frac{1}{2}, \quad (\text{C.34})$$

$$\epsilon B_{00}(p_1, m_0, m_1) = \frac{1}{12} (p_1^2 - 3m_0^2 - 3m_1^2), \quad (\text{C.35})$$

$$\epsilon B_{11}(p_1, m_0, m_1) = \frac{1}{3}, \quad (\text{C.36})$$

$$\epsilon C_{00}(p_1, p_2, m_0, m_1, m_2) = \frac{1}{4}, \quad (\text{C.37})$$

$$\epsilon C_{001}(p_1, p_2, m_0, m_1, m_2) = -\frac{1}{6}, \quad (\text{C.38})$$

$$\epsilon C_{002}(p_1, p_2, m_0, m_1, m_2) = -\frac{1}{12}, \quad (\text{C.39})$$

$$\epsilon D_{0000}(p_1, p_2, p_3, m_0, m_1, m_2, m_3) = \frac{1}{24}. \quad (\text{C.40})$$

## APPENDIX D

### $\mathcal{O}(\alpha_s)$ REAL CORRECTIONS TO $pp(p\bar{p}) \rightarrow Q\bar{Q}\gamma$ PROCESS: SOFT AND COLLINEAR MATRIX ELEMENTS

The calculation of the  $\mathcal{O}(\alpha_s)$  real corrections to  $Q\bar{Q}\gamma$  production at hadron colliders, described in Sec. 2.4, require real-correction matrix elements in both the soft and the collinear limits, which will be explicitly shown in this Appendix. As an example, the computation of real-correction matrix element for the  $q\bar{q}$  initiated subprocess (as an example), in the soft and collinear limits, are presented in Secs. D.1 and D.2, respectively.

#### D.1 Matrix element in the soft limit

The soft singularities in the  $\mathcal{O}(\alpha_s)$  real corrections to  $pp(p\bar{p}) \rightarrow Q\bar{Q}\gamma$  process arise when the energy of the emitted gluon vanishes, i.e.  $E_g = k^0 \rightarrow 0$ . The divergent Feynman diagrams in the soft gluon limit for the  $q\bar{q} \rightarrow Q\bar{Q}\gamma + g$  subprocess are shown in Fig. D.1, and the corresponding amplitudes are denoted by  $\mathcal{M}_{\text{soft}}^{q\bar{q}}$ . Writing the amplitude for one of the diagram in Fig. D.1 (i.e.  $\mathcal{M}_{1,\text{soft}}^{q\bar{q};a}$ ),

$$\begin{aligned} \mathcal{M}_{1,\text{soft}}^{q\bar{q};a} &= i\mu^\epsilon \frac{eg_s^3 Q_Q}{s_{12}} (t^{a_6} t^c)_{i_3 i_4} t_{i_2 i_1}^c \bar{v}_2 \gamma_\mu u_1 \\ &\quad \times \bar{u}_3 \not{\epsilon}_k^* \frac{\not{p}_3 + \not{p}_k + m_t}{(p_3 + k)^2 - m_t^2} \not{\epsilon}_5^* \frac{\not{p}_3 + \not{p}_5 + \not{p}_k + m_t}{(p_3 + p_5 + k)^2 - m_t^2} \gamma^\mu v_4. \end{aligned} \quad (\text{D.1})$$

Taking the soft gluon limit,  $k \rightarrow 0$ , and using  $\not{\epsilon}_k^* \not{p}_3 = 2p_3 \cdot \epsilon_k^* - \not{p}_3 \not{\epsilon}_k^*$  together with the Dirac equation for the top quark,  $\bar{u}_3(\not{p}_3 + m_t) = 0$ , we obtain,

$$\begin{aligned} \mathcal{M}_{1,\text{soft}}^{q\bar{q};a} &= i\mu^\epsilon \frac{eg_s^3 Q_Q}{s_{12}} (t^{a_6} t^c)_{i_3 i_4} t_{i_2 i_1}^c \frac{p_3 \cdot \epsilon_k^*}{p_3 \cdot k} [\bar{v}_2 \gamma_\mu u_1] [\bar{u}_3 \not{\epsilon}_5^* (\not{p}_3 + \not{p}_5 + m_t) \gamma^\mu v_4], \\ &= (t^{a_6} t^c)_{i_3 i_4} t_{i_2 i_1}^c g_s \mu^\epsilon \left( \frac{p_3 \cdot \epsilon_k^*}{p_3 \cdot k} \right) \mathcal{A}_1^{q\bar{q}}, \end{aligned} \quad (\text{D.2})$$

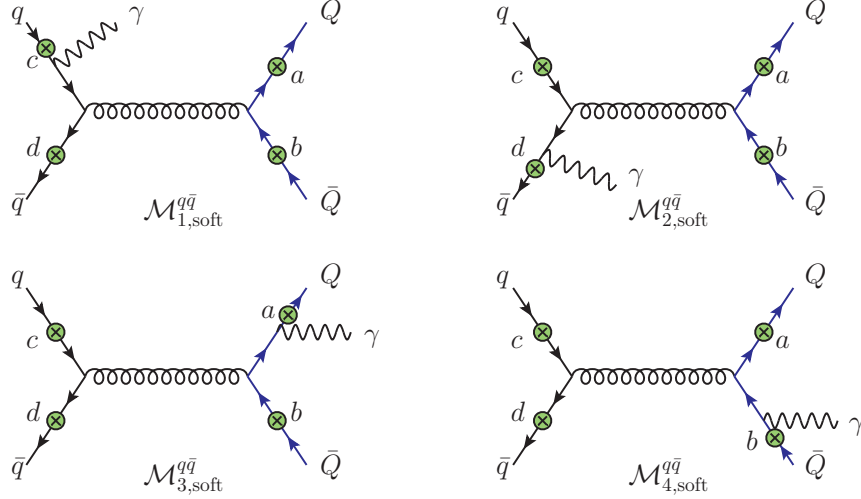


Figure D.1: Divergent Feynman diagrams in the soft limit, for the  $q\bar{q} \rightarrow Q\bar{Q}\gamma$  subprocess. The green-circled crosses correspond to all possible external gluon leg insertions.

with  $\mathcal{A}_1^{q\bar{q}}$  is defined in Eq. 2.12. Similarly for  $\mathcal{A}_{1,\text{soft}}^{q\bar{q};b,c,d}$ ,

$$\mathcal{M}_{1,\text{soft}}^{q\bar{q};b} = (t^c t^{a6})_{i_3 i_4} t_{i_2 i_1}^c g_s \mu^\epsilon \left( -\frac{p_4 \cdot \varepsilon_k^*}{p_4 \cdot k} \right) \mathcal{A}_1^{q\bar{q}}, \quad (\text{D.3})$$

$$\mathcal{M}_{1,\text{soft}}^{q\bar{q};c} = t_{i_3 i_4}^c (t^c t^{a6})_{i_2 i_1} g_s \mu^\epsilon \left( -\frac{p_1 \cdot \varepsilon_k^*}{p_1 \cdot k} \right) \mathcal{A}_1^{q\bar{q}}, \quad (\text{D.4})$$

$$\mathcal{M}_{1,\text{soft}}^{q\bar{q};d} = t_{i_3 i_4}^c (t^{a6} t^c)_{i_2 i_1} g_s \mu^\epsilon \left( \frac{p_2 \cdot \varepsilon_k^*}{p_2 \cdot k} \right) \mathcal{A}_1^{q\bar{q}}. \quad (\text{D.5})$$

Summing all contributions of the divergent diagrams in the  $q\bar{q} \rightarrow Q\bar{Q}\gamma$  subprocess in the soft gluon limit, we get,

$$\begin{aligned} \mathcal{M}_{0,\text{soft}}^{q\bar{q}} &= \sum_{i=1}^4 \left( \mathcal{M}_{i,\text{soft}}^{q\bar{q};a} + \mathcal{M}_{i,\text{soft}}^{q\bar{q};b} + \mathcal{M}_{i,\text{soft}}^{q\bar{q};c} + \mathcal{M}_{i,\text{soft}}^{q\bar{q};d} \right) \\ &= g_s \mu^\epsilon \mathcal{A}_0^{q\bar{q}} \\ &\quad \times \left\{ (t^{a6} t^c)_{i_3 i_4} t_{i_2 i_1}^c \left( \frac{p_3 \cdot \varepsilon_k^*}{p_3 \cdot k} \right) + (t^c t^{a6})_{i_3 i_4} t_{i_2 i_1}^c \left( -\frac{p_4 \cdot \varepsilon_k^*}{p_4 \cdot k} \right) \right. \\ &\quad \left. + t_{i_3 i_4}^c (t^c t^{a6})_{i_2 i_1} \left( -\frac{p_1 \cdot \varepsilon_k^*}{p_1 \cdot k} \right) + t_{i_3 i_4}^c (t^{a6} t^c)_{i_2 i_1} \left( \frac{p_2 \cdot \varepsilon_k^*}{p_2 \cdot k} \right) \right\}. \quad (\text{D.6}) \end{aligned}$$

The above equation is the explicit form of the soft amplitude that is given in Eq. 2.67 for the  $q\bar{q} \rightarrow Q\bar{Q}\gamma + g$  channel, where the terms inside the curly bracket are the eikonal factor.

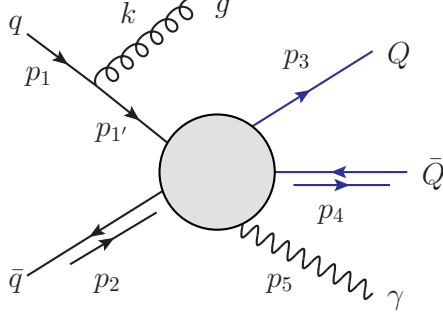


Figure D.2: Schematic diagram involving a final state gluon radiated from initial quark line in the  $q\bar{q} \rightarrow Q\bar{Q}\gamma + g$  subprocess.

Squaring the soft amplitudes and summing over the spins and colors,

$$\begin{aligned}
\sum |\mathcal{M}_{0,\text{soft}}^{q\bar{q}}|^2 &= g_s^2 \mu^{2\epsilon} \frac{N^2 - 1}{4} \sum |\mathcal{A}_0^{q\bar{q}}|^2 \\
&\times \left\{ \frac{N}{2} \left[ -\frac{m_Q^2}{(p_3 \cdot k)^2} - \frac{m_Q^2}{(p_4 \cdot k)^2} + \frac{p_1 \cdot p_3}{p_1 \cdot k p_3 \cdot k} + \frac{p_2 \cdot p_4}{p_2 \cdot k p_4 \cdot k} \right] \right. \\
&\quad + \frac{1}{2N} \left[ \frac{m_Q^2}{(p_3 \cdot k)^2} + \frac{m_Q^2}{(p_4 \cdot k)^2} - \frac{p_1 \cdot p_2}{p_1 \cdot k p_2 \cdot k} - \frac{p_3 \cdot p_4}{p_3 \cdot k p_4 \cdot k} \right. \\
&\quad \left. \left. + \frac{2p_1 \cdot p_4}{p_1 \cdot k p_4 \cdot k} + \frac{2p_2 \cdot p_3}{p_2 \cdot k p_3 \cdot k} - \frac{2p_1 \cdot p_3}{p_1 \cdot k p_3 \cdot k} - \frac{2p_2 \cdot p_4}{p_2 \cdot k p_4 \cdot k} \right] \right\}, \tag{D.7}
\end{aligned}$$

where we have used

$$\sum \varepsilon_k^{\mu*} \varepsilon_k^\nu = -g^{\mu\nu} + \frac{k^\mu q^\nu + k^\nu q^\mu}{k \cdot q}, \tag{D.8}$$

for the external gluon polarization sum, with only the  $g^{\mu\nu}$  term gives nonzero result in the case of gluon emitted from the quark line.  $\mathcal{A}_0^{q\bar{q}}$  is the color-stripped LO  $q\bar{q} \rightarrow Q\bar{Q}\gamma$  amplitude, given in Eq. 2.13. Again, Eq. D.7 is the explicit form of the soft amplitude squared given in Eq. 2.68.

## D.2 Matrix element in the collinear limit

The  $\mathcal{O}(\alpha_s)$  real corrections to  $pp(p\bar{p}) \rightarrow Q\bar{Q}\gamma$  process suffer from collinear singularities when two massless partons become collinear, i.e.  $\cos \theta_{ij} \rightarrow 1$ , and the propagator denominator in the amplitude vanishes,  $2k_i \cdot k_j = E_i E_j (1 - \cos \theta_{ij}) \rightarrow 0$ . In this Section, we will show the calculation of a collinear amplitude, taking the  $q\bar{q} \rightarrow Q\bar{Q}\gamma + g$  channel, with the external gluon is emitted from the initial quark line as an example, as shown in Fig. D.2.

To parameterize the external momenta in the collinear limit, it is convenient to use Sudakov decomposition, given as follows:

$$\begin{aligned} p_1^\mu &= p_{1'}^\mu + k^\mu, \\ p_{1'}^\mu &= zp_1^\mu + \xi n^\mu + p_T^\mu, \\ k^\mu &= (1-z)p_1^\mu - \xi n^\mu - p_T^\mu, \end{aligned} \quad (\text{D.9})$$

where,

$$\xi = -\frac{p_T^2}{2(1-z)}, \quad p_1 \cdot n = 1.$$

Writing explicitly the momentum component of the incoming quark, normal and transverse 4-vectors,

$$\begin{aligned} p_1^\mu &= (P, 0, 0, P), \\ n^\mu &= \left( \frac{1}{P}, 0, 0, 0 \right), \\ p_T^\mu &= (0, p_\perp, 0, 0), \end{aligned} \quad (\text{D.10})$$

the momentum component of the emitted gluon and quark are given by,

$$p_{1'}^\mu = \left( zP - \frac{p_\perp^2}{2(1-z)P}, p_\perp, 0, zP \right), \quad (\text{D.11})$$

$$k^\mu = \left( (1-z)P + \frac{p_\perp^2}{2(1-z)P}, -p_\perp, 0, (1-z)P \right), \quad (\text{D.12})$$

where

$$p_{1'}^2 = -\frac{p_\perp^2}{1-z}. \quad (\text{D.13})$$

The scattering amplitude for the process shown in Fig. D.2 is given by,

$$\mathcal{M}(1_q, 2_{\bar{q}}, 3_Q, 4_{\bar{Q}}, 5_\gamma, k_g) = -g_s \mu^\epsilon t_{i_1, i_1}^a \tilde{\mathcal{M}}_{i_2 i_1'}(2_{\bar{q}}, 3_Q, 4_{\bar{Q}}, 5_\gamma) \frac{\not{p}_{1'}}{p_{1'}^2} \gamma_\mu \varepsilon_k^{\mu*} u_1, \quad (\text{D.14})$$

$$\stackrel{\text{coll}}{=} g_s \mu^\epsilon t_{i_1, i_1}^a \frac{1-z}{p_\perp^2} \tilde{\mathcal{M}}_{i_2 i_1'}(2_{\bar{q}}, 3_Q, 4_{\bar{Q}}, 5_\gamma) \not{p}_{1'} \gamma_\mu \varepsilon_k^{\mu*} u_1. \quad (\text{D.15})$$

Where in Eq. D.15, we have substituted  $p_{1'}^2$  from Eq. D.13. Expressing  $p_{1'}$  in terms of  $p_1$  and  $k$ , using Dirac equation for massless quark,  $\not{p}_1 u_1 = 0$  and substituting  $(1-z)p_1$  using the third equation in Eq. D.9, and neglecting  $\mathcal{O}(p_\perp^2)$  terms,

$$\begin{aligned} (1-z)\not{p}_{1'} \gamma_\mu \varepsilon_k^{\mu*} u_1 &\simeq [2p_T^\mu - (1-z)\gamma_\mu \not{p}_T] \varepsilon_k^{\mu*} u_1 \\ &\equiv \mathcal{J}_\mu(z, p_T) \varepsilon_k^{\mu*} u_1, \end{aligned}$$

and the collinear amplitude becomes,

$$\mathcal{M}(1_q, 2_{\bar{q}}, 3_Q, 4_{\bar{Q}}, 5_\gamma, k_g)_{\text{coll}} = \frac{g_s \mu^\epsilon t_{i_1, i_1}^a}{p_\perp^2} \tilde{\mathcal{M}}_{i_2 i_1'}(2_{\bar{q}}, 3_Q, 4_{\bar{Q}}, 5_\gamma) \mathcal{J}_\mu(z, p_T) \varepsilon_k^{\mu*} u_1. \quad (\text{D.16})$$

Squaring the collinear amplitude, and summing over spins and colors (also taking the average over initial quark colors), we obtain,

$$\begin{aligned} \sum |\mathcal{M}(1_q, 2_{\bar{q}}, 3_Q, 4_{\bar{Q}}, 5_\gamma, k_g)|_{\text{coll}}^2 &= \frac{g_s^2 \mu^{2\epsilon} N^2 - 1}{p_\perp^4} \frac{N^2 - 1}{2N} \cdot \sum \varepsilon_k^{\mu*} \varepsilon_k^\nu \\ &\times \text{Tr}[\tilde{\mathcal{M}}_{i_2 i_1'}(2_{\bar{q}}, 3_Q, 4_{\bar{Q}}, 5_\gamma) \mathcal{J}_\mu(z, p_T) \not{p}_1 \\ &\quad \mathcal{J}_\nu^\dagger(z, p_T) \tilde{\mathcal{M}}_{i_2 i_1'}^\dagger(2_{\bar{q}}, 3_Q, 4_{\bar{Q}}, 5_\gamma)]. \quad (\text{D.17}) \end{aligned}$$

Using the external gluon polarization vector sum given in Eq. D.8,

$$\mathcal{J}_\mu(z, p_T) \not{p}_1 \mathcal{J}_\nu^\dagger(z, p_T) \sum \varepsilon_k^{\mu*} \varepsilon_k^\nu = 2p_\perp^2 \not{p}_1 (1 + z^2), \quad (\text{D.18})$$

leads us the the expression of real-correction amplitude squared for the  $q\bar{q} \rightarrow Q\bar{Q}\gamma + g$  channel, where the gluon is emitted from initial quark line, in the collinear limit,

$$\begin{aligned} &\sum |\mathcal{M}(1_q, 2_{\bar{q}}, 3_Q, 4_{\bar{Q}}, 5_\gamma, k_g)|_{\text{coll}}^2 \\ &= (4\pi\mu^{2\epsilon}\alpha_s) \frac{2}{z} \frac{1 + z^2}{p_\perp^2} \frac{N^2 - 1}{2N} \times \text{Tr}[\tilde{\mathcal{M}}_{i_2 i_1'}(2_{\bar{q}}, 3_Q, 4_{\bar{Q}}, 5_\gamma) \not{p}_1 \tilde{\mathcal{M}}_{i_2 i_1'}^\dagger(2_{\bar{q}}, 3_Q, 4_{\bar{Q}}, 5_\gamma)], \quad (\text{D.19}) \end{aligned}$$

$$\begin{aligned} &= (4\pi\mu^{2\epsilon}\alpha_s) \frac{2}{zs_{ik}} \frac{N^2 - 1}{2N} \left( \frac{1 + z^2}{1 - z} \right) \sum |\mathcal{M}(1'_q, 2_{\bar{q}}, 3_Q, 4_{\bar{Q}}, 5_\gamma)|^2, \\ &= (4\pi\mu^{2\epsilon}\alpha_s) \frac{2}{zs_{ik}} P_{qq}(z) \sum |\mathcal{M}(1'_q, 2_{\bar{q}}, 3_Q, 4_{\bar{Q}}, 5_\gamma)|^2. \quad (\text{D.20}) \end{aligned}$$

The above equation is the explicit form of the collinear-amplitude squared that is given in Eq. 2.72.

The Altarelli-Parisi splitting functions that appear in the calculation of the collinear amplitude are given by [66],

$$P_{qq}(z) = \frac{N^2 - 1}{2N} \left[ \frac{1 + z^2}{1 - z} - \epsilon(1 - z) \right], \quad (\text{D.21})$$

$$P_{gg}(z) = 2N \left[ \frac{z}{1 - z} + \frac{1 - z}{z} + z(1 - z) \right], \quad (\text{D.22})$$

$$P_{gq}(z) = \frac{z^2 + (1 - z)^2}{2} - \epsilon z(1 - z), \quad (\text{D.23})$$

$$P_{qg}(z) = \frac{N^2 - 1}{2N} \left[ \frac{1 + (1 - z)^2}{z} - \epsilon z \right]. \quad (\text{D.24})$$

We also use the following notation,  $P_{ij}(z, \epsilon) = P_{ij}(z) + \epsilon P'_{ij}(z)$ , in order to specify the  $\mathcal{O}(1)$  and  $\mathcal{O}(\epsilon)$  parts of the splitting function.

# REFERENCES

- [1] Georges Aad et al. Observation of a new particle in the search for the Standard Model Higgs boson with the ATLAS detector at the LHC. *Phys.Lett.*, B716:1–29, 2012, 1207.7214.
- [2] Serguei Chatrchyan et al. Observation of a new boson at a mass of 125 GeV with the CMS experiment at the LHC. *Phys.Lett.*, B716:30–61, 2012, 1207.7235.
- [3] Charalampos Anastasiou, Lance J. Dixon, Kirill Melnikov, and Frank Petriello. High precision QCD at hadron colliders: Electroweak gauge boson rapidity distributions at NNLO. *Phys.Rev.*, D69:094008, 2004, hep-ph/0312266.
- [4] Peter Baernreuther, Michal Czakon, and Alexander Mitov. Percent Level Precision Physics at the Tevatron: First Genuine NNLO QCD Corrections to  $q\bar{q} \rightarrow t\bar{t} + X$ . *Phys.Rev.Lett.*, 109:132001, 2012, 1204.5201.
- [5] Johan Alwall, Michel Herquet, Fabio Maltoni, Olivier Mattelaer, and Tim Stelzer. MadGraph 5 : Going Beyond. *JHEP*, 1106:128, 2011, 1106.0522.
- [6] A. Pukhov, E. Boos, M. Dubinin, V. Edneral, V. Ilyin, et al. CompHEP: A Package for evaluation of Feynman diagrams and integration over multiparticle phase space. 1999, hep-ph/9908288.
- [7] A. Pukhov. CalcHEP 2.3: MSSM, structure functions, event generation, batches, and generation of matrix elements for other packages. 2004, hep-ph/0412191.
- [8] John M. Campbell and R.K. Ellis. MCFM for the Tevatron and the LHC. *Nucl.Phys.Proc.Suppl.*, 205-206:10–15, 2010, 1007.3492.
- [9] K. Arnold, M. Bahr, Giuseppe Bozzi, F. Campanario, C. Englert, et al. VBFNLO: A Parton level Monte Carlo for processes with electroweak bosons. *Comput.Phys.Commun.*, 180:1661–1670, 2009, 0811.4559.
- [10] T. Binoth, J.P. Guillet, E. Pilon, and M. Werlen. A Full next-to-leading order study of direct photon pair production in hadronic collisions. *Eur.Phys.J.*, C16:311–330, 2000, hep-ph/9911340.
- [11] R. Keith Ellis, Zoltan Kunszt, Kirill Melnikov, and Giulia Zanderighi. One-loop calculations in quantum field theory: from Feynman diagrams to unitarity cuts. *Phys.Rept.*, 518:141–250, 2012, 1105.4319.



- [12] C.F. Berger, Z. Bern, L.J. Dixon, F. Febres Cordero, D. Forde, et al. An Automated Implementation of On-Shell Methods for One-Loop Amplitudes. *Phys.Rev.*, D78:036003, 2008, 0803.4180.
- [13] Thomas Hahn. Automatic loop calculations with FeynArts, FormCalc, and LoopTools. *Nucl.Phys.Proc.Suppl.*, 89:231–236, 2000, hep-ph/0005029.
- [14] Gavin Cullen, Nicolas Greiner, Gudrun Heinrich, Gionata Luisoni, Pierpaolo Mastrolia, et al. Automated One-Loop Calculations with GoSam. *Eur.Phys.J.*, C72:1889, 2012, 1111.2034.
- [15] Valentin Hirschi, Rikkert Frederix, Stefano Frixione, Maria Vittoria Garzelli, Fabio Maltoni, et al. Automation of one-loop QCD corrections. *JHEP*, 1105:044, 2011, 1103.0621.
- [16] Laura Reina and Thomas Schutzmeier. Towards  $W b \bar{b} + j$  at NLO with an Automated Approach to One-Loop Computations. *JHEP*, 1209:119, 2012, 1110.4438.
- [17] Fabio Cascioli, Philipp Maierhofer, and Stefano Pozzorini. Scattering Amplitudes with Open Loops. *Phys.Rev.Lett.*, 108:111601, 2012, 1111.5206.
- [18] R. Frederix, T. Gehrmann, and N. Greiner. Integrated dipoles with MadDipole in the MadGraph framework. *JHEP*, 1006:086, 2010, 1004.2905.
- [19] Tanju Gleisberg, Stefan Hoeche, Frank Krauss, Andreas Schaliche, Steffen Schumann, et al. SHERPA 1. alpha: A Proof of concept version. *JHEP*, 0402:056, 2004, hep-ph/0311263.
- [20] T. Gleisberg, Stefan. Hoeche, F. Krauss, M. Schonherr, S. Schumann, et al. Event generation with SHERPA 1.1. *JHEP*, 0902:007, 2009, 0811.4622.
- [21] S. Catani and M.H. Seymour. A General algorithm for calculating jet cross-sections in NLO QCD. *Nucl.Phys.*, B485:291–419, 1997, hep-ph/9605323.
- [22] Stefano Catani, Stefan Dittmaier, Michael H. Seymour, and Zoltan Trocsanyi. The Dipole formalism for next-to-leading order QCD calculations with massive partons. *Nucl.Phys.*, B627:189–265, 2002, hep-ph/0201036.
- [23] S. Frixione, Z. Kunszt, and A. Signer. Three jet cross-sections to next-to-leading order. *Nucl.Phys.*, B467:399–442, 1996, hep-ph/9512328.
- [24] Torbjorn Sjostrand, Stephen Mrenna, and Peter Z. Skands. PYTHIA 6.4 Physics and Manual. *JHEP*, 0605:026, 2006, hep-ph/0603175.
- [25] Torbjorn Sjostrand, Stephen Mrenna, and Peter Z. Skands. A Brief Introduction to PYTHIA 8.1. *Comput.Phys.Commun.*, 178:852–867, 2008, 0710.3820.
- [26] G. Corcella, I.G. Knowles, G. Marchesini, S. Moretti, K. Odagiri, et al. HERWIG 6: An Event generator for hadron emission reactions with interfering gluons (including supersymmetric processes). *JHEP*, 0101:010, 2001, hep-ph/0011363.

- [27] M. Bahr, S. Gieseke, M.A. Gigg, D. Grellscheid, K. Hamilton, et al. Herwig++ Physics and Manual. *Eur.Phys.J.*, C58:639–707, 2008, 0803.0883.
- [28] Stefano Frixione and Bryan R. Webber. Matching NLO QCD computations and parton shower simulations. *JHEP*, 0206:029, 2002, hep-ph/0204244.
- [29] Paolo Nason. A New method for combining NLO QCD with shower Monte Carlo algorithms. *JHEP*, 0411:040, 2004, hep-ph/0409146.
- [30] Stefano Frixione, Paolo Nason, and Carlo Oleari. Matching NLO QCD computations with Parton Shower simulations: the POWHEG method. *JHEP*, 0711:070, 2007, 0709.2092.
- [31] Michal Czakon, Paul Fiedler, and Alexander Mitov. The total top quark pair production cross-section at hadron colliders through  $O(\alpha_s^4)$ . *Phys.Rev.Lett.*, 110:252004, 2013, 1303.6254.
- [32] Radja Boughezal, Fabrizio Caola, Kirill Melnikov, Frank Petriello, and Markus Schulze. Higgs boson production in association with a jet at next-to-next-to-leading order in perturbative QCD. *JHEP*, 1306:072, 2013, 1302.6216.
- [33] F. Abe et al. Observation of top quark production in  $\bar{p}p$  collisions. *Phys.Rev.Lett.*, 74:2626–2631, 1995, hep-ex/9503002.
- [34] S. Abachi et al. Observation of the top quark. *Phys.Rev.Lett.*, 74:2632–2637, 1995, hep-ex/9503003.
- [35] The Tevatron Electroweak Working Group. Combination of the  $t\bar{t}$  production cross section measurements from the tevatron collider. September 2012. D0 Note 6363.
- [36] Masato Aoki. Top quark production at the lhc. 2013. Moriond QCD and High Energy Interactions, <http://moriond.in2p3.fr/QCD/2013/WednesdayMorning/Aoki.pdf>.
- [37] The Tevatron Electroweak Working Group. Combination of cdf and d0 results on the mass of the top quark using up to 8.7 fb<sup>1</sup> of  $p\bar{p}$  collisions. March 2013. CDF Note 10976, D0 Note 6381.
- [38] The ATLAS and CMS collaboration. Combination of atlas and cms results on the mass of the top quark using up to 4.9/fb of data. June 2013. CMS-PAS-TOP-12-001, ATLAS-CONF-2012-095.
- [39] U. Baur, A. Juste, L.H. Orr, and D. Rainwater. Probing electroweak top quark couplings at hadron colliders. *Phys.Rev.*, D71:054013, 2005, hep-ph/0412021.
- [40] U. Baur, A. Juste, D. Rainwater, and L.H. Orr. Improved measurement of  $t\bar{t}Z$  couplings at the CERN LHC. *Phys.Rev.*, D73:034016, 2006, hep-ph/0512262.
- [41] U. Baur, A. Juste, L.H. Orr, and D. Rainwater. Probing electroweak top quark couplings at hadron and lepton colliders. *Nucl.Phys.Proc.Suppl.*, 160:17–21, 2006, hep-ph/0606264.

- [42] Search for  $t\bar{t}Z$  production in the three lepton final state with  $4.7 \text{ fb}^{-1}$  of  $\sqrt{s} = 7 \text{ TeV}$   $pp$  collision data collected by the ATLAS detector. 2012.
- [43] Measurement of the inclusive  $t \bar{t}$  gamma cross section with the ATLAS detector. 2011.
- [44] Measurement of the associated production of vector bosons with top-antitop pairs at 7 tev. Technical Report CMS-PAS-TOP-12-014, CERN, Geneva, 2012.
- [45] Peng-Fei Duan, Wen-Gan Ma, Ren-You Zhang, Liang Han, Lei Guo, et al. QCD corrections to associated production of  $t\bar{t}\gamma$  at hadron colliders. *Phys.Rev.*, D80:014022, 2009.
- [46] Kirill Melnikov, Markus Schulze, and Andreas Scharf. QCD corrections to top quark pair production in association with a photon at hadron colliders. *Phys.Rev.*, D83:074013, 2011, 1102.1967.
- [47] Achilleas Lazopoulos, Kirill Melnikov, and Frank John Petriello. NLO QCD corrections to the production of  $t\bar{t}Z$  in gluon fusion. *Phys.Rev.*, D77:034021, 2008, 0709.4044.
- [48] Achilleas Lazopoulos, Thomas McElmurry, Kirill Melnikov, and Frank Petriello. Next-to-leading order QCD corrections to  $t\bar{t}Z$  production at the LHC. *Phys.Lett.*, B666:62–65, 2008, 0804.2220.
- [49] Adam Kardos, Zoltan Trocsanyi, and Costas Papadopoulos. Top quark pair production in association with a Z-boson at NLO accuracy. *Phys.Rev.*, D85:054015, 2012, 1111.0610.
- [50] M.V. Garzelli, A. Kardos, C.G. Papadopoulos, and Z. Trocsanyi. Z0 - boson production in association with a top anti-top pair at NLO accuracy with parton shower effects. *Phys.Rev.*, D85:074022, 2012, 1111.1444.
- [51] S. Dittmaier, P. Uwer, and S. Weinzierl. NLO QCD corrections to  $t \text{ anti-}t + \text{jet}$  production at hadron colliders. *Phys.Rev.Lett.*, 98:262002, 2007, hep-ph/0703120.
- [52] S. Dittmaier, P. Uwer, and S. Weinzierl. Hadronic top-quark pair production in association with a hard jet at next-to-leading order QCD: Phenomenological studies for the Tevatron and the LHC. *Eur.Phys.J.*, C59:625–646, 2009, 0810.0452.
- [53] Kirill Melnikov and Markus Schulze. NLO QCD corrections to top quark pair production in association with one hard jet at hadron colliders. *Nucl.Phys.*, B840:129–159, 2010, 1004.3284.
- [54] Kirill Melnikov, Andreas Scharf, and Markus Schulze. Top quark pair production in association with a jet: QCD corrections and jet radiation in top quark decays. *Phys.Rev.*, D85:054002, 2012, 1111.4991.
- [55] V.M. Abazov et al. Measurement of the photon+ $b$ -jet production differential cross section in  $p\bar{p}$  collisions at  $\sqrt{s}=1.96 \text{ TeV}$ . *Phys.Lett.*, B714:32–39, 2012, 1203.5865.

- [56] T. Aaltonen et al. Measurement of the cross section for direct-photon production in association with a heavy quark in  $p\bar{p}$  collisions at  $\sqrt{s} = 1.96$  TeV. 2013, 1303.6136.
- [57] T.P. Stavreva and J.F. Owens. Direct Photon Production in Association With A Heavy Quark At Hadron Colliders. *Phys.Rev.*, D79:054017, 2009, 0901.3791.
- [58] V.M. Abazov et al. Measurement of  $\gamma + b + X$  and  $\gamma + c + X$  production cross sections in p anti-p collisions at  $\sqrt{s} = 1.96$ -TeV. *Phys.Rev.Lett.*, 102:192002, 2009, 0901.0739.
- [59] T. Aaltonen et al. A Study of the associated production of photons and b-quark jets in p p-bar collisions at  $\sqrt{s} = 1.96$ -TeV. *Phys.Rev.*, D81:052006, 2010, 0912.3453.
- [60] A.V. Lipatov, M.A. Malyshev, and N.P. Zotov. Prompt photon and associated heavy quark production at hadron colliders with kt-factorization. *JHEP*, 1205:104, 2012, 1204.3828.
- [61] H. B. Hartanto, L. Reina, and T. Schutzmeier. Heavy-quark associated production with one hard photon at hadron colliders. in preparation.
- [62] D. Binosi and L. Theussl. JaxoDraw: A Graphical user interface for drawing Feynman diagrams. *Comput.Phys.Commun.*, 161:76–86, 2004, hep-ph/0309015.
- [63] John C. Collins, Davison E. Soper, and George F. Sterman. Factorization of Hard Processes in QCD. *Adv.Ser.Direct.High Energy Phys.*, 5:1–91, 1988, hep-ph/0409313.
- [64] Yuri L. Dokshitzer. Calculation of the Structure Functions for Deep Inelastic Scattering and  $e^+ e^-$  Annihilation by Perturbation Theory in Quantum Chromodynamics. *Sov.Phys.JETP*, 46:641–653, 1977.
- [65] V.N. Gribov and L.N. Lipatov. Deep inelastic e p scattering in perturbation theory. *Sov.J.Nucl.Phys.*, 15:438–450, 1972.
- [66] Guido Altarelli and G. Parisi. Asymptotic Freedom in Parton Language. *Nucl.Phys.*, B126:298, 1977.
- [67] S. Alekhin, J. Blumlein, and S. Moch. Parton Distribution Functions and Benchmark Cross Sections at NNLO. *Phys.Rev.*, D86:054009, 2012, 1202.2281.
- [68] Hung-Liang Lai, Marco Guzzi, Joey Huston, Zhao Li, Pavel M. Nadolsky, et al. New parton distributions for collider physics. *Phys.Rev.*, D82:074024, 2010, 1007.2241.
- [69] A.M. Cooper-Sarkar. PDF Fits at HERA. *PoS*, EPS-HEP2011:320, 2011, 1112.2107.
- [70] A.D. Martin, W.J. Stirling, R.S. Thorne, and G. Watt. Parton distributions for the LHC. *Eur.Phys.J.*, C63:189–285, 2009, 0901.0002.
- [71] Richard D. Ball, Valerio Bertone, Stefano Carrazza, Christopher S. Deans, Luigi Del Debbio, et al. Parton distributions with LHC data. *Nucl.Phys.*, B867:244–289, 2013, 1207.1303.

- [72] M.R. Whalley, D. Bourilkov, and R.C. Group. The Les Houches accord PDFs (LHAPDF) and LHAGLUE. 2005, hep-ph/0508110.
- [73] T. Kinoshita. Mass singularities of Feynman amplitudes. *J.Math.Phys.*, 3:650–677, 1962.
- [74] T.D. Lee and M. Nauenberg. Degenerate Systems and Mass Singularities. *Phys.Rev.*, 133:B1549–B1562, 1964.
- [75] G. Passarino and M.J.G. Veltman. One Loop Corrections for  $e^+e^-$  Annihilation Into  $\mu^+\mu^-$  in the Weinberg Model. *Nucl.Phys.*, B160:151, 1979.
- [76] Ansgar Denner and S. Dittmaier. Reduction schemes for one-loop tensor integrals. *Nucl.Phys.*, B734:62–115, 2006, hep-ph/0509141.
- [77] Th. Diaconidis, J. Fleischer, J. Gluza, K. Kajda, T. Riemann, et al. A Complete reduction of one-loop tensor 5 and 6-point integrals. *Phys.Rev.*, D80:036003, 2009, 0812.2134.
- [78] R. Keith Ellis and Giulia Zanderighi. Scalar one-loop integrals for QCD. *JHEP*, 0802:002, 2008, 0712.1851.
- [79] J.A.M. Vermaseren. New features of FORM. 2000, math-ph/0010025.
- [80] G. Peter Lepage. VEGAS: an Adaptive Multidimensional Integration Program. 1980.
- [81] D.B. Melrose. Reduction of Feynman diagrams. *Nuovo Cim.*, 40:181–213, 1965.
- [82] Andrei I. Davydychev. A Simple formula for reducing Feynman diagrams to scalar integrals. *Phys.Lett.*, B263:107–111, 1991.
- [83] O.V. Tarasov. Connection between Feynman integrals having different values of the space-time dimension. *Phys.Rev.*, D54:6479–6490, 1996, hep-th/9606018.
- [84] W.H. Furry. A Symmetry Theorem in the Positron Theory. *Phys.Rev.*, 51:125–129, 1937.
- [85] B.W. Harris and J.F. Owens. The Two cutoff phase space slicing method. *Phys.Rev.*, D65:094032, 2002, hep-ph/0102128.
- [86] John Campbell. TASI 2011: lectures on Perturbative QCD and NLO Monte Carlo Simulations. 2011.
- [87] W. Beenakker, H. Kuijf, W.L. van Neerven, and J. Smith. QCD Corrections to Heavy Quark Production in p anti-p Collisions. *Phys.Rev.*, D40:54–82, 1989.
- [88] L. Reina, S. Dawson, and D. Wackeroth. QCD corrections to associated t anti-t h production at the Tevatron. *Phys.Rev.*, D65:053017, 2002, hep-ph/0109066.
- [89] S. Dawson, C. Jackson, L.H. Orr, L. Reina, and D. Wackeroth. Associated Higgs production with top quarks at the large hadron collider: NLO QCD corrections. *Phys.Rev.*, D68:034022, 2003, hep-ph/0305087.

- [90] L. Bourhis, M. Fontannaz, and J. P. Guillet. Quark and gluon fragmentation functions into photons. *Eur. Phys. J.*, C2:529–537, 1998, hep-ph/9704447.
- [91] A. Gehrmann-De Ridder and E.W. Nigel Glover. Final state photon production at LEP. *Eur.Phys.J.*, C7:29–48, 1999, hep-ph/9806316.
- [92] Stefano Frixione. Isolated photons in perturbative QCD. *Phys.Lett.*, B429:369–374, 1998, hep-ph/9801442.
- [93] W. Beenakker, S. Dittmaier, M. Kramer, B. Plumper, M. Spira, et al. Higgs radiation off top quarks at the Tevatron and the LHC. *Phys.Rev.Lett.*, 87:201805, 2001, hep-ph/0107081.
- [94] W. Beenakker, S. Dittmaier, M. Kramer, B. Plumper, M. Spira, et al. NLO QCD corrections to  $t$  anti- $t$  H production in hadron collisions. *Nucl.Phys.*, B653:151–203, 2003, hep-ph/0211352.
- [95] Rikkert Frederix, Stefano Frixione, Valentin Hirschi, Fabio Maltoni, Roberto Pittau, et al. Scalar and pseudoscalar Higgs production in association with a top-antitop pair. *Phys.Lett.*, B701:427–433, 2011, 1104.5613.
- [96] M.V. Garzelli, A. Kardos, C.G. Papadopoulos, and Z. Trocsanyi. Standard Model Higgs boson production in association with a top anti-top pair at NLO with parton showering. *Europhys.Lett.*, 96:11001, 2011, 1108.0387.
- [97] Benjamin Thayer. On-shell Methods Applied to Exotic Higgs Production at Hadronic Colliders, PhD Thesis, Florida State University, 2012.
- [98] H. B. Hartanto, C. B Jackson, L. Reina, and B. Thayer. Pseudoscalar Higgs production in association with heavy-quark pair at hadron colliders. in preparation.
- [99] J. Pumplin, D.R. Stump, J. Huston, H.L. Lai, Pavel M. Nadolsky, et al. New generation of parton distributions with uncertainties from global QCD analysis. *JHEP*, 0207:012, 2002, hep-ph/0201195.
- [100] Simone Alioli, Paolo Nason, Carlo Oleari, and Emanuele Re. A general framework for implementing NLO calculations in shower Monte Carlo programs: the POWHEG BOX. *JHEP*, 1006:043, 2010, 1002.2581.
- [101] F. Englert and R. Brout. Broken symmetry and the mass of gauge vector mesons. *PRL*, 13(9):321, 1964.
- [102] Peter W. Higgs. Broken symmetries and the masses of gauge bosons. *PRL*, 13(16):508, 1964.
- [103] G. S. Guralnik, C. R. Hagen, and T. W. B. Kibble. Global conservation laws and massless particles. *Phys. Rev. Lett.*, 13:585–587, 1964.
- [104] T. W. B. Kibble. Symmetry breaking in non-abelian gauge theories. *Phys. Rev.*, 155:1554–1561, 1967.

- [105] Frits A. Berends, R. Kleiss, P. De Causmaecker, R. Gastmans, and Tai Tsun Wu. Single Bremsstrahlung Processes in Gauge Theories. *Phys.Lett.*, B103:124, 1981.
- [106] P. De Causmaecker, R. Gastmans, W. Troost, and Tai Tsun Wu. Multiple Bremsstrahlung in Gauge Theories at High-Energies. 1. General Formalism for Quantum Electrodynamics. *Nucl.Phys.*, B206:53, 1982.
- [107] R. Kleiss and W. James Stirling. Spinor Techniques for Calculating  $p$  anti- $p \rightarrow W^{+-} / Z^0 + \text{Jets}$ . *Nucl.Phys.*, B262:235–262, 1985.
- [108] Stefan Dittmaier. Weyl-van der Waerden formalism for helicity amplitudes of massive particles. *Phys.Rev.*, D59:016007, 1998, hep-ph/9805445.
- [109] Simon Badger, John M. Campbell, and R.K. Ellis. QCD corrections to the hadronic production of a heavy quark pair and a W-boson including decay correlations. *JHEP*, 1103:027, 2011, 1011.6647.
- [110] Simon Badger, Ralf Sattler, and Valery Yundin. Analytic Computations of Massive One-Loop Amplitudes. *Nucl.Phys.Proc.Suppl.*, 205-206:61–66, 2010, 1006.5011.
- [111] Simon Badger, Ralf Sattler, and Valery Yundin. One-Loop Helicity Amplitudes for  $t\bar{t}$  Production at Hadron Colliders. *Phys.Rev.*, D83:074020, 2011, 1101.5947.
- [112] Lance J. Dixon. Calculating scattering amplitudes efficiently. 1996, hep-ph/9601359.
- [113] Michael E. Peskin. Simplifying Multi-Jet QCD Computation. 2011, 1101.2414.
- [114] D. Maitre and P. Mastrolia. S@M, a Mathematica Implementation of the Spinor-Helicity Formalism. *Comput.Phys.Commun.*, 179:501–574, 2008, 0710.5559.